



Estudo de Modelos de Turbulência Aplicados à Ventilação de Espaços Interiores

CÉLIA PATRÍCIA DIAS DE ALMEIDA

novembro de 2021

TURBULENCE MODELS STUDY APPLIED TO INDOOR SPACE VENTILATION

Célia Patrícia Dias de Almeida

1140489

2021

Instituto Superior de Engenharia do Porto

Department of Mechanical Engineering



TURBULENCE MODELS STUDY APPLIED TO INDOOR SPACE VENTILATION

Célia Patrícia Dias de Almeida

1140489

Dissertation presented to *Instituto Superior de Engenharia do Porto* as a part of the requirements for fulfilment of the master's degree in Mechanical Engineering, accomplish under the orientation of Professor Rui Filipe Neves de Araújo Rego. Its main goal is the development of a CFD work-flow to study the ventilation of indoor environments, by employing mainly open-source software.

2021

Instituto Superior de Engenharia do Porto

Department of Mechanical Engineering



JURY

President

Raul Duarte Salgueiral Gomes Campilho

Professor Adjunto, Instituto Superior de Engenharia do Porto

Advisor

Rui Filipe Neves Araújo Rego

Professor Adjunto, Instituto Superior de Engenharia do Porto

Co-Advisor

Maria Odete Magalhães Almeida

Sócia em *Paulo Queirós de Faria - Engenheiros Consultores,Lda*, PQF

Examiner

Alexandre Miguel Prior Afonso

Professor Auxiliar, Faculdade de Engenharia da Universidade do Porto

Acknowledgements

In this section, acknowledgement is given to those, without whom, this work wouldn't have been possible.

This work was supervised by Professor Rui de Araújo Rego, to whom I would like to show my gratitude for his continuous support, guidance, qualified help and much needed patience.

I would also like to acknowledge my co-supervisors at the host company, *Paulo Queirós de Faria - Engenheiros Consultores,Lda* (PQF), Engineer Odete de Almeida and Engineer Paulo Queirós de Faria, not only for sharing knowledge about the subject at study, but also in other areas as well (HVAC systems, CAD design, soft skills,etc.), for the constant support and for providing a great work environment. Futhermore, the computations presented would not have been possible, if PQF didn't provide the necessary materials and equipment.

Finally, I would like to give a special thanks to Professor Fernando Aristides Castro, for many productive discussions, support and extensive knowledge on computational fluid dynamics.

PALAVRAS-CHAVE

Modelos de Turbulência; RaNS; Mecânica dos Fluidos Computacional; Métodos Numéricos; Ventilação; OpenFOAM

RESUMO

Mecânica dos Fluidos Computacional tem sido implementada em estudos de ventilação de espaços interiores. Apesar da sua maturidade e utilidade, a sua utilização para aplicações de engenharia como projetos de aquecimento, ventilação e ar condicionado (AVAC) ainda é escassa em Portugal. Com este objetivo, esta dissertação apresenta alguns estudos introdutórios para a criação de um *workflow* de mecânica de fluidos computacional (CFD) para uso por engenheiros de AVAC com pouco conhecimento acerca de práticas de CFD. Assim, alguns aspetos foram investigados, tais como, geração de malhas, esquemas de discretização, *solvers*, condições de fronteira e modelos de turbulência.

A partir de uma panóplia de modelos de turbulência, seis modelos de *Reynolds-averaged Navier-Stokes* (RaNS) de turbulência foram testados e validados para espaços interiores, *standard* $k - \varepsilon$, *renormalization group (RNG)* $k - \varepsilon$, *realizable* $k - \varepsilon$, $\overline{v'^2} - f$, $k - \omega$ e $k - \omega$ *shear stress transport*. O modelo *standard* $k - \varepsilon$ apresenta os resultados mais satisfatórios entre os estudados. O modelo *RNG* $k - \varepsilon$ também demonstrou boa concordância com os resultados experimentais disponíveis na literatura, no entanto necessita de mais tempo de simulação para convergir do que o modelo *standard* $k - \varepsilon$. Com o *realizable* $k - \varepsilon$ não foi possível obter convergência e os modelos $k - \omega$ e $k - \omega$ SST produzem resultados significativamente desfasados da realidade, especialmente na zona afastada das paredes. Estes estudos foram comparados com *benchmarks* do *International Energy Agency Annex 20*.

Esta dissertação também apresenta estudos de convergência de malhas, efeitos de impulsão sobre o escoamento (casos incompressíveis, isotérmicos e não isotérmicos) e simulações de escoamento em regime permanente e transiente.

KEYWORDS

Turbulence Models; RaNS; Computational Fluid Dynamics; Numerical Methods; Ventilation; OpenFOAM

ABSTRACT

Computational Fluid Dynamics has been implemented for indoor environments ventilation studies. Despite of its maturity and usefulness, its use for engineering applications such as heating, ventilation, and air conditioning (HVAC) projects is still scarce in Portugal. With this aim, this dissertation presents some introductory studies to create a computational fluid dynamics (CFD) workflow for the use by HVAC engineers with minimal knowledge of CFD practices. Thus, some aspects were investigated, such as mesh design, discretization schemes, solvers, boundary conditions and turbulence models.

For the latter, from a large set of turbulence models, six Reynolds-averaged Navier-Stokes (RaNS) turbulence models were tested and validated for indoor ventilation, the standard $k - \varepsilon$, the renormalization group (RNG) $k - \varepsilon$, the realizable $k - \varepsilon$, the $\overline{v'^2} - f$, the $k - \omega$ and the $k - \omega$ shear stress transport (SST). The standard $k - \varepsilon$ model continues to present the most satisfactory results of all the studied turbulence models. The RNG $k - \varepsilon$ model also showed good agreement with the experimental data, however it required more time to achieve convergence. It was not possible to achieve convergence with the realizable $k - \varepsilon$ model. The $k - \omega$ and $k - \omega$ SST models yield results significantly different from the experimental measurements, specially in the far wall region. These studies were compared with the benchmarks from the International Energy Agency Annex 20.

This work also presents 2D and 3D cases, mesh convergence studies, effects of flow buoyancy (incompressible, isothermal and non-isothermal cases), and steady-state and transient flow simulations.

NOMENCLATURE

Abbreviations

1D/2D/3D	1,2,3-Dimensional
Ansys Fluent	Fluid Simulation Software
CAD	Computer-aided Design
CFD	Computational Fluid Dynamics
CO_2	Carbon Dioxide
COMSOL	Software for Multiphysics Simulation
COVID-19	Coronavirus Disease 2019
CV	Control Volume
DES	Detached Eddy Simulation
DNS	Direct Numerical Simulation
DNS	Direct Numerical Simulation
e.g.	<i>exempli gratia</i> (for example)
EVMs	Eddy Viscosity Models
FVM	Finite Volume Methods
GB	Gigabyte
HVAC	Heating, Ventilation and Air-Conditioning
IEA	International Energy Agency
LES	Large Eddy Simulation
Log-law	Semi-logarithmic relation
OpenFOAM	Open Field Operation and Manipulation
PIMPLE	PISO and SIMPLE combination
PISO	Pressure-Implicit with Splitting of Operators
QUICK	Quadratic Upwind Interpolation for Convective Kinematics
RaNS	Reynolds-averaged Navier-Stokes
RDT	Rapid Distortion Theory
RMS	Root Mean Square
RNG	Re-normalization Group
SGS	Sub-grid Scale
SIMPLE	Semi-Implicit Method for Pressure Linked Equations
SST	Shear Stress Transport

Roman Characters

A	Diagonal component of the coefficient matrix
$A_0, C_1, C_2, C_3,$ $C_{3,RDT}, C_\mu,$ $C_{\mu k\varepsilon}, C_L, C_\eta,$ $C_{\varepsilon 2}$ and $C_{\varepsilon 1}$	Model coefficients
B	Source vector
C_μ	Model coefficient for the eddy viscosity
c_p	Specific heat capacity at constant pressure
D_k, D_ε	Effective diffusivity for turbulent kinetic energy and its dissipation
E	Total energy
e	Thermal/internal energy
f	Relaxation function
F_1, F_2, F_{23}, F_3	Blending functions
f_2, f_μ	Damping functions
g	Gravity
G_b	Generation of turbulent kinetic energy due to buoyancy
G_k, G	Generation of turbulent kinetic energy due to mean velocity gradients
H	Off-diagonal component of the coefficient matrix
I	Identity matrix
I	Turbulent intensity
k	Turbulent kinetic energy
K	Mechanical/kinetic energy
k_{cond}	Thermal conductivity
kl	Laminar kinetic energy
L_{ref}	Turbulent reference length scale
\mathcal{L}	Turbulent length scale ($\overline{v'^2} - f$ Turbulence model)
M	Coefficient matrix
n	Unit normal vector to the surface
p	Pressure
p_k	Kinematic pressure
q	Square root of turbulent kinetic energy (\sqrt{k})
q	Heat flux
\mathfrak{R}	Renormalization group
Re	Reynolds number
Re_θ	Transition momentum thickness Reynolds number
S_{ij}	Rate of strain tensor
S_ϕ	Source term for a variable ϕ
T	Temperature
\mathfrak{T}	Turbulent time scale ($\overline{v'^2} - f$ Turbulence model)

Roman Characters (continuation)

u	Velocity vector
U	Mean velocity vector
u, v, w	x, y and z -components of the velocity
U, V, W	x, y and z -components of the mean velocity
u^+	Dimensionless velocity
u_τ	Friction velocity
u'	Fluctuating components of the velocity
$\overline{u'^2}$	Normal stress
$\overline{u'_i u'_j}$	Reynolds stresses
$\overline{v'^2}$	Turbulent stress normal to streamlines
w (in <i>Boundary conditions</i>)	Value fraction
x	Position vector
x (in <i>Solution Methods</i>)	Vector of unknowns
x, y, z	Cartesian coordinates
y (in <i>Law of the wall</i>)	Distance to the wall
y^+	Dimensionless wall distance
Y_M	Fluctuating dilation in compressible turbulence

Math Symbols

$\partial()/\partial()$	Partial derivative
$d()/d()$	Total derivative
∇	Gradient operator
$\nabla \cdot$	Divergence operator
∇^2	Laplacian operator
\int_V	Volume integral
\oint_S	Surface integral

Super and Subscripts

—	Average
0 and <i>ref</i>	Initial or reference value
i, j, k	Einstein notation
*	Guessed or previous iteration value of a variable

Greek Letters

α	Phase fraction of the given phase
β	Coefficient of thermal expansion
$\beta, \beta^*, \beta_0, \gamma, \gamma_1, \gamma_2, \eta_0$	Model coefficients
γ	Intermittency
Γ	Diffusion coefficient or diffusivity
Δ	Face to cell distance
δ_{ij}	Kronecker delta function
ε	Turbulent kinetic energy dissipation rate
ζ	Square root of turbulent kinetic energy dissipation rate
η	Ratio of the turbulent to mean strain time scale
μ	Absolute or dynamic viscosity
μ_t	Turbulent viscosity
ν	Kinematic viscosity
κ	Von Karman's constant
ρ	Density
σ_{ij}	Stress tensor
$\sigma_k, \sigma_\varepsilon$	Prandtl numbers for turbulent kinetic energy and its dissipation rate, respectively.
τ_{ij}	Viscous stresses
ϕ	Generic variable
ϕ_c	Cell value
ϕ_f	Face value
ω	Specific dissipation rate
$\overline{\omega_i \omega_i}$	Mean-square vorticity fluctuation

LIST OF FIGURES

FIGURE 2.1	MULTISCALE AND MULTIREOLUTION APPROACHES FOR TURBULENCE [1]	13
FIGURE 3.1	TYPICAL VELOCITY PROFILE FOR A TURBULENT BOUNDARY LAYER.[2]	23
FIGURE 3.2	SOME POSSIBLE LOCATIONS TO STORE INFORMATION AT CELLS [3].	43
FIGURE 3.3	TYPES OF MESHES: (A) STRUCTURED, (B) UNSTRUCTURED, AND (C) HYBRID [4].	44
FIGURE 3.4	STEPS OF CFD SIMULATION AND GROUPS OF ERROR SOURCES [5].	45
FIGURE 4.1	CHANNEL GEOMETRY	49
FIGURE 4.2	EVOLUTION OF THE U/U_0 AT THE POINT OF THE VELOCITY GRADIENT MAXIMUM, FOR VELOCITY PROFILE THROUGHOUT THE CHANNEL FOR DIFFERENT MESHES.	52
FIGURE 4.3	EVALUATION OF THE RATIO (U/U_0 MAX) INDEPENDENCE ON THE MESH AT $L = 10\text{M}$.	53
FIGURE 4.4	EVOLUTION OF THE VARIATION OF THE RATIO (U/U_0 MAX) OF THE VELOCITY PROFILE AT $L = 10\text{ M}$ WITH INCREASING NUMBER OF CELLS.	53
FIGURE 4.5	<i>CHECKMESH</i> EXCERPT.	54
FIGURE 4.6	SOLVER COMPARISON FOR THE EVOLUTION OF U/U_0 MAX OF THE VELOCITY PROFILE.	54
FIGURE 4.7	SOLVER COMPARISON FOR THE EVOLUTION OF U/U_0 MAX OF THE VELOCITY PROFILE IN THE LAST 5M OF THE CHANNEL.	55
FIGURE 4.8	CELLS DISTRIBUTION BY PROCESSORS.	55
FIGURE 4.9	RESIDUALS FOR THE MAIN VARIABLES AT STUDY (U , k AND ε).	56
FIGURE 4.10	VELOCITY U/U_0 .	57
FIGURE 4.11	TURBULENT KINETIC ENERGY k (M^2/S^2).	57
FIGURE 4.12	SECTION OF THE CHANNEL IN THE FULLY DEVELOPED REGION OF THE FLOW AT $L = 7\text{m}$.	57
FIGURE 4.13	YPLUS NEAR THE WALL.	57
FIGURE 4.14	VELOCITY PROFILE ACROSS THE CHANNEL.	58
FIGURE 4.15	SKETCH OF THE TWO-DIMENSIONAL TEST CASE [6].	59
FIGURE 4.16	TEST CASE MEASUREMENT LINES.	62
FIGURE 4.17	EVOLUTION OF U/U_0 MAXIMUM AT THE SUPPLY OPENING (INLET).	62
FIGURE 4.18	VELOCITY PROFILE (U/U_0) AT THE ROOM INLET FOR MESHES 2(COARSE), 6(MEDIUM) AND 12(FINE).	63
FIGURE 4.19	VELOCITY PROFILE (U/U_0) AT $x=H$ AND $x=2H$ FOR MESHES 2(COARSE), 6(MEDIUM) AND 12(FINE).	63
FIGURE 4.21	VELOCITY PROFILE (U/U_0) AT $x=H$ AND $x=2H$, NEAR THE ROOM FLOOR.	64
FIGURE 4.20	VELOCITY PROFILE (U/U_0) AT $x=H$ AND $x=2H$, NEAR THE ROOM CEILING.	64
FIGURE 4.22	ASPECT RATIO AND MAXIMUM SKEWNESS.	65
FIGURE 4.23	CELL DISTRIBUTION BY PROCESSOR FOR THE ANNEX 20 ROOM.	65
FIGURE 4.24	TRANSIENT AND STEADY-STATE SOLVER COMPARISON, FOR THE VELOCITY FIELD MAGNITUDE (\mathbf{U}/\mathbf{U}_0) AND RMS VELOCITY ($\sqrt{u'^2}/U_0$) AT THE INLET.	66
FIGURE 4.25	TRANSIENT AND STEADY-STATE SOLVER COMPARISON, FOR THE VELOCITY FIELD MAGNITUDE (\mathbf{U}/\mathbf{U}_0) AND RMS VELOCITY ($\sqrt{u'^2}/U_0$) AT $x = H$ AND $x = 2H$.	67
FIGURE 4.26	TRANSIENT AND STEADY-STATE SOLVER COMPARISON, FOR THE VELOCITY FIELD MAGNITUDE (\mathbf{U}/\mathbf{U}_0) AND RMS VELOCITY ($\sqrt{u'^2}/U_0$) AT $y = H - h/2$ AND $y = h/2$.	67
FIGURE 4.27	VELOCITY MAGNITUDE (U/U_0) FOR THE TURBULENCE MODELS TESTED.	68

FIGURE 4.28 TURBULENT KINETIC ENERGY (k) FOR THE TURBULENCE MODELS TESTED.	69
FIGURE 4.29 VELOCITY PROFILES (\mathbf{U}/\mathbf{U}_0) AT THE INLET FOR DIFFERENT TURBULENCE MODELS AND EXPERIMENT MEASUREMENTS PERFORMED BY NIELSEN [7].	70
FIGURE 4.30 TURBULENT KINETIC ENERGY IN TERMS OF ROOT-MEAN SQUARE (RMS) VELOCITY PROFILES ($\sqrt{u'^2}/U_0$) AT THE INLET, FOR DIFFERENT TURBULENCE MODELS AND EXPERIMENT MEASUREMENTS PERFORMED BY NIELSEN [7].	70
FIGURE 4.31 VELOCITY PROFILES (\mathbf{U}/\mathbf{U}_0) AT $y = H - h/2$ AND $y = h/2$ FOR DIFFERENT TURBULENCE MODELS AND EXPERIMENT MEASUREMENTS PERFORMED BY NIELSEN [7].	71
FIGURE 4.32 RMS VELOCITY PROFILES ($\sqrt{u'^2}/U_0$) AT $y = H - h/2$ AND $y = h/2$ FOR DIFFERENT TURBULENCE MODELS AND EXPERIMENT MEASUREMENTS PERFORMED BY NIELSEN [7].	71
FIGURE 4.33 VELOCITY PROFILES (\mathbf{U}/\mathbf{U}_0) AT $x = H$ AND $x = 2H$ FOR DIFFERENT TURBULENCE MODELS AND EXPERIMENT MEASUREMENTS PERFORMED BY NIELSEN [7].	72
FIGURE 4.34 RMS VELOCITY PROFILES ($\sqrt{u'^2}/U_0$) AT $x = H$ AND $x = 2H$ FOR DIFFERENT TURBULENCE MODELS AND EXPERIMENT MEASUREMENTS PERFORMED BY NIELSEN [7].	72
FIGURE 4.35 RESIDUALS FOR THE MAIN VARIABLES AT STUDY (U , k AND ε) FOR TRANSIENT SOLVER.	73
FIGURE 4.36 RESIDUALS FOR THE MAIN VARIABLES AT STUDY (U , k AND ε) FOR STEADY-STATE SOLVER.	74
FIGURE 4.37 VELOCITY FIELD (\mathbf{U}/\mathbf{U}_0).	74
FIGURE 4.38 VELOCITY VECTOR FIELD.	75
FIGURE 4.39 TURBULENT KINETIC ENERGY ($k \text{ M}^2/\text{S}^2$).	75
FIGURE 4.40 COMPARISON BETWEEN COMPUTED RESULTS FOR MEAN VELOCITY (U/U_0) AND RMS VELOCITY ($\sqrt{u'^2}/U_0$) WITH EXPERIMENT MEASUREMENTS PERFORMED BY NIELSEN [7] AT THE SUPPLY OPENING.	75
FIGURE 4.41 COMPARISON BETWEEN COMPUTED RESULTS FOR MEAN VELOCITY (U/U_0) AND RMS VELOCITY ($\sqrt{u'^2}/U_0$) WITH EXPERIMENT MEASUREMENTS PERFORMED BY NIELSEN [7] AT $x = H$ AND $x = 2H$	76
FIGURE 4.42 COMPARISON BETWEEN COMPUTED RESULTS FOR MEAN VELOCITY (U/U_0) AND RMS VELOCITY ($\sqrt{u'^2}/U_0$) WITH EXPERIMENT MEASUREMENTS PERFORMED BY NIELSEN [7] AT $y = h/2$ AND $y = H - h/2$	76
FIGURE 4.43 SKETCH OF THE TWO-DIMENSIONAL NON-ISOTHERMAL TEST CASE.	78
FIGURE 4.44 ISOTHERMAL AND NON-ISOTHERMAL SOLVER COMPARISON, FOR THE VELOCITY FIELD MAGNITUDE (\mathbf{U}/\mathbf{U}_0) AND RMS VELOCITY ($\sqrt{u'^2}/U_0$) AT THE INLET.	80
FIGURE 4.45 ISOTHERMAL AND NON-ISOTHERMAL SOLVER COMPARISON, FOR THE VELOCITY FIELD MAGNITUDE (\mathbf{U}/\mathbf{U}_0) AND RMS VELOCITY ($\sqrt{u'^2}/U_0$) AT $x = H$ AND $x = 2H$	81
FIGURE 4.46 ISOTHERMAL AND NON-ISOTHERMAL SOLVER COMPARISON, FOR THE VELOCITY FIELD MAGNITUDE (\mathbf{U}/\mathbf{U}_0) AND RMS VELOCITY ($\sqrt{u'^2}/U_0$) AT $y = h/2$ AND $y = H - h/2$	81
FIGURE 4.47 COMPARISON OF NIELSEN PREDICTIONS FOR $Ar = 0.02$ AT $Re = 5000$ AND THE COMPUTATIONAL RESULTS AT $Re = 5000$	83
FIGURE 4.48 TEMPERATURE STRATIFICATION AND VELOCITY VECTOR FIELD AT $Re = 5000$, FOR DIFFERENT ARCHIMEDES NUMBERS.	84
FIGURE 4.49 TEMPERATURE STRATIFICATION AND VELOCITY VECTOR FIELD AT $Re = 7100$, FOR DIFFERENT ARCHIMEDES NUMBERS.	85
FIGURE 4.50 SKETCH OF THE THREE-DIMENSIONAL ISOTHERMAL TEST CASE.	87
FIGURE 4.51 VELOCITY PROFILE (U/U_0) AT THE ROOM INLET AT THE SYMMETRY PLANE.	89
FIGURE 4.52 VELOCITY PROFILE (U/U_0) AT $x = H$ AND $x = 2H$ AT THE SYMMETRY PLANE.	89

FIGURE 4.53 VELOCITY PROFILE (U/U_0) AT $y = h/2$ AND $y = H - h/2$ AT THE SYMMETRY PLANE.	90
FIGURE 4.54 CELL DISTRIBUTION BY PROCESSOR FOR THE IEA ANNEX 20 3D ROOM.	90
FIGURE 4.55 COMPARISON BETWEEN COMPUTED RESULTS FOR MEAN VELOCITY (U/U_0) AND RMS VELOCITY ($\sqrt{u'^2}/U_0$) WITH EXPERIMENT MEASUREMENTS PERFORMED BY NIELSEN [7] AT THE SUPPLY OPENING (SYMMETRY PLANE).	91
FIGURE 4.56 COMPARISON BETWEEN COMPUTED RESULTS FOR MEAN VELOCITY (U/U_0) AND RMS VELOCITY ($\sqrt{u'^2}/U_0$) WITH EXPERIMENT MEASUREMENTS PERFORMED BY NIELSEN [7] AT $x = H$ AND $x = 2H$ (SYMMETRY PLANE).	92
FIGURE 4.57 COMPARISON BETWEEN COMPUTED RESULTS FOR MEAN VELOCITY (U/U_0) AND RMS VELOCITY ($\sqrt{u'^2}/U_0$) WITH EXPERIMENT MEASUREMENTS PERFORMED BY NIELSEN [7] AT $y = h/2$ AND $y = H - h/2$ (SYMMETRY PLANE).	92
FIGURE 4.58 VELOCITY DISTRIBUTION AT THE (A) AND (C) NEAR WALL REGIONS, AND AT THE (B) SYMMETRY PLANE.	93
FIGURE 4.59 RMS VELOCITY ($\sqrt{u'^2}/U_0$) DISTRIBUTION AT THE NEAR WALL REGIONS (A) AND (C), AND AT THE SYMMETRY PLANE (B).	93
FIGURE 4.60 VELOCITY PREDICTIONS (U/U_0) AT (A) $x = H$ AND (B) $x = 2H$	93
FIGURE 4.61 RMS VELOCITY PREDICTIONS ($\sqrt{u'^2}/U_0$) AT (A) $x = H$ AND (B) $x = 2H$	93
FIGURE 4.62 VELOCITY PREDICTIONS (U/U_0) AT (A) $y = h/2$, (B) $y = 0.5H$ AND (C) $y = H - h/2$	93
FIGURE 4.63 RMS VELOCITY PREDICTIONS ($\sqrt{u'^2}/U_0$) AT (A) $y = h/2$, (B) $y = 0.5H$ AND (C) $y = H - h/2$	94
FIGURE 7.1 EQUATION FOR TEMPERATURE IN A STEADY-STATE SOLVER.	121
FIGURE 7.2 EQUATION FOR TEMPERATURE IN A TRANSIENT SOLVER.	121
FIGURE 7.3 REPRESENTATION OF A 2D CONTROL VOLUME [8].	122
FIGURE 7.4 CHANNEL MESHES STUDIED (1M).	124
FIGURE 7.5 2D ANNEX 20 ROOM COARSE MESH (16650 CELLS).	125
FIGURE 7.6 2D ANNEX 20 ROOM MEDIUM MESH (76200 CELLS).	125
FIGURE 7.7 2D ANNEX 20 ROOM FINE MESH (159750 CELLS).	125
FIGURE 7.8 EVOLUTION OF U/U_0 MAXIMUM NEAR THE CEILING FOR $x = H$	126
FIGURE 7.9 EVOLUTION OF U/U_0 MAXIMUM NEAR THE FLOOR FOR $x = H$	126
FIGURE 7.10 EVOLUTION OF U/U_0 MAXIMUM NEAR THE CEILING FOR $x = 2H$	127
FIGURE 7.11 EVOLUTION OF U/U_0 MAXIMUM NEAR THE FLOOR FOR $x = 2H$	127
FIGURE 7.12 VELOCITY PROFILE (U/U_0) AT THE ROOM INLET FOR ALL MESHES.	128
FIGURE 7.13 VELOCITY PROFILE (U/U_0) AT $x = H$ AND $x = 2H$ FOR ALL MESHES.	128
FIGURE 7.14 VELOCITY PROFILE (U/U_0) AT $x=H$ AND $x=2H$, NEAR THE ROOM CEILING FOR ALL MESHES.	129
FIGURE 7.15 VELOCITY PROFILE (U/U_0) AT $x=H$ AND $x=2H$, NEAR THE ROOM FLOOR FOR ALL MESHES.	129
FIGURE 7.16 VELOCITY (U/U_0) STREAMLINES AND TEMPERATURE ISOTHERMS (T IN °C) FOR $Re = 5000$	130
FIGURE 7.17 VELOCITY (U/U_0) STREAMLINES AND TEMPERATURE ISOTHERMS (T IN °C) FOR $Re = 7100$	131
FIGURE 7.18 3D ANNEX 20 ROOM COARSE MESH (53000 CELLS).	132
FIGURE 7.19 3D ANNEX 20 ROOM MEDIUM MESH (106000 CELLS).	132
FIGURE 7.20 3D ANNEX 20 ROOM FINE MESH (462500 CELLS).	132
FIGURE 7.21 VELOCITY DISTRIBUTION AT THE NEAR WALL REGIONS AND AT THE SYMMETRY PLANE FOR THE x -COMPONENT (A,D,G), y -COMPONENT (B,E,H) AND z -COMPONENT (C,F,I).	133
FIGURE 7.22 VELOCITY DISTRIBUTION AT THE $x = H$ (A,B,C) AND $x = 2H$, FOR THE x -COMPONENT, y -COMPONENT AND z -COMPONENT, RESPECTIVELY.	133

FIGURE 7.23 VELOCITY DISTRIBUTION AT THE $y = h/2$ (A,D,G), $y = 0.5H$ (B,E,H), AND $y = H - h/2$ (C,F,I), FOR THE x -COMPONENT, y -COMPONENT AND z -COMPONENT.	134
---	-----

LIST OF TABLES

TABLE 3.1	DEFAULT MODEL COEFFICIENTS FOR STANDARD $k - \varepsilon$.	27
TABLE 3.2	OPENFOAM DEFAULT MODEL COEFFICIENTS FOR STANDARD $k - \varepsilon$.	27
TABLE 3.3	DEFAULT MODEL COEFFICIENTS FOR RNG $k - \varepsilon$.	28
TABLE 3.4	OPENFOAM DEFAULT MODEL COEFFICIENTS FOR RNG $k - \varepsilon$.	29
TABLE 3.5	DEFAULT MODEL COEFFICIENTS FOR REALIZABLE $k - \varepsilon$.	30
TABLE 3.6	DEFAULT MODEL COEFFICIENTS FOR $\overline{v'^2} - f$.	32
TABLE 3.7	OPENFOAM DEFAULT MODEL COEFFICIENTS FOR $\overline{v'^2} - f$.	33
TABLE 3.8	DEFAULT MODEL COEFFICIENTS FOR $k - \omega$.	34
TABLE 3.9	OPENFOAM DEFAULT MODEL COEFFICIENTS FOR $k - \omega$.	34
TABLE 3.10	DEFAULT MODEL COEFFICIENTS FOR $k - \omega$ SST.	36
TABLE 3.11	OPENFOAM DEFAULT MODEL COEFFICIENTS FOR $k - \omega$ SST.	37
TABLE 4.1	INLET BOUNDARY CONDITIONS.	50
TABLE 4.2	OUTLET BOUNDARY CONDITIONS.	50
TABLE 4.3	WALLS BOUNDARY CONDITIONS.	51
TABLE 4.4	NUMBER OF CELLS DISTRIBUTED BY PROCESSORS.	56
TABLE 4.5	MEAN SUPPLIED VELOCITY U_0 AND FREE-STREAM VALUES FOR THE IEA ANNEX 20 ROOM.	60
TABLE 4.6	ROOM SUPPLY OPENING BOUNDARY CONDITIONS.	60
TABLE 4.7	ROOM EXHAUST OPENING BOUNDARY CONDITIONS.	60
TABLE 4.8	ROOM WALLS BOUNDARY CONDITIONS.	61
TABLE 4.9	NUMBER OF CELLS OF THE MESHES STUDIED FOR THE ROOM GEOMETRY.	61
TABLE 4.10	CELL DISTRIBUTION BY PROCESSOR FOR THE ANNEX 20 ROOM.	65
TABLE 4.11	NON-ISOTHERMAL ROOM SUPPLY OPENING BOUNDARY CONDITIONS.	79
TABLE 4.12	NON-ISOTHERMAL ROOM EXHAUST OPENING BOUNDARY CONDITIONS.	79
TABLE 4.13	NON-ISOTHERMAL ROOM WALLS BOUNDARY CONDITIONS.	80
TABLE 4.14	TEMPERATURE GRADIENT (∇T), HEAT FLUX (q'') AND ΔT_0 FOR DIFFERENT ARCHIMEDES NUMBERS.	83
TABLE 4.15	3D ROOM SUPPLY OPENING BOUNDARY CONDITIONS.	88
TABLE 4.16	3D ROOM EXHAUST OPENING BOUNDARY CONDITIONS.	88
TABLE 4.17	3D ROOM WALLS BOUNDARY CONDITIONS.	88
TABLE 4.18	NUMBER OF CELLS OF THE MESHES STUDIED FOR THE 3D ROOM GEOMETRY.	88
TABLE 4.19	CELL DISTRIBUTION BY PROCESSOR FOR THE IEA ANNEX 20 3D ROOM.	90
TABLE 7.1	SOME DIMENSIONLESS NUMBERS	123

INDEX

1	INTRODUCTION	1
1.1	CONTEXT	3
1.2	OBJECTIVES	4
1.3	METHODOLOGY	4
1.4	STRUCTURE	5
1.5	HOST COMPANY	5
2	LITERATURE REVIEW	7
2.1	COMPUTATIONAL FLUID DYNAMICS (CFD)	9
2.2	MODELLING OF TURBULENT FLOWS	10
2.2.1	<i>DIRECT NUMERICAL SIMULATION</i>	11
2.2.2	<i>LARGE EDDY SIMULATION</i>	11
2.2.3	<i>DETACHED EDDY SIMULATION (DES)</i>	12
2.2.4	<i>REYNOLDS-AVERAGED NAVIER-STOKES SIMULATION (RANS)</i>	12
3	EQUATIONS AND NUMERICAL METHODS	17
3.1	GOVERNING EQUATIONS	19
3.1.1	<i>CONTINUITY EQUATION</i>	19
3.1.2	<i>MOMENTUM EQUATION</i>	19
3.1.3	<i>ENERGY EQUATION</i>	20
3.1.4	<i>BOUSSINESQ APPROXIMATION FOR BUOYANCY DRIVEN FLOW</i>	21
3.1.5	<i>LAW OF THE WALL</i>	22
3.2	BOUNDARY AND INITIAL CONDITIONS	23
3.3	TURBULENCE MODELLING	24
3.3.1	<i>REYNOLDS-AVERAGED NAVIER-STOKES SIMULATION (RANS)</i>	24
3.3.1.1	THE STANDARD $k - \varepsilon$ TURBULENCE MODEL	26
3.3.1.2	THE RNG $k - \varepsilon$ TURBULENCE MODEL	28
3.3.1.3	THE REALIZABLE $k - \varepsilon$ TURBULENCE MODEL	29
3.3.1.4	THE $\overline{v'^2} - f$ TURBULENCE MODEL	31
3.3.1.5	THE $k - \omega$ TURBULENCE MODEL	33
3.3.1.6	THE $k - \omega$ SST TURBULENCE MODEL	34
3.3.2	<i>MAIN CONCLUSIONS</i>	37
3.4	SOLUTION METHOD	38
3.4.1	<i>FINITE VOLUME METHODS</i>	38
3.4.2	<i>SIMPLE ALGORITHM</i>	41
3.4.3	<i>PISO ALGORITHM</i>	41
3.4.4	<i>PIMPLE ALGORITHM</i>	42
3.5	CONVERGENCE CRITERIA	42
3.6	MESHING	43
3.6.1	<i>TYPE OF NUMERICAL GRID</i>	43
3.6.2	<i>MESH QUALITY AND GENERATION</i>	44

4	TURBULENCE MODELS VALIDATION	47
4.1	TURBULENT CHANNEL FLOW	49
4.1.1	INTRODUCTION	49
4.1.2	TEST CASE SPECIFICATIONS	49
4.1.3	PRE-PROCESSING	50
4.1.3.1	BOUNDARY CONDITIONS	50
4.1.3.2	TURBULENCE MODEL AND NUMERICS	51
4.1.3.3	MESH INDEPENDENCE	52
4.1.3.4	SOLVER	54
4.1.3.5	PARALLEL RUNNING	55
4.1.4	POST-PROCESSING	56
4.1.4.1	RESIDUALS AND CONVERGENCE	56
4.1.4.2	RESULTS	57
4.1.4.3	CONCLUSIONS	58
4.2	2D ISOTHERMAL TEST CASE IN ANNEX 20	59
4.2.1	INTRODUCTION	59
4.2.2	TEST CASE SPECIFICATIONS	59
4.2.3	PRE-PROCESSING	60
4.2.3.1	BOUNDARY CONDITIONS	60
4.2.3.2	MESH INDEPENDENCE	61
4.2.3.3	PARALLEL RUNNING	65
4.2.3.4	SOLVER	66
4.2.3.5	TURBULENCE MODELS AND NUMERICS	68
4.2.4	POST-PROCESSING	73
4.2.4.1	RESIDUALS AND CONVERGENCE	73
4.2.4.2	RESULTS	74
4.2.4.3	CONCLUSIONS	77
4.3	2D NON-ISOTHERMAL TEST CASE IN ANNEX 20	78
4.3.1	INTRODUCTION	78
4.3.2	TEST CASE SPECIFICATIONS	78
4.3.3	PRE-PROCESSING	79
4.3.3.1	BOUNDARY CONDITIONS	79
4.3.3.2	SOLVER	80
4.3.3.3	TURBULENCE MODEL AND NUMERICS	82
4.3.4	POST-PROCESSING	83
4.3.4.1	RESULTS	83
4.3.4.2	CONCLUSIONS	86
4.4	3D ISOTHERMAL TEST CASE IN ANNEX 20	87
4.4.1	INTRODUCTION	87
4.4.2	TEST CASE SPECIFICATIONS	87
4.4.3	PRE-PROCESSING	88
4.4.3.1	BOUNDARY CONDITIONS	88
4.4.3.2	MESH INDEPENDENCE	88
4.4.3.3	PARALLEL RUNNING	90

4.4.3.4	TURBULENCE MODELS AND NUMERICS	91
4.4.4	POST-PROCESSING	91
4.4.4.1	RESULTS	91
4.4.4.2	CONCLUSIONS	94
5	CONCLUSIONS AND FUTURE WORK	95
5.1	CONCLUSIONS	97
5.2	FUTURE WORK	98
6	BIBLIOGRAPHY AND OTHER SOURCES OF INFORMATION	99
7	ANNEXES	119
7.1	ANNEX 1 - T EQUATION IN OPENFOAM	121
7.2	ANNEX 2 -PRESSURE AND VELOCITY CORRECTIONS [8]	122
7.3	ANNEX 3 - DIMENSIONLESS NUMBERS	123
7.4	ANNEX 4 - 2D CHANNEL FLOW	124
7.5	ANNEX 5 - 2D ISOTHERMAL TEST CASE	125
7.6	ANNEX 6 - 2D NON-ISOTHERMAL TEST CASE	130
7.7	ANNEX 7 - 3D ISOTHERMAL TEST CASE	132

INTRODUCTION

- 1.1 CONTEXT
- 1.2 OBJECTIVES
- 1.3 METHODOLOGY
- 1.4 STRUCTURE
- 1.5 HOST COMPANY

1 INTRODUCTION

1.1 Context

Accurate prediction of ventilation flow is essential for designing a healthy, comfortable, and energy-efficient indoor environment [9].

Energy consumption in residential and commercial air-conditioning-related sectors represents about 40% of the primary energy consumption in the world [10]. In Portugal, approximately 47% of the total energy consumption in residential buildings is for space heating and cooling [11] and in services, approximately 62% of the energy total consumption is for space heating and cooling (data for 2018) [12]. The International Energy Agency (IEA) offers no official data about the segmentation of energy consumption in industrial buildings. However, about 29% of the energy total final consumption in the world is for industry (being $\approx 42\%$ electricity consumption) [10]. In Portugal, the situation is similar, 28% of the energy total final consumption is for industry (being $\approx 34\%$ electricity consumption) [13]. The consideration of energy consumption of industrial buildings mainly focuses on the heating, ventilation, and air conditioning (HVAC) systems [14].

The optimization of HVAC systems, as well as the effectiveness improvement of comfort parameters for the occupants, are crucial to reach CO_2 emission reduction targets. The forecast of these parameters is of extreme importance for calculating the building energy consumption, ergo in the decision making by the design team when it comes to the best technical-economic option to pursue. A major design objective is to ensure that air ventilation is delivered from a limited number of supply openings to every part of a space in an effective and efficient manner [15]. As buildings have become more complex, for these geometries or even complex boundary conditions, it is possible to use, more frequently, numerical methods. In this sense, the purpose of this dissertation is to study some important aspects of HVAC systems design parameters, such as pressure, velocity, and temperature distribution in order to achieve energy efficiency targets on a space, based on computational fluid dynamics (CFD) models.

The set-up, simulation, and analysis of several benchmark test cases, will contribute to the validation of models and methodology with the aim being the ventilation study of an industrial building with considerable temperature stratification. CFD is often used in situations when experimentation is not possible. It allows scientists to test different scenarios and retrieve more information of physical phenomena. However caution must be taken, as Li and Nielsen [15] suggested "CFD has not become a replacement for experi-

ment and theoretical analysis in ventilation research, rather it has become an increasingly important partner.”.

1.2 Objectives

The objectives of the present dissertation can be divided into two primary categories, namely the validation of turbulence models and the development of a CFD work-flow to study the ventilation effectiveness in air-conditioned spaces. This work is implemented mainly in open-source software, because of its flexibility (possible to make changes to meet specific needs), quality, since there are thousands of users going through the code errors are more often detected and quickly corrected, shared knowledge (a lot of documentation is available) and because it's free. To achieve these goals, some factors must be taken into account:

- Define a work-flow for the geometry and meshing;
- Select the proper OpenFOAM solver;
- Validation of existing turbulence models in the OpenFOAM code for isothermal and non-isothermal calculations of airflows in indoor environments;
- Perform convergence studies;
- Perform Benchmark tests for indoor environments;
- Set-up and simulation of a case study.

1.3 Methodology

In order to achieve the objectives defined for this dissertation, the methodology followed was:

- Investigation of computational fluid dynamics general applications. Focus on indoor environments applications.
- Investigation and selection of turbulence models.
- Selection of mesh design tools, CFD software and post-processing tools.
- Selection and analysis of benchmarks/case studies.
- Pre-Processing, simulation and post-processing of benchmark studies. Mesh generation and cases set-up; Running the cases, monitoring and control; data extraction, benchmark results comparison and data analysis.
- Work-flow validation for the case study.
- Set-up and simulation of the case study, critical analysis of the results.

1.4 Structure

This dissertation is divided into four chapters, as follows:

- Chapter 1 - Introduction, aims to introduce the dissertation's subject and its context. The objectives, structure and methodology are described in this chapter. Since this paper was carried out under a curricular internship, the host company is also here presented.
- Chapter 2 - Literature Review, provides a brief history about computational fluid dynamics. This chapter also includes a theoretical framework to different ways of approaching the modelling of turbulent flows;
- Chapter 3 - Equations and Numerical Methods, in this chapter some basics of computational fluids dynamics are studied: governing equations, some assumptions and approximations; boundary conditions; and some two-equations, eddy-viscosity models based on the Reynolds averaged Navier-Stokes equations (RaNS models).
- Chapter 4 - Turbulence Models Validation, aims to present the performed benchmark simulation results. The results are reviewed and critically evaluated in the context of the literature and the present knowledge about the subject.
- Chapter 5 - Conclusions and Future Work, aims to summarize the main conclusions and to present some future work ideas and/or improvements to be made.

1.5 Host Company

This study is the outcome of a curricular internship that took place at **Paulo Queirós de Faria - Engenheiros Consultores, Lda (PQF)**, specialized in building physics, performance and services consultancy, specially HVAC projects, energy consumptions analysis and thermal comfort.

LITERATURE REVIEW

2.1 COMPUTATIONAL FLUID DYNAMICS (CFD)

2.2 MODELLING OF TURBULENT FLOWS

2 LITERATURE REVIEW

2.1 Computational Fluid Dynamics (CFD)

CFD was firmly established in the aerospace, automotive and power generation sectors. Subsequently, it has spread throughout engineering industry [16]. The increase in computational power, specially in the last decade, has contributed to the simulation of cases with more complex geometries and elaborate boundary conditions, with a significant reduction of the time spent simulating. A recent revolutionary CFD simulation was conducted by Professor Bert Blocken of Eindhoven University of Technology entitled *The Peloton Project*. Blocken et al. [17] conducted the first aerodynamic simulation and wind tunnel test of a full peloton of 121 cyclists. With almost 3 billion calculation cells, the Peloton Project simulation was the largest ever in sports and the largest using commercial CFD software [18].

CFD has become one of the most powerful tools in ventilation research. The very first predictions of room air movement were made in the '70s. Nielsen [7, 19] presented an early CFD prediction of flow in a ventilated room by showing the great advantage of flexibility in choosing the configuration and boundary conditions. His work became a fundamental reference to the majority of the indoor ventilation research that follow. A cooperative work performed under the IEA for the Energy Conservation in Buildings and Community Systems Programme, was developed by researchers from 13 different countries [6] with the aim of evaluating the performance of single- and multi-zone air and contaminant flow simulation techniques, and to establish their viability as design tools. This project has become known as *Annex 20: Air Flow Patterns within Buildings* and it consolidates the information from the technical reports and papers produced within this subtask, in such a manner that it serves as entry to more detailed papers, such as Nielsen [20, 21]. Jones and Whittle [22] reviewed the application of CFD to building environmental design, by analysing the major technical issues, status and capabilities of the '90s. In the beginning of the twenty-first century, Russell and Surendran [23] have reviewed work on the subject, including one of the first simulations of the thermal mannequin case [24]. In 1996, Baskaran and Kashef [25] presented the application of CFD for modelling wind environmental conditions around a variety of building configurations. The examined configurations included, wind flow around a single building, flow between parallel buildings and air flow around multiple building configurations. They attempted for the first time ever to simulate the surrounding landscape such as the hills and trees, accounting with

far more than the buildings. Wind tunnel studies were used for model validation, but also data from open country exposure, using the power law and normal wind flow condition, for the comparison. This paper used a number of cells, which at that time would be considered high, however, now that mesh would still be considered coarse, due to the massive increase of computational capacity in the last two decades. This evolution allowed for CFD cases to become more detailed and representative of the physical phenomena of the real case to study. With CFD it is possible to study specific situations, such as night ventilation as a way of cooling office buildings and provide comfort in summer [26] and, therefore, retrieve more detailed conclusions about the strategies that can be more efficient and advantageous to follow.

In 2003, Sørensen and Nielsen [27] discussed modelling aspects of turbulence and boundary conditions, as well as aspects related to numerical errors, with emphasis on choice of differencing scheme and computational grid. Both the development of CFD models for room air movement and progress in general fluid dynamics research are still strongly influenced by the increase computer power that has been available for the past few decades [5]. In 2010, Goethals and Janssens [28] studied the impact of different inlet and outlet orientations in indoor air flow patterns.

The evaluation of indoor air environment has been one of the main targets in ventilation design, from the start of CFD applications. Simulations of mechanical ventilation in buildings became a common practice [29, 30, 31]. However, due to energy consumption reduction targets, natural ventilation studies have also significantly increased [32, 33, 34, 35, 36, 37].

Only in the last three years, CFD simulation of air flow in indoor environments have significantly increased. Inspired by the impact of COVID-19, many researchers and scientists have reviewed, updated and re-simulated previous papers about pathogen transmission. This new wave of research papers includes research from subjects such as saliva particulate transport during human cough with and without facial masks [38], to more direct studies involving air conditioning systems, such as the one done by Bhattacharyya et al. [39] that investigates the effectiveness of conditioned air released from air-conditioning machines to mix with aerosol sanitizer to reach every point of the space of the isolation room so as to kill the COVID-19 virus.

In 2015, Ito et al. [40, 41, 24] reviewed and compared performance and results for two benchmark tests, from the IEA Annex 20, for six different commercial CFD codes. Some IEA Annex 20 benchmarks will be part of this dissertation studies.

In order to understand and properly implement CFD methods, some basic contents have to be initially examined. This is the subject of the following sections.

2.2 Modelling of Turbulent Flows

Flows that include turbulence are difficult to describe exactly mathematically, therefore it is costume to use semi-empirical models to represent this phenomena. These are called turbulence models. These models combined with simplifications such as the Boussinesq approximation affect the accuracy of the solution, thereupon, care is needed when draw-

ing conclusions from calculations in which these models are used [42].

Turbulence models predict eddy viscosity as a function of position in the flow. They do it so by solving a set of transport equations for properties of the turbulence. These transport equations are not exact laws of fluid motion, they contain a degree of empiricism that is designed to allow predictions of engineering accuracy in many, although not all, situations [43].

2.2.1 Direct Numerical Simulation

The Direct Numerical Simulation (DNS) of turbulence consist in solving numerically the Navier-Stokes equations in such a way as to resolve all the essential turbulent scales [44]. The principal advantage of DNS is that it provides extremely detailed information about the flow, such as turbulence intensities, vorticity, fluctuations, Reynolds stresses, their budget terms, along with others [45]. In addition, it is possible to specify the case parameters (inflow, boundary conditions, etc.) more accurately [46], which can be very useful.

Moin and Mahesh [47], Perić and Ferziger [48], Lee and Moser [49], among others, concluded that DNS must be used as a research tool and not as brute-force solution to the Navier-Stokes equations for engineering problems. DNS spends most of the computational effort on resolving scales that are not very important for determining second-order quantities such as the Reynolds stresses and the scalar flux [50]. This degree of detail contributes to a highly time-consuming data generation and requires a large computational capacity. For example, Wu and Moin [51], to simulate a simple case of a fully developed incompressible pipe flow with a relatively small number of cells, required for:

- $Re \approx 5300$, 128 processors on 16 IBM 8-way P655+nodes;
- $Re \approx 44000$, 1024 processors on 128 IBM 8-way P655+nodes.

Furthermore, in DNS large memory to store data is required. In this case, it was achieved up to 25 GB of data per iteration datafile.

Another well known limitation of DNS is its restriction to low Reynolds numbers. Most of the cases use Reynolds numbers up to ≈ 6000 and simple geometries (channel flows, backward-facing step case and free jets) [52, 45, 53].

More recently, and due to the advances in computer power, more complex cases, such as the ones including heat transfer have been simulated with DNS [54].

2.2.2 Large Eddy Simulation

Large Eddy Simulation (LES) attempts to overcome the limitations of DNS by resolving some eddies (largest scale), while the effects of the smaller scale (sub-grid scale (SGS)) motions are modelled. LES is an unsteady, three-dimensional simulation methodology [55].

In LES, the dependent variables are time-dependent, therefore the equations must be

solved transiently. This is the main reason why LES is much more expensive than Reynolds-averaged Navier-Stokes (RaNS) [56]. In spite of LES being much more costly than RaNS, it is also more accurate.

The conceptual steps for LES are presented with more detail by Pope [50]. LES has been widely used for not only turbulent flow analysis but also for combustion, aeroacoustics, and more. A great majority of large-eddy simulation include external flows around buildings [57, 58, 59] and combustion [60, 61].

“Good” LES will resolve at least 80% of the turbulent kinetic energy [62], which inevitably requires an advanced and accurate SGS model to properly model the effects of SGS motions. Pope [61] discussed the development of a numerical algorithm and solver capable of performing large-eddy simulation in the very complex geometries and high Reynolds numbers, two of the main issues of LES. In addition, in most practical engineering flows, performing a wall resolved LES is too big of a task due to large Reynolds number, since the log-law will not hold as in RaNS [62, 63].

2.2.3 Detached Eddy Simulation (DES)

Detached Eddy Simulation (DES) was created in 1997 to address the challenge of considerably separated flows at high Reynolds number. DES was defined with intent of combining the strengths of Reynolds-averaged methods and of Large-Eddy Simulations, in a non-zonal manner [64, 65]. Spalart [66] proposed a “*working definition*” of DES, which states “*that the boundary layer is treated by RaNS, and regions of massive separation are treated with LES; the space between these areas, known as the gray area, may be problematic unless the separation is abrupt, often fixed by the geometry*”(p.183).

DES has been shown good results, specially when applied to aerodynamics such as performance of airfoils and winged bodies [65, 67, 68, 69], propulsive jets [70], gases dispersion [71] and aeroacoustic of high lift devices and landing gears [72, 73, 74, 75, 76, 77].

The main advantage of DES over LES in case of external flows, is its requirement of lesser number of nodes because unsteadiness dominates predominately over a small region around the body [78].

2.2.4 Reynolds-averaged Navier-Stokes Simulation (RaNS)

The vast majority of CFD simulations has been carried out with procedures based on the Reynolds-averaged approach to the Navier–Stokes equations [16]. Usually, the averaged properties of the flow, provide sufficient information for most engineering purposes. RaNS methods require much less computational capacity when compared with LES or DNS, therefore remain the first choice for most industrial CFD users [79].

The base of RaNS methods is the Reynolds decomposition [48]. These fluctuating components of the velocity give rise to the Reynolds stresses, which are computed by turbulence models. Most RaNS models use the *Boussinesq hypothesis* (linear eddy-viscosity models (EVMs)) for the viscosity [80] or non-linear eddy viscosity formulations [81]. Non-linear EVMs were developed to combine computational robustness and efficiency of lin-

ear EVMs with improved accuracy of second moment closures [82]. Others do not use these hypotheses and are far superior to the EVMs, the Reynolds-stress models. However, they are much more complex, numerically unstable and require a higher computer capacity [83].

Figure 2.1 shows different groups of turbulence models and their relative computational cost.

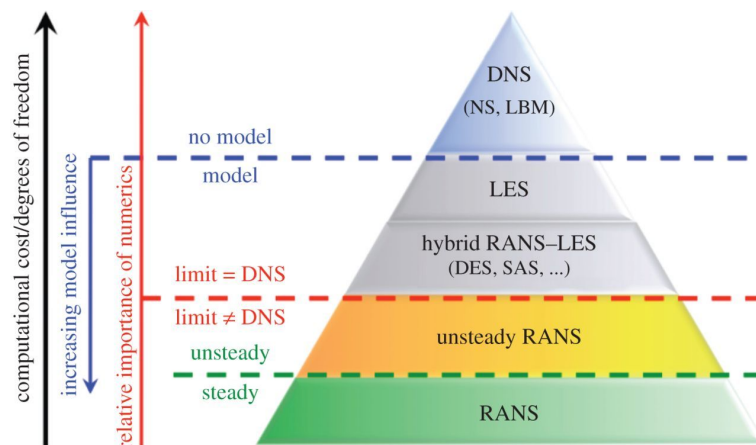


Figure 2.1 – Multiscale and Multiresolution approaches for turbulence [1]

The RaNS turbulence models are usually classified on the basis of the number of additional transport equations that need to be solved along with the flow equations [16]. Some examples are: the zero-equation (Mixing length), one-equation (Spalart-Allmaras), two-equation ($k - \varepsilon$, $k - \omega$, $q - \zeta$), three-equation ($k - kl - \omega$), four-equation ($\gamma - Re_\theta$, $\overline{v'^2} - f$), seven-equation (Reynolds Stress Models) etc.

$k - \omega$ and $k - \varepsilon$ are the more common "families" of RaNS turbulence models used.

Historically, the $k - \omega$ appear first, however this version proposed by Kolmogorov in 1942 [84] was somewhat brief and didn't establish values for all of the closure coefficients. In 1970, Saffman [85] proposed a superior formulation for the $k - \omega$ model that has served as the basis for the $k - \omega$ turbulence models that followed. Since 1970, several formulations of the $k - \omega$ model were proposed, such as the more known Wilcox's $k - \omega$ model versions [86, 87, 2] and Menter's [88] formulation of the $k - \omega$ Shear Stress Transport.

The $k - \omega$ model is mostly used in aerodynamics and turbo machinery [89, 90] for two main reasons, doesn't require any wall-damping functions nor the computation of wall distances, and it models near-wall interactions more accurately than $k - \varepsilon$ models. The $k - \omega$ model is superior to $k - \varepsilon$ in the treatment of the viscous near-wall region, and in accounting for the effects of streamwise pressure gradients [50]. The $k - \omega$ model has, however, a major drawback, it is very sensitive to free-stream boundary conditions [88, 91, 92].

The $k - \omega$ SST (Shear Stress Transport) model it is a combination of the $k - \omega$ model (in the inner boundary layer) and the standard $k - \varepsilon$ model (in the outer region) [93]. This model has been successful for flows with moderate adverse pressure gradients, but fails

for flows with pressure induced separation [94]. Although, the $k - \omega$ SST model is still sensitive to free-stream boundary conditions [88].

The earliest development efforts of the $k - \varepsilon$ model were made by Chou [95] in 1945, but similarly to what happened with the $k - \omega$ formulation, it wasn't until 1972 that Jones and Launder [96] presented the very first complete formulation of the $k - \varepsilon$, this version would be adjusted two years later, regarding the model's closure coefficients, by Launder and Spalding [97] and this what is currently known as the standard $k - \varepsilon$ model. Besides the standard $k - \varepsilon$ model, some well known variants exist, such as the realizable $k - \varepsilon$ [98] and the RNG $k - \varepsilon$ [99, 100] models.

The standard $k - \varepsilon$ model has shown to be reliable in the prediction of both near-wall and free-shear-flow phenomena, with relatively small pressure gradients [97]. However, when it comes to problems involving adverse pressure gradients, large separations, and complex flows with strong curvatures, the model might not yield accurate predictions [101]. The standard $k - \varepsilon$ model has proven to be reliable and robust for many engineering applications [102]. This model has shown good results in air ventilation performance [103, 104, 31]

The realizable $k - \varepsilon$ model was developed with the aim of solving some of the standard $k - \varepsilon$ limitations, such as the performance for flows with a high mean shear rate or a massive separation, which in the cases of the eddy viscosity is over-predicted by the standard eddy viscosity formulation [105]. The realizable $k - \varepsilon$ model has been tested for different turbulent flow calculations and it has shown good agreement with the experimental data for:

- Rotating homogeneous shear flows. The realizable $k - \varepsilon$ is better in predicting rotation flows. The standard $k - \varepsilon$ model does not show the effects of rotation, as it gives the same growth rate of turbulent kinetic energy as in cases with no rotation [98, 106, 107].
- Boundary-free shear flows (mixing layer, planar and round jet). For the first two, the realizable $k - \varepsilon$ has shown significant improvements in the prediction of turbulent kinetic energy and the Reynolds shear stress distributions, specially for their peak levels. For round jets, both the standard and the realizable $k - \varepsilon$ predictions agree well with the experimental data, however the standard $k - \varepsilon$ predicts a wider distribution of the mean velocity profile [108, 109, 110, 111].
- Good predictions of the recirculation zone near walls [112, 113], specially in benchmarks as the backward-facing step [114, 115]
- Channel flow and boundary layer flows. In these case, the predictions for the realizable and standard $k - \varepsilon$ model are very similar and little improvement is observed [105, 116].

RNG $k - \varepsilon$ model is another well known $k - \varepsilon$ model formulation, here the effective viscosity accounts for low-Reynolds number effects [100]. The model has showed good agreement with experimental measurements in modelling different configurations of swirling

flow [117, 118], homogeneous shear flows [119, 100], supersonic axisymmetric separated base flows [120], engine flows [121, 122, 123] and external flows [124, 125]. Good agreement with experimental data has also been found for indoor environments ventilation [126, 127, 128].

In the next chapter, focus will be given to the formulation of some RaNS models based on the eddy viscosity assumption, as some basic notions needed to develop a CFD case.

EQUATIONS AND NUMERICAL METHODS

- 3.1 GOVERNING EQUATIONS
- 3.2 BOUNDARY AND INITIAL CONDITIONS
- 3.3 TURBULENCE MODELLING
- 3.4 SOLUTION METHOD
- 3.5 CONVERGENCE CRITERIA
- 3.6 MESHING

3 EQUATIONS AND NUMERICAL METHODS

3.1 Governing Equations

CFD is fundamentally based on the *governing equations of fluid flow* [129]. They are a mathematical representation of the conservation laws of physics. Understanding the governing equations it is necessary to numerically solve a fluid flow. These equations are the continuity (eq. 3.1), momentum (eq. 3.8) and energy (eq. 3.12) equations [16].

3.1.1 Continuity Equation

The differential equation of mass conservation or *continuity equation* does not require assumptions except that the density and velocity are continuum functions. The continuity equation (eq. 3.1), is a general expression of the overall mass conservation requirement, and it must be satisfied at every point in the fluid [130].

$$\frac{\partial \rho}{\partial t} + \nabla \cdot (\rho \mathbf{u}) = 0 \quad (3.1)$$

where ρ is the density of the fluid and \mathbf{u} is the velocity vector.

For steady flow, this law requires that the net rate at which mass enters a control volume must equal zero. Furthermore, considering an incompressible fluid, where ρ is a constant it yields [131]:

$$(\nabla \cdot \mathbf{u}) = \frac{\partial u}{\partial x} + \frac{\partial v}{\partial y} + \frac{\partial w}{\partial z} = 0. \quad (3.2)$$

where u , v and w are the x , y and z -components of the velocity.

3.1.2 Momentum Equation

Conservation of linear momentum can be presented as a general differential equation known as the **Cauchy's Equation**:

$$\frac{\partial}{\partial t}(\rho \mathbf{u}) + \nabla \cdot (\rho \mathbf{u} \mathbf{u}) = \rho \mathbf{g} + \nabla \cdot \sigma_{ij} \quad (3.3)$$

Cauchy's equation (eq. 3.3) is not very useful as it is, because the stress tensor σ_{ij} , contains more unknown variables than equations. To the problem be solvable it is necessary

six more equations. These equations are called *constitutive equations* [132], and they allow to write the stress tensor as:

$$\sigma_{ij} = \underbrace{\tau_{ij}}_{\text{viscous stresses}} - \underbrace{p\mathbf{I}}_{\text{pressure stresses}} \quad (3.4)$$

If it is assumed that the flow is isothermal and incompressible, then:

$$\tau_{ij} = \mu \left(\frac{\partial u_i}{\partial x_j} + \frac{\partial u_j}{\partial x_i} \right) \quad (3.5)$$

Substituting equation 3.5 and equation 3.4 into the Cauchy's equation (eq. 3.3), is possible to obtain, for example, for the x-component:

$$\rho \frac{du}{dt} = -\frac{\partial p}{\partial x} + \rho g_x + \mu \left[\frac{\partial}{\partial x} \left(\frac{\partial u}{\partial x} + \frac{\partial v}{\partial y} + \frac{\partial w}{\partial z} \right) + \underbrace{\left(\frac{\partial^2 u}{\partial x^2} + \frac{\partial^2 u}{\partial y^2} + \frac{\partial^2 u}{\partial z^2} \right)}_{\text{Laplacian of velocity component u}} \right] \quad (3.6)$$

= 0, due to continuity equation for incompressible flow

Therefore, the momentum equation of the x-component can be written as:

$$\rho \frac{du}{dt} = -\frac{\partial p}{\partial x} + \rho g_x + \mu \nabla^2 u \quad (3.7)$$

Combining the three components into one vector equation the result is the **Navier-Stokes Equations** for incompressible flow with constant viscosity:

$$\rho \frac{d\mathbf{u}}{dt} = \rho \mathbf{g} - \nabla p + \mu \nabla^2 \mathbf{u} \quad (3.8)$$

Equation 3.8 still has 4 unknowns (3 velocity components and pressure), thus it's necessary another equation to make the problem solvable, the incompressible continuity equation (eq. 3.2).

3.1.3 Energy Equation

In the most cases, temperature variations are significant and considerations must be taken when preparing a CFD case. The main issue is that the energy and momentum equations are coupled and must be solved simultaneously. Fortunately, the coupling is not usually so strong that will withhold the solution of the equations in sequential approach [48, 8].

CFD codes generally do not consider radiation and radiation heat transfer, since its up to the user to choose if, considering radiation is relevant or not. When consider, its usually implemented by radiation models [133]. The following form of the energy equation will not have into account radiation or radiation heat transfer.

In most CFD codes, such as Ansys Fluent, COMSOL and OpenFOAM can deal with the energy equation as total energy, internal/thermal energy or energy equation in terms of

enthalpy (useful for chemical reactions and combustion). The thermal energy/internal energy (e) equation is:

$$\underbrace{\frac{\partial(\rho e)}{\partial t}}_{\text{Unsteady}} + \underbrace{\nabla \cdot (\rho \mathbf{u} e)}_{\text{Convection}} = - \underbrace{\nabla \cdot \mathbf{q}}_{\text{Diffusion}} + \underbrace{S_e}_{\text{Source}} \quad (3.9)$$

where $e = c_p T$ and the heat flux is $\mathbf{q} = -k_{cond} \nabla T$ (Fourier's Law)[131]. Equation 3.9 is not sufficient for compressible flows where the flow speed is high. Internal energy can be converted into mechanical/kinetic energy (K). The kinetic energy of the flow (per unit mass) is:

$$K = \frac{1}{2} (\mathbf{u} \cdot \mathbf{u}) = \frac{1}{2} (|\mathbf{u}|)^2 \quad (3.10)$$

The kinetic energy (K) can be written in form of a differential equation, after a derivation process [134], as:

$$\frac{\partial(\rho K)}{\partial t} + \nabla \cdot (\rho \mathbf{u} K) = \underbrace{\nabla \cdot (\boldsymbol{\sigma} \cdot \mathbf{u})}_{\text{Strain energy}} + \underbrace{\rho \mathbf{g} \cdot \mathbf{u}}_{\text{Potential energy}} \quad (3.11)$$

Now, the differential total energy (E) equation can be obtain, by simply adding the internal (e) and kinetic energy (K) equation, $E = e + K$, and considering the decomposition of the total stress tensor (eq. 3.4), it yields:

$$\frac{\partial(\rho E)}{\partial t} + \nabla \cdot (\rho \mathbf{u} E) + \nabla \cdot (p \mathbf{u}) = -\nabla \cdot \mathbf{q} + S_e + \nabla \cdot (\boldsymbol{\tau} \cdot \mathbf{u}) + \rho \mathbf{g} \cdot \mathbf{u} \quad (3.12)$$

This is the form used by density-based solvers (compressible flows), pressure-based solvers use the internal energy equation, rather than the total energy equation.

3.1.4 Boussinesq Approximation for Buoyancy Driven Flow

Density it is often assumed to vary linearly with temperature. However if the variation is not large, it is possible to neglect the density in the unsteady and convection terms, but not in the gravitational term [80]. This is called the **Boussinesq approximation**. It is also a standard practice to use the kinematic pressure in incompressible flow solvers:

$$p_k = \frac{p}{\rho_0} \quad (3.13)$$

and therefore the continuity and Navier-Stokes equations can be written as follows:

$$\nabla \cdot \mathbf{u} = 0 \quad (3.14)$$

$$\frac{\partial \mathbf{u}}{\partial t} + \nabla \cdot (\mathbf{u} \cdot \mathbf{u}) = -\nabla p_k + \nu \nabla^2 \mathbf{u} + \underbrace{\frac{\rho \mathbf{g}}{\rho_0}}_{\text{Buoyancy force term}} \quad (3.15)$$

This approximation assumes that the density can be written on the form:

$$\rho \approx \rho_0 [1 - \beta(T - T_0)], \quad (3.16)$$

where β is the coefficient of volumetric expansion.

Thus the buoyancy force term can be computed as:

$$\frac{\rho \mathbf{g}}{\rho_0} \approx [1 - \beta(T - T_0)] \mathbf{g} \quad (3.17)$$

By implementing this approximation, the memory requirement is reduced, because the density has been removed from the Navier-Stokes equation. In addition, the degree of non-linearity of the Navier-Stokes equations is reduced, contributing to a more stable simulation.

This approximation introduces errors of the order of 1% if the temperature differences ($T - T_0$) are below 2°C for water and 15°C for air [48].

The equation can be now written as:

$$\frac{\partial \mathbf{u}}{\partial t} + \nabla \cdot (\mathbf{u}\mathbf{u}) = -\nabla p_k + \nu \nabla^2 \mathbf{u} + \underbrace{(1 - \beta(T - T_0)) \mathbf{g}}_{\text{buoyancy}} \quad (3.18)$$

Is still necessary to solve some form of the energy equation to compute the temperature. In OpenFOAM, the temperature equation is defined in **TEqn.H**, its definition can be found in 7.1 - Annex 1.

3.1.5 Law of the wall

The law of the wall is one of the most famous empirically-determined relationships in turbulent flows near solid boundaries. According to the classical law of the wall [135], within the viscous inner layer adjacent to the wall, the molecular viscosity is dominant and the turbulence-eddy viscosity is neglected [136]. The mean stream-wise velocity can be approximately expressed by a linear relation:

$$u^+ = y^+ \quad (3.19)$$

In the logarithmic sublayer, it can be assumed that the turbulence eddy viscosity is dominant, whereas the molecular viscosity is negligible. The streamwise velocity can be approximately described by the most widely used law of the wall, the semi-logarithmic relation (log-law) [137]:

$$u^+ = \frac{1}{\kappa} \ln(y^+) + C \quad (3.20)$$

where κ is the von Karman constant, C is the constant of integration. The values of $\kappa \approx 0.41$ and $C \approx 5.0$ have been widely used for all the wall-bounded flows and incorporated in almost all CFD turbulence models [138]. y^+ is non-dimensional wall distance for a wall-bounded flow.

$$y^+ = \frac{u_\tau y}{\nu} \quad (3.21)$$

Bradshaw and Huang [139] presented typical values for y^+ and the constant C as well as more detailed formulation of the log law for both velocity and temperature.

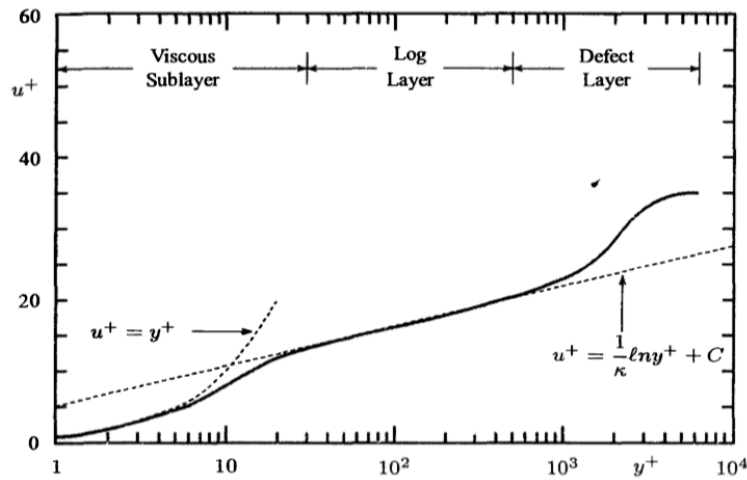


Figure 3.1 – Typical velocity profile for a turbulent boundary layer.[2]

3.2 Boundary and Initial Conditions

The laws of motion are incomplete without boundary conditions, they indicate how the user includes the specific physical phenomena into the mathematical model [83]. Boundary conditions are appropriate constraints that must be specified on the surfaces that bound a computational domain [43].

To the system can be physically correct and properly solved, the combinations of the boundary conditions should be close to the real scenario as much as the CFD software allows, in order to prevent incorrect predictions, and even solver failure.

There are a lot of boundary conditions in CFD codes and OpenFOAM provides a wide range, such as, geometry constraints, inlet, outlet, wall and coupled conditions, and also, general conditions for patches and fields.

Special attention must be given to the following boundary conditions:

- **General conditions.** Boundary conditions are usually reduce to one of the following types:
 - Dirichlet: fixed value, $\phi_f = \phi_{ref}$.
 - Neumann: fixed gradient, $\phi_f = \phi_c + \Delta \nabla \phi_{ref}$.
 - Mixed: linear combination of Dirichlet and Neumann, $\phi_f = w\phi_{ref} + (1 - w)(\phi_c + \Delta \nabla \phi_{ref})$
- **Geometry constraints boundary conditions.** The geometry setting of a CFD model refers to the size of the computational domain along with sizes and locations of all the solid objects. Some cases can be "geometrically" simplified, e.g. a 3D/2D geometry can be converted into a 2D/1D geometry, if physically the case remains feasible; symmetric and cyclic conditions can sometimes be used, etc.

- **Inlet conditions.** The way air is supplied affects the airflow pattern in a room, therefore inlet conditions are the most important. Variables usually defined at the inlet are, the velocity, pressure, temperature and turbulence conditions.
- **Outlet conditions.** An outlet generally has little impact on room airflow. However, the conditions set for the outlet can have a significant influence on the numerical stability of the simulation.
- **Wall conditions.** Solid surfaces in an indoor space, such as walls, ceilings, floors, and the objects surfaces, are all classified as walls.

Nielsen et al. [5] approaches a specific set of boundary and initial conditions more frequently implemented in CFD ventilation design.

3.3 Turbulence Modelling

Turbulence modelling comes instead of simulating all of the scales of the Navier-Stokes equations in space and time. Approximations are going to be made, that allow to obtain engineering quantities of interest much more efficiently.

3.3.1 Reynolds-averaged Navier-Stokes Simulation (RaNS)

When solving all scales of the Navier-Stokes equations in space and time (DNS) isn't always necessary or possible, when LES is infeasible to use (e.g. 2D simulations) or when we just want to get some engineering quantities of interest such as average velocity or temperature in a room it is much more efficient to use Reynolds-averaged Navier-Stokes (RaNS) based turbulence models.

By using RANS, the computational costs can be reduced by solving the statistically averaged equation system. The present study will take focus on a few two-equations models, which are models that prevail in calculations of indoor airflows [140].

In RaNS, the governing equations are the continuity and Navier-Stokes equations combined with a model for the fluctuations ($\mathbf{u}'(\mathbf{x}, t)$). The Reynolds averaging approach to the Navier-Stokes equations base idea is to take the Reynolds decomposition of the pressure ($p(\mathbf{x}, t)$) and velocity field $\mathbf{u}(\mathbf{x}, t)$,

$$p(\mathbf{x}, t) = \bar{p}(\mathbf{x}) + p'(\mathbf{x}, t) \quad (3.22)$$

$$\mathbf{u}(\mathbf{x}, t) = \mathbf{U}(\mathbf{x}) + \mathbf{u}'(\mathbf{x}, t) \quad (3.23)$$

and plug it into the Navier-Stokes equations,

$$\frac{\partial \mathbf{u}}{\partial t} + (\mathbf{u} \cdot \nabla) \mathbf{u} = -\nabla p + \frac{1}{Re} \nabla^2 \mathbf{u} \quad (3.24)$$

and continuity equation (e.g. incompressible flow),

$$\nabla \cdot \mathbf{u} = 0 \quad (3.25)$$

and average these equations to get a simplified equation of just the mean flow $\mathbf{U}(\mathbf{x}, t)$ to obtain a simpler set of equations to solve, that is less expensive but provide a large scale of information (average lift, average velocity, separation point of the flow over an airfoil, etc.). From the full derivation [141] we get the momentum equation (x -component) in terms of the mean and fluctuating components of the velocity field:

$$U \frac{\partial U}{\partial x} + V \frac{\partial U}{\partial y} + W \frac{\partial U}{\partial z} + \underbrace{\left(\frac{\partial \overline{u'u'}}{\partial x} + \frac{\partial \overline{u'v'}}{\partial y} + \frac{\partial \overline{u'w'}}{\partial z} \right)}_{\text{Reynolds stresses}} = -\nabla \bar{p} + \frac{1}{Re} \nabla^2 \mathbf{U} \quad (3.26)$$

or, in a more embracing form:

$$U_j \frac{\partial U_i}{\partial x_j} = \frac{1}{\rho} \frac{\partial}{\partial x_j} \left(\underbrace{-p \delta_{ij}}_{\text{Pressure}} + \underbrace{2\mu S_{ij}}_{\text{Viscous diffusion}} - \underbrace{\overline{\rho u'_i u'_j}}_{\text{Reynolds stresses}} \right) \quad (3.27)$$

where S_{ij} is the rate of strain tensor,

$$S_{ij} = \frac{1}{2} \left(\frac{\partial U_i}{\partial x_j} + \frac{\partial U_j}{\partial x_i} \right). \quad (3.28)$$

Here, it is possible to verify that the mean flow profile depends on turbulent fluctuations (*Reynolds stresses*), this is what we call the closure modelling problem. The goal of RaNS approach is to find a model for the Reynolds stresses in terms of mean flow and it do it so, by modelling how the energy flow occurs only using mean flow variables and therefore the need to define the *turbulent kinetic energy* (k).

$$k = \frac{1}{2} \overline{u'_i u'_j} \quad (3.29)$$

Whatever the notation of the turbulent kinetic energy equation, this includes terms for the k rate of change, mean flow convection, pressure diffusion, turbulent transport, viscous transport, turbulent production and dissipation [141]. A common formulation is the following:

$$\frac{\partial \rho k}{\partial t} + \nabla \cdot (\rho \mathbf{U} k) = \nabla \cdot \left[\left(\mu + \frac{\mu_t}{\sigma_k} \right) \nabla k \right] + G_k + G_b - \rho \varepsilon + S_k \quad (3.30)$$

In order to finally close the problem, a way to calculate Reynolds stresses ($-\overline{\rho u'_i u'_j}$) must be found. The simpler approach to solve the closure problem, and still the most widely used, are the *eddy viscosity models* [2]. In 1877, Boussinesq [80] proposed a way to model the smallest turbulent scales that generate Reynolds stresses, that will act as viscosity in the Navier-Stokes equations:

$$-\overline{\rho u'_i u'_j} = \mu_t \left(\frac{\partial U_i}{\partial x_j} + \frac{\partial U_j}{\partial x_i} - \frac{2}{3} \frac{\partial U_k}{\partial x_k} \delta_{ij} \right) - \frac{2}{3} \rho k \delta_{ij} \quad (3.31)$$

Equation 3.31 is valid for both the shear and normal stress components. μ_t is the turbulent or eddy viscosity, an artificial parameter that controls the "strength" of the diffusion. There are a large variety of turbulence models based on the eddy viscosity assumption, here only the following models will be approach:

- The standard $k - \varepsilon$ turbulence model;
- The RNG $k - \varepsilon$ turbulence model;
- The realizable $k - \varepsilon$ turbulence model;
- The $\overline{v'^2} - f$ turbulence model.
- The $k - \omega$ turbulence model;
- The $k - \omega$ SST turbulence model;

3.3.1.1 The standard $k - \varepsilon$ turbulence model

The standard $k - \varepsilon$ is one of the most common and widely used turbulence model in CFD. The $k - \varepsilon$ model basis and modifications to the $k - \varepsilon$ of Launder and Spalding [97] model are shown in detail in [142]. In the standard $k - \varepsilon$ model, the dependent variables are the turbulence kinetic energy (k (eq. 3.29)) and the dissipation rate of turbulence energy (ε (eq. 3.32)):

$$\varepsilon = \nu \overline{\frac{\partial u'_i}{\partial x_j} \frac{\partial u'_i}{\partial x_j}} \quad (3.32)$$

The turbulent kinetic energy and the dissipations rate of turbulence energy are determined from the following pair of equations:

$$\frac{\partial}{\partial t}(\rho k) + \frac{\partial}{\partial x_j}(\rho k U_j) = \frac{\partial}{\partial x_j} \left[\left(\mu + \frac{\mu_t}{\sigma_k} \right) \frac{\partial k}{\partial x_j} \right] + G_k + G_b - \rho \varepsilon - Y_M + S_k \quad (3.33)$$

$$\begin{aligned} \frac{\partial}{\partial t}(\rho \varepsilon) + \frac{\partial}{\partial x_j}(\rho \varepsilon U_j) = \frac{\partial}{\partial x_j} \left[\left(\mu + \frac{\mu_t}{\sigma_\varepsilon} \right) \frac{\partial \varepsilon}{\partial x_j} \right] + C_1 \frac{\varepsilon}{k} (G_k + C_3 G_b) \\ - C_2 f_2 \rho \frac{\varepsilon^2}{k} + S_\varepsilon \end{aligned} \quad (3.34)$$

Equation 3.33 together with equation 3.34 enables the turbulent viscosity μ_t to be found:

$$\mu_t = C_\mu f_\mu \rho \frac{k^2}{\varepsilon} \quad (3.35)$$

f_2 and f_μ are damping functions:

$$f_2 = f_\mu = 1 \quad (3.36)$$

According to Launder and Spalding [97], the constants appearing in equations 3.33 and 3.34 take the values given in following table:

Table 3.1 – Default model coefficients for standard $k - \varepsilon$.

C_μ	C_1	C_2	C_3^a	σ_k	σ_ε
0.09	1.44	1.92	-0.33 (usual value)	1.0	1.3

^a Only used when the effect of buoyancy is included. Not to be confused with ($C_{3,RDT}$).

In the standard version of the $k - \varepsilon$ model the transport equations are not integrated up to the walls, instead the logarithmic law of the wall is used to specify the production and dissipation of kinetic energy in cells near to the wall.

The **OpenFOAM** $k - \varepsilon$ model chosen for turbulence is a standard $k - \varepsilon$ turbulence model that can be used for incompressible and compressible flows, its own variant of the model includes a compression term based on rapid distortion theory (RDT), a method based on linear analysis, for calculating "rapidly changing turbulent flows" under the action of different kinds of distortions, such as large-scale velocity gradient, the effects of body forces, etc. [143].

This alternative differs from the standard $k - \varepsilon$ model (eq. 3.33 - 3.34), hence the model equations for the turbulence kinetic energy and the dissipation rate are now, respectively, the following (eq. 3.37 - 3.38):

$$\frac{\partial}{\partial t}(\alpha \rho k) + \nabla \cdot (\alpha \rho \mathbf{U} k) - \nabla^2(\alpha \rho D_k k) = \alpha \rho G - \frac{2}{3} \alpha \rho \nabla \cdot \mathbf{U} k - \alpha \rho \epsilon + S_k + S_{fvOptions} \quad (3.37)$$

$$\begin{aligned} \frac{\partial}{\partial t}(\alpha \rho \varepsilon) + \nabla \cdot (\alpha \rho \mathbf{U} \varepsilon) - \nabla^2(\alpha \rho D_\varepsilon \varepsilon) &= C_1 \alpha \rho G \frac{\varepsilon}{k} - C_2 \alpha \rho \frac{\varepsilon^2}{k} \\ &- \left(\frac{2}{3} C_1 - C_{3,RDT} \right) \alpha \rho \nabla \cdot \mathbf{U} \varepsilon + S_\varepsilon + S_{fvOptions} \end{aligned} \quad (3.38)$$

where $D_k = \nu_t / \sigma_k + \nu$ is the effective diffusivity for k and $D_\varepsilon = \nu_t / \sigma_\varepsilon + \nu$ is the effective diffusivity for ε .

Table 3.2 – OpenFOAM default model coefficients for standard $k - \varepsilon$.

C_μ	C_1	C_2	$C_{3,RDT}$	σ_k	σ_ε
0.09	1.44	1.92	0	1	1.3

In OpenFOAM, as in many CFD codes, it is necessary to stipulate some initialization free-stream boundary conditions values at the inlet, in this model the values of k and ε . Estimating these turbulent variables directly is not always easy and therefore, variables as the turbulence intensity (I) and turbulent length (L_{ref}) are used. Once the appropriate values of this properties have been estimated or measured, k and ε can be computed.

For isotropic turbulence¹, the turbulence kinetic energy can be estimated by (eq. 3.39):

$$k = \frac{3}{2} (I |\mathbf{U}_{ref}|)^2 \quad (3.39)$$

where I is the turbulent intensity, and \mathbf{U}_{ref} a reference velocity. The turbulence dissipation

¹Idealised turbulent state in which the turbulent fluctuations are statistically uniform in all directions.

rate follows as (eq. 3.40):

$$\varepsilon = \frac{C_\mu^{0.75} k^{1.5}}{L_{ref}} \quad (3.40)$$

3.3.1.2 The RNG $k - \varepsilon$ turbulence model

RNG $k - \varepsilon$ was developed by using re-normalization group (RNG methods) by Yakhot and Orszag [99] to re-normalize the Navier-Stokes equations, to account for the effects of smaller scales of motion. Yakhot and Orszag [99] showed how turbulence models could be developed based on a dynamic re-normalization group (RNG methods) with the improvements made by Yakhot et. al [100], scale expansions for the Reynolds stress and production of dissipation terms, lead to a generalised form of the RNG $k - \varepsilon$ turbulence model. The additional parameter is the ratio of the turbulent to mean strain time scale ($\eta \equiv \mathbf{S}k/\varepsilon$). In this model the derivation of the ε equation is revised and the constant in the production of dissipation term is re-evaluated. A detailed development and analysis can be found in [144].

The RNG $k - \varepsilon$ model transport equations are:

$$\frac{\partial}{\partial t}(\rho k) + \frac{\partial}{\partial x_j}(\rho k U_j) = \frac{\partial}{\partial x_j} \left[\left(\mu + \frac{\mu_t}{\sigma_k} \right) \frac{\partial k}{\partial x_j} \right] + G_k - \rho \varepsilon \quad (3.41)$$

$$\frac{\partial}{\partial t}(\rho \varepsilon) + \frac{\partial}{\partial x_j}(\rho \varepsilon U_j) = C_1 \frac{\varepsilon}{k} G_k - C_2 \rho \frac{\varepsilon^2}{k} - \mathfrak{R} + \frac{\partial}{\partial x_j} \left[\left(\mu + \frac{\mu_t}{\sigma_\varepsilon} \right) \frac{\partial \varepsilon}{\partial x_j} \right] \quad (3.42)$$

where

$$\mathfrak{R} = 2\nu_0 S_{ij} \frac{\partial u'_i}{\partial x_j} \frac{\partial u'_j}{\partial x_i} \quad \text{or} \quad \mathfrak{R} = \frac{C_\mu \eta^3 (1 - \eta/\eta_0)}{1 + \beta \eta^3} \frac{\varepsilon^2}{k} \quad (3.43)$$

and

$$\eta = \sqrt{2 S_{ij} S_{ij}} \frac{k}{\varepsilon} \quad (3.44)$$

and the constants C_1 , C_2 , and $\sigma_k = \sigma_\varepsilon$ are calculated explicitly. The contributions of \mathfrak{R} in eq.3.42 is small for weakly strained turbulence and large in the rapid distortion limit when $\eta \rightarrow \infty$.

In the renormalization group procedure the values of all the model coefficients (except β) are derived explicitly.

Table 3.3 – Default model coefficients for RNG $k - \varepsilon$.

C_μ	C_1	C_2	C_3	σ_k	σ_ε	η_0	β
0.0845	1.42	1.68	-0.33	0.71942	0.71942	4.38	0.012

The **OpenFOAM** RNG $k - \varepsilon$ can be applied for both incompressible and compressible flows. The dissipation and turbulent kinetic energy equations are respectively:

$$\begin{aligned} \frac{\partial}{\partial t}(\alpha \rho \varepsilon) + \nabla \cdot (\alpha \rho \mathbf{U} \varepsilon) - \nabla^2(\alpha \rho D_\varepsilon \varepsilon) = \\ (C_1 - \mathfrak{R}) \alpha \rho C_\mu \frac{G}{\nu} - \left(\frac{2}{3} C_1 - C_3 \right) \alpha \rho \nabla \cdot \mathbf{U} \varepsilon - C_2 \alpha \rho \frac{\varepsilon^2}{k} + S_\varepsilon + S_{fvOptions} \end{aligned} \quad (3.45)$$

$$\frac{\partial}{\partial t}(\alpha\rho k) + \nabla \cdot (\alpha\rho \mathbf{U}k) - \nabla^2(\alpha\rho D_k k) = \alpha\rho G - \frac{2}{3}\alpha\rho \nabla \cdot \mathbf{U}k - \alpha\rho\varepsilon + S_k + S_{fvOptions} \quad (3.46)$$

where

$$\mathfrak{R} = \frac{\eta(1 - \eta/\eta_0)}{1 + \beta\eta^3} \quad (3.47)$$

and

$$\eta = \sqrt{2S_{ij}S_{ij}} \frac{k}{\varepsilon} \quad (3.48)$$

The default model coefficient are the same as the model defined by Yakhot and Orszag [99], with the exception of C_3 that now equals zero².

Table 3.4 – OpenFOAM default model coefficients for RNG $k - \varepsilon$.

C_μ	C_1	C_2	C_3	σ_k	σ_ε	η_0	β
0.0845	1.42	1.68	0	0.71942	0.71942	4.38	0.012

The turbulent free-stream boundary conditions variables can be found in the same manner as in the standard $k - \varepsilon$ model.

3.3.1.3 The realizable $k - \varepsilon$ turbulence model

The realizable $k - \varepsilon$ model was first proposed by Shih et. al [98], among the $k - \varepsilon$ models is the most recently developed. This model consists on a new definition of the dissipation rate equation and new eddy viscosity formulation. The dissipation rate equation is based on the dynamic equation of the mean-square vorticity fluctuation ($\overline{\omega_i\omega_i}$), once the equation for $\overline{\omega_i\omega_i}$ is modelled, it is possible to obtain the dissipation rate equation through equation 3.49 at large Reynolds numbers:

$$\varepsilon = \overline{\omega_i\omega_i} \quad (3.49)$$

In this model, the turbulent viscosity is also modelled as:

$$\nu_t = C_\mu \frac{k^2}{\varepsilon} \quad (3.50)$$

However, here the coefficient C_μ is not a constant. Shih et al. [105] used a proposed formulation by Reynolds [145] for the coefficient C_μ , that satisfied the realizability conditions³ [146]:

$$C_\mu = \frac{1}{A_0 + A_s U^{(*)} k/\varepsilon} \quad (3.51)$$

where

$$U^{(*)} = \sqrt{S_{ij}S_{ij} + \tilde{\Omega}_{ij}\tilde{\Omega}_{ij}}, \quad (3.52)$$

$$\tilde{\Omega}_{ij} = \Omega_{ij} - \varepsilon_{ijk}\omega_k \quad (3.53)$$

²This is a common change in the value of C_3 for $k - \varepsilon$ based models, however an explanation couldn't be found in the literature.

³Any non-negative turbulent quantities must remain positive during the evolution of turbulence, and Schwarz's inequality between any turbulent quantities must be satisfied all of the time

and

$$\Omega_{ij} = \bar{\Omega}_{ij} - \varepsilon_{ijk}\omega_k \quad (3.54)$$

where $\bar{\Omega}_{ij}$ is the mean rotation rate viewed in a rotating reference frame with the angular velocity ω_k . The parameter A_S and C_1 are determined by:

$$A_S = \sqrt{6} \cos \phi, \quad \phi = \frac{1}{3} \arccos(\sqrt{6}W) \quad (3.55)$$

$$W = \frac{S_{ij}S_{jk}S_{ki}}{\tilde{S}^3} \quad \tilde{S} = \sqrt{S_{ij}S_{ij}} \quad (3.56)$$

$$C_1 = \max \left\{ 0.43, \frac{\eta}{5 + \eta} \right\} \quad (3.57)$$

where

$$\eta = \frac{\mathbf{S}k}{\varepsilon}, \quad \mathbf{S} = \sqrt{2S_{ij}S_{ij}} \quad (3.58)$$

Table 3.5 – Default model coefficients for realizable $k - \varepsilon$.

C_μ	C_1	C_2	A_0	σ_k	σ_ε
Equation 3.51	Equation 3.57	1.9	4.0	1.0	1.2

The model equations for k and ε are:

$$\frac{\partial}{\partial t}(k\rho) + \frac{\partial}{\partial x_j}(k\rho U_j) = \frac{\partial}{\partial x_j} \left[\left(\mu + \frac{\mu_t}{\sigma_k} \right) \frac{\partial k}{\partial x_j} \right] - G_k - \varepsilon\rho \quad (3.59)$$

$$\frac{\partial}{\partial t}(\varepsilon\rho) + \frac{\partial}{\partial x_j}(\varepsilon U_j\rho) = \frac{\partial}{\partial x_j} \left[\left(\mu + \frac{\mu_t}{\sigma_\varepsilon} \right) \frac{\partial \varepsilon}{\partial x_j} \right] + C_1\rho\mathbf{S}\varepsilon - C_2\frac{\varepsilon^2}{k + \sqrt{\nu\varepsilon}}\rho \quad (3.60)$$

The **OpenFOAM realizable $k - \varepsilon$** model can be applied for both incompressible and compressible flows. The dissipation and turbulent kinetic energy equations are respectively:

$$\frac{\partial}{\partial t}(\alpha\rho\varepsilon) + \nabla \cdot (\alpha\rho\mathbf{U}\varepsilon) - \nabla^2(\alpha\rho D_\varepsilon\varepsilon) = C_1\alpha\rho\mathbf{S}\varepsilon - C_2\frac{\alpha\rho\varepsilon^2}{k + \sqrt{\nu\varepsilon}} + S_\varepsilon + S_{fvOptions} \quad (3.61)$$

$$\frac{\partial}{\partial t}(\alpha\rho k) + \nabla \cdot (\alpha\rho\mathbf{U}k) - \nabla^2(\alpha\rho D_k k) = \alpha\rho G - \frac{2}{3}\alpha\rho\nabla \cdot \mathbf{U}k - \alpha\rho\varepsilon + S_k + S_{fvOptions} \quad (3.62)$$

where

$$C_\mu = \frac{1}{A_0 + A_s U^{(*)} \frac{k}{\varepsilon}} \quad (3.63)$$

and

$$A_s = \sqrt{6} \cos \phi_{A_s} \quad \phi_{A_s} = \frac{1}{3} \arccos(\sqrt{6}W) \quad W = \frac{S_{ij}S_{jk}S_{ki}}{(\sqrt{S_{ij}S_{ij}})^3} \quad (3.64)$$

The turbulent free-stream boundary conditions variables can be found in the same manner as in the standard $k - \varepsilon$ and the RNG $k - \varepsilon$ model. The default model coefficient are the same as the model defined by [98, 105] (table 3.5).

3.3.1.4 The $\overline{v'^2} - f$ turbulence model

The $\overline{v'^2} - f$ model was originally proposed by Durbin [147], latter improved and modified by Lien [148] and Davidson et al. [149], in order to alleviate the "stiffness problem" associated with the original model caused by the boundary conditions at walls and enhance numerical stability. The final formulation of the $\overline{v'^2} - f$ model is the following:

The eddy-viscosity ν_t is given by

$$\nu_t = C_\mu \overline{v'^2} \mathfrak{T}, \quad (3.65)$$

where, \mathfrak{T} is the turbulent time scale defined as

$$\mathfrak{T} = \max \left\{ \frac{k}{\epsilon}, 6 \sqrt{\frac{\nu}{\epsilon}} \right\}, \quad (3.66)$$

and \mathfrak{L} is the turbulent length scale

$$\mathfrak{L} = C_L \max \left\{ \frac{k^{3/2}}{\epsilon}, C_\eta \left(\frac{\nu^3}{\epsilon} \right)^{1/4} \right\}. \quad (3.67)$$

ν_t , \mathfrak{T} and \mathfrak{L} are determined from the standard $k - \epsilon$ equations:

$$\frac{\partial k}{\partial t} + U_j \frac{\partial k}{\partial x_j} = G_k - \epsilon + \frac{\partial}{\partial x_j} \left[\left(\nu + \frac{\nu_t}{\sigma_k} \right) \frac{\partial k}{\partial x_j} \right] \quad (3.68)$$

$$\frac{\partial \epsilon}{\partial t} + U_j \frac{\partial \epsilon}{\partial x_j} = \frac{C_{\epsilon 1} G_k - C_{\epsilon 2} \epsilon}{\mathfrak{T}} + \frac{\partial}{\partial x_j} \left[\left(\nu + \frac{\nu_t}{\sigma_\epsilon} \right) \frac{\partial \epsilon}{\partial x_j} \right] \quad (3.69)$$

The $\overline{v'^2}$ transport equation is

$$\frac{\partial \overline{v'^2}}{\partial t} + U_j \frac{\partial \overline{v'^2}}{\partial x_j} = kf - 6 \overline{v'^2} \frac{\epsilon}{k} + \frac{\partial}{\partial x_j} \left[\left(\nu + \frac{\nu_t}{\sigma_k} \right) \frac{\partial \overline{v'^2}}{\partial x_j} \right], \quad (3.70)$$

where kf represents the redistribution of turbulence energy from the streamwise component, therefore equation 3.70 is called the turbulence stress normal to streamlines equation. Non-locality is represented by solving an elliptic relaxation equation for f

$$\mathfrak{L}^2 \frac{\partial^2 f}{\partial x_j^2} - f = \frac{1}{\mathfrak{T}} \left[(C_1 - 6) \frac{\overline{v'^2}}{k} - \frac{2}{3} (C_1 - 1) \right] - C_2 \frac{G_k}{k}. \quad (3.71)$$

As referred, to overcome some difficulties of the original $\overline{v'^2} - f$ model, some modifications were made by Lien [148] and Davidson et al. [149], these include:

- **Modification I** - reduction of $\overline{v'^2}$ as walls are approached.
 $\overline{v'^2}$ should be smaller than the other normal stresses, which means that $\overline{v'^2} \leq 2k/3$. This relation is not satisfied in the standard $\overline{v'^2} - f$ model. The first modification proposed gives $\overline{v'^2} \leq 2k/3$ everywhere. The source term kf in the $\overline{v'^2}$ -equation (eq. 3.68) is the modelled pressure strain term which is dampened near walls as f goes to zero. In the homogeneous region far away from the wall, the Laplace term

is assumed to be negligible i.e. $\partial^2 f / \partial x_j \partial x_j \rightarrow 0$. Then 3.71 reduces to

$$f_{hom} = -\frac{1}{\mathfrak{L}} \left[(C_1 - 6) \frac{\overline{v'^2}}{k} - \frac{2}{3}(C_1 - 1) \right] + C_2 \frac{G_k}{k} \quad (3.72)$$

In the region far away from the wall, the Laplace term is not negligible, and consequently $\overline{v'^2}$ gets too large so that $\overline{v'^2} > \frac{2}{3}k$. A simple upper bound limit on the source term kf in the $\overline{v'^2}$ -equation was also proposed:

$$\overline{v'^2}_{source} = \min \left\{ kf, \frac{1}{\mathfrak{L}} \left[(C_1 - 6)\overline{v'^2} - \frac{2k}{3}(C_1 - 1) \right] + C_2 G_k \right\} \quad (3.73)$$

This modification ensures that $\overline{v'^2} \leq 2k/3$.

$$\nu_t = \min \left\{ 0.09k^2/\varepsilon, 0.22\overline{v'^2}\mathfrak{L} \right\} \quad (3.74)$$

- **Modification II** - two turbulent viscosities are defined.

In the $\overline{v'^2} - f$ model there are two velocity time scales, $(\overline{v'^2})^{1/2}$ and $k^{1/2}$. The wall-normal stress $\overline{v'^2}$ is dampened near walls as f goes to zero. Thus it is natural to introduce two viscosities, one for wall-normal diffusion ($\nu_{t,\perp}$) and one for diffusion parallel to the wall ($\nu_{t,\parallel}$). Davidson et. al [149] propose to compute them as

$$\nu_{t,\perp} = 0.22\overline{v'^2}\mathfrak{L}, \quad \nu_{t,\parallel} = 0.09k\mathfrak{L} \quad (3.75)$$

Table 3.6 – Default model coefficients for $\overline{v'^2} - f$.

C_μ	σ_k	σ_ε	$C_{\varepsilon 2}$	C_1	C_η	C_L	C_2	$C_{\varepsilon 1}$
0.22	1	1.3	1.9	1.4	70	0.23	0.3	$1.4(1 + 0.05(k/\overline{v'^2})^{1/2})$

OpenFOAM's model equations for the $\overline{v'^2} - f$ turbulence model are the following:

Dissipation rate of turbulence energy equation (ε)

$$\begin{aligned} \frac{\partial}{\partial t}(\alpha\rho\varepsilon) + \nabla \cdot (\alpha\rho\mathbf{U}\varepsilon) - \nabla^2(\alpha\rho D_\varepsilon\varepsilon) = C_{\varepsilon 1}\alpha\rho\frac{G}{\mathfrak{L}} - \left(\frac{2}{3}C_{\varepsilon 1} + C_{\varepsilon 3} \right) \alpha\rho\nabla \cdot \mathbf{U}\varepsilon \\ - C_{\varepsilon 2}\alpha\frac{\rho}{\mathfrak{L}}\varepsilon + S_{fvOptions} \end{aligned} \quad (3.76)$$

Turbulent kinetic energy equation (k)

$$\frac{\partial}{\partial t}(\alpha\rho k) + \nabla \cdot (\alpha\rho\mathbf{U}k) - \nabla^2(\alpha\rho D_k k) = \alpha\rho G - \frac{2}{3}\alpha\rho\nabla \cdot \mathbf{U}k - \alpha\rho\varepsilon + S_{fvOptions} \quad (3.77)$$

Relaxation function equation (f)

$$-\nabla \cdot \mathbf{U} f = -\frac{1}{\mathfrak{L}} f - \frac{1}{\mathfrak{L}k} \left[\frac{1}{\mathfrak{L}} \left[(C_1 - N)\overline{v'^2} - \frac{2}{3}k(C_1 - 1.0) \right] - C_2 G \right] \quad (3.78)$$

Turbulence stress normal to streamlines equation ($\overline{v'^2}$)

$$\begin{aligned} \frac{\partial}{\partial t}(\alpha\rho\overline{v'^2}) + \nabla \cdot (\alpha\rho\mathbf{U}\overline{v'^2}) - \nabla^2 \cdot (\alpha\rho D_k\overline{v'^2}) = -N\alpha\rho\frac{\varepsilon}{k}\overline{v'^2} + S_{fvOptions} \\ + \alpha\rho \min \left\{ kf, C_2G - \frac{1}{\mathfrak{L}} \left[(C_1 - N)\overline{v'^2} - \frac{2}{3}k(C_1 - 1.0) \right] \right\} \end{aligned} \quad (3.79)$$

where

$$\mathfrak{L} = \max \left\{ \frac{k}{\varepsilon}, 6\sqrt{\frac{\nu}{\varepsilon}} \right\} \quad (3.80)$$

$$\mathfrak{L} = C_L \cdot \max \left\{ \frac{k^{3/2}}{\varepsilon}, C_\eta \left(\frac{\nu^3}{\varepsilon} \right)^{1/4} \right\} \quad (3.81)$$

$$\nu_t = \min \left\{ C_{\mu k\varepsilon} \frac{k^2}{\varepsilon}, C_\mu \overline{v'^2} \mathfrak{L} \right\} \quad (3.82)$$

and

$$C_{\varepsilon 1} = 1.4 \left[1 + 0.05 \min \left\{ \sqrt{\frac{k}{\overline{v'^2}}}, 100 \right\} \right] \quad (3.83)$$

Table 3.7 – OpenFOAM default model coefficients for $\overline{v'^2} - f$.

C_μ	$C_{\mu k\varepsilon}$	C_1	C_2	C_L	C_η	$C_{\varepsilon 2}$	$C_{\varepsilon 3}$	σ_ε	σ_k
0.22	0.09	1.4	0.3	0.23	70	1.9	-0.33	1.3	1

The turbulent free-stream boundary conditions k and ε variables can be found in the same manner as in the standard $k - \varepsilon$ model. The inlet value for $\overline{v'^2}$ can also be approximated by

$$\overline{v'^2} = 2/3k \quad (3.84)$$

and the boundary condition for f is *zeroGradient*.

3.3.1.5 The $k - \omega$ turbulence model

The $k - \varepsilon$ models are not very accurate at predicting boundary layers with adverse pressure gradients and low Reynolds numbers applications [150]. The second most widely used two-equation turbulence model is the $k - \omega$ model, originally proposed by Kolmogorov [84] and Spalding [151] that has been developed by Wilcox [86] and others (see [150, 2]).

There are many variants of the $k - \omega$ model, however OpenFOAM (version 6) uses the $k - \omega$ turbulence model version developed by Wilcox in 1998 [87, 152], and therefore the $k - \omega$ model presented here⁴.

$$\frac{\partial(\rho k)}{\partial t} + \frac{\partial(\rho U_j k)}{\partial x_j} = G_k - \beta^* \omega k + \frac{\partial}{\partial x_j} \left[\left(\mu + \sigma_k \frac{\rho k}{\omega} \right) \frac{\partial k}{\partial x_j} \right] \quad (3.85)$$

⁴The most recent version of OpenFOAM (version 9) now includes the Wilcox (2006) [2] formulation.

$$\frac{\partial(\rho\omega)}{\partial t} + \frac{\partial U_j \omega}{\partial x_j} = \frac{\gamma\omega}{k} G_k - \beta\rho\omega^2 + \frac{\partial}{\partial x_j} \left[\left(\mu + \sigma_\omega \frac{\rho k}{\omega} \right) \frac{\partial \omega}{\partial x_j} \right] \quad (3.86)$$

Table 3.8 – Default model coefficients for $k - \omega$.

$C_\mu = \beta^*$	σ_k	σ_ω	β_0	γ
0.09	0.5	0.5	9/125	13/25

The eddy viscosity is:

$$\mu_t = \frac{\rho k}{\omega} \quad \text{or} \quad \nu_t = \frac{k}{\omega} \quad (3.87)$$

The $k - \omega$ model in OpenFOAM is a standard high Reynolds-number $k - \omega$ turbulence model for incompressible and compressible flows. **OpenFOAM's model equations for the $k - \omega$ turbulence model** that implement the Wilcox (1998) formulation [87] are the following:

$$\frac{\partial}{\partial t}(\alpha\rho\omega) + \nabla \cdot (\alpha\rho\mathbf{U}\omega) - \nabla^2(\alpha\rho D_\omega\omega) = \gamma\alpha\rho G \frac{\omega}{k} - \frac{2}{3}\gamma\alpha\rho \nabla \cdot \mathbf{U}\omega - \beta\alpha\rho\omega^2 + S_{fvOptions} \quad (3.88)$$

$$\frac{\partial}{\partial t}(\alpha\rho k) + \nabla \cdot (\alpha\rho\mathbf{U}k) - \nabla^2(\alpha\rho D_k k) = \alpha\rho G - \frac{2}{3}\alpha\rho \nabla \cdot \mathbf{U}k - \beta^*\alpha\rho\omega k + S_{fvOptions} \quad (3.89)$$

Table 3.9 – OpenFOAM default model coefficients for $k - \omega$.

$C_\mu = \beta^*$	$\alpha_k = \sigma_k^{-1}$	$\alpha_\omega = \sigma_\omega^{-1}$	$\beta = \beta_0$	γ
0.09	0.5	0.5	0.072	0.52

The turbulent free-stream boundary conditions k and ε variables can be found in the same manner as in the standard $k - \varepsilon$ model. The inlet value for ω can be found through equation 3.90:

$$\omega = \frac{k^{0.5}}{C_\mu L_{ref}} \quad (3.90)$$

3.3.1.6 The $k - \omega$ SST turbulence Model

The $k - \omega$ SST model was proposed by Menter [89, 153] in attempt to address the problems of the $k - \varepsilon$ and $k - \omega$ models. It has been especially designed for predicting adverse pressure gradient flows where most of the two-equation models are known to fail [93]. The idea behind the SST model, the combination of the best elements of the $k - \varepsilon$ and the $k - \omega$ model. There are three main differences in the $k - \omega$ SST model:

- The introduction of a cross-diffusion term (eq.3.91) in the ω equation, that makes the model insensitive to free-stream flows.

$$2(1 - F_1)\rho\sigma_{\omega 2} \frac{1}{\omega} \frac{\partial k}{\partial x_i} \frac{\partial \omega}{\partial x_i} \quad (3.91)$$

- The use of blending functions to blend the equations together and also blend between the empirical constants. They allow proper calculation of the near-wall and far-field areas. F_1 is equal to zero away from the surface ($k-\varepsilon$ model), and switches over to one inside the boundary layer ($k-\omega$ model).

$$\gamma = \gamma_1 F_1 + \gamma_2 (1 - F_1) \quad (3.92)$$

- The turbulent eddy viscosity now takes into account the transport of the turbulent shear stress (based on Bradshaw's assumption) [153] by including a "viscosity limiter" and is defined as follow:

$$\nu_t = \frac{a_1 k}{\max(a_1 \omega, \mathbf{S} F_2)} \quad (3.93)$$

Where \mathbf{S} is the invariant measure of the strain rate and F_2 is a second blending function defined by:

$$F_2 = \tanh \left\{ \left[\max \left(\frac{2\sqrt{k}}{\beta^* \omega y}, \frac{500\nu}{y^2 \omega} \right) \right]^2 \right\} \quad (3.94)$$

These differences intend to make the $k-\omega$ SST model more precise for a larger variety of flows than the $k-\omega$ model.

In the $k-\omega$ SST the transport equations for k and ω are the following [94]:

$$\frac{\partial(\rho k)}{\partial t} + \frac{\partial(\rho U_i k)}{\partial x_i} = \tilde{G}_k - \beta^* \rho k \omega + \frac{\partial}{\partial x_i} \left[(\mu + \sigma_k \mu_t) \frac{\partial k}{\partial x_i} \right] \quad (3.95)$$

$$\frac{\partial(\rho \omega)}{\partial t} + \frac{\partial(\rho U_i \omega)}{\partial x_i} = \frac{\gamma G_k}{\nu_t} - \beta \rho \omega^2 + \frac{\partial}{\partial x_i} \left[(\mu + \sigma_\omega \mu_t) \frac{\partial \omega}{\partial x_i} \right] + 2(1 - F_1) \rho \sigma_{\omega 2} \frac{1}{\omega} \frac{\partial k}{\partial x_i} \frac{\partial \omega}{\partial x_i} \quad (3.96)$$

Where the blending function F_1 is defined by:

$$F_1 = \tanh \left\{ \left\{ \min \left[\max \left(\frac{\sqrt{k}}{\beta^* \omega y}, \frac{500\nu}{y^2 \omega} \right), \frac{4\rho \sigma_{\omega 2} k}{CD_{k\omega} y^2} \right] \right\}^4 \right\} \quad (3.97)$$

with

$$CD_{k\omega} = \max \left(2\rho \sigma_{\omega 2} \frac{1}{\omega} \frac{\partial k}{\partial x_i} \frac{\partial \omega}{\partial x_i}, 10^{-10} \right) \quad (3.98)$$

and y is the distance to the nearest wall.

A production limiter is used in the SST model to prevent the build-up of turbulence in stagnation regions:

$$\tilde{G}_k = \min(G_k, 10 \cdot \beta^* \rho k \omega) \quad (3.99)$$

Table 3.10 – Default model coefficients for $k - \omega$ SST.

β^*	γ_1	β_1	σ_{k1}	$\sigma_{\omega 1}$	γ_2	β_2	σ_{k2}	$\sigma_{\omega 2}$
0.09	5/9	3/40	0.85	0.5	0.44	0.0828	1	0.856

OpenFOAM's version of the $k - \omega$ SST used is based on the Menter (2001) [154] formulation, with the updated coefficients from Menter (2003) [94] and the addition of the optimal F_3 term for rough walls from Hellsten [93]. In OpenFOAM the implementation of the $k - \omega$ SST is written in terms of $\alpha_{k \text{ or } \omega}$ coefficients instead of σ ($\alpha = 1/\sigma$) so that the blending could be applied to all of the coefficients in a consistent manner.

The turbulent eddy viscosity is defined as follows:

$$\nu_t = \frac{a_1 k}{\max(a_1 \omega, b_1 F_2 \sqrt{S_2})} \quad (3.100)$$

and the turbulent frequency (ω) and turbulent kinetic energy (k) are respectively:

$$\begin{aligned} \frac{\partial}{\partial t}(\alpha \rho \omega) + \nabla \cdot (\alpha \rho \mathbf{U} \omega) - \nabla^2(\alpha \rho D_\omega \omega) = \\ \alpha \rho \gamma \cdot \min \left\{ \frac{G}{\nu}, \frac{c_1}{a_1} \beta^* \omega \cdot \max \left\{ a_1 \omega, b_1 F_2 \sqrt{S_2} \right\} \right\} - \frac{2}{3} \alpha \rho \gamma \nabla \cdot \mathbf{U} \omega \quad (3.101) \\ - \alpha \rho \beta \omega^2 - \frac{\alpha \rho (F_1 - 1) C D_{k\omega}}{\omega} + S_\omega + S_{fvOptions} + Q_{SAS} \end{aligned}$$

$$\begin{aligned} \frac{\partial}{\partial t}(\alpha \rho k) + \nabla \cdot (\alpha \rho \mathbf{U} k) - \nabla^2(\alpha \rho D_k k) = \alpha \rho \tilde{G} - \frac{2}{3} \alpha \rho \nabla \cdot \mathbf{U} - \alpha \rho \beta^* \omega k + S_k \quad (3.102) \\ + S_{fvOptions} \end{aligned}$$

Where the blending functions (F_1 , F_2 and F_3) are defined by:

$$F_1 = \tanh \left\{ \left[\min \left[\max \left(\frac{\sqrt{k}}{\beta^* \omega y}, \frac{500 \mu / \rho}{y^2 \omega} \right), \frac{4 \alpha_{\omega 2} k}{C D_{k\omega} y^2} \right] \right]^4 \right\} \quad (3.103)$$

$$F_2 = \tanh \left\{ \left[\max \left\{ \frac{2 \sqrt{k}}{\beta^* \omega y}, \frac{500 \mu / \rho}{\omega y^2} \right\} \right]^2 \right\} \quad (3.104)$$

$$F_3 = 1 - \tanh \left\{ \left[\frac{150 \mu / \rho}{\omega y^2} \right]^4 \right\} \quad (3.105)$$

where

$$\tilde{G} = \min \{ G, c_1 \beta^* k \omega \} \quad (3.106)$$

and

$$C D_{k\omega} = \max \left(2 \alpha_{\omega 2} \nabla k \nabla \omega \frac{1}{\omega}, 10^{-10} \right) \quad (3.107)$$

All the constants are computed by a blend from the corresponding constants of the $k - \varepsilon$

and the $k - \omega$ model via $\gamma = \gamma_1 F_1 + \gamma_2 (1 - F_1)$.

Table 3.11 – OpenFOAM default model coefficients for $k - \omega$ SST.

α_{k1}	α_{k2}	$\alpha_{\omega1}$	$\alpha_{\omega2}$	β_1	β_2	β^*	γ_1	γ_2	a_1	b_1	c_1
0.85	1.0	0.5	0.856	0.075	0.0828	0.09	5/9	0.44	0.31	1.0	10.0

The turbulent free-stream boundary conditions k , ε and ω variables can be found in the same manner as in the $k - \omega$ model.

3.3.2 Main Conclusions

There are some limitations with RANS models due to the assumptions made. For example the use of an eddy viscosity to close the Navier-Stokes equations or the presumption that the turbulence is effectively isotropic. These limitations include, among others, secondary flows induced by turbulence, rotational flows, transitional flows, unsteady flows and stagnant regions in flows. However, each model tries to provide some sort of solution for one or more of these limitations.

The models here studied can be divided into two groups, the $k - \varepsilon$ models and the $k - \omega$ models. It was possible to verify that, the former are commonly used when the main area of interest is the far from walls region and the latter in near wall regions. This can be justified by the way this models first appeared.

It was found that the use of damping functions that are necessary in the $k - \varepsilon$ become unreliable when applied to a variety of flows that are different from the ones used for their calibration. Therefore, constant updating of the $k - \varepsilon$ model functions and coefficients have been presented, throughout the years, by other versions of the $k - \varepsilon$ model (e.g. realizable or RNG) or by using other functions for the near wall treatment ($\overline{v'^2} - f$, log-law, wall functions, etc.).

The $k - \omega$ model typical application would be external aerodynamics, such as flow over an airfoil, as such the region to be analysed is near the wall. The formulation of these models does not require near wall damping functions. After the $k - \omega$ was first proposed, it was found that the solution values for the $k - \omega$ model were actually sensitive to initial conditions. The $k - \omega$ SST tries to solve the problem of separated flows, which was found, for both $k - \varepsilon$ and $k - \omega$ models, that the wall shear stress was too high and the flow would not separate correctly.

The most important notion to retain is, no universal RANS turbulence model exists yet! Computational results must be compared with experimental data, critically analysed and validated for each model and case.

A proper CFD study case doesn't depend only on the proper choice of turbulence model or boundary conditions, the way the equations are coupled and solved is another important factor, as it will be analysed in the next section.

3.4 Solution Method

Considering the continuity and incompressible Navier-Stokes equations, there are four equations and four unknown variables, hence it shouldn't be a problem to solve this equations numerically. However, there's no equation for pressure (p). The continuity equation is actually a restriction. The convection term in the momentum equation is non-linear and it may not necessarily be available an equation of state (e.g. Ideal gas law) to use to compute the pressure. These are some of the many reasons why algorithms, such as SIMPLE and PISO, are used to solve the equation system.

3.4.1 Finite Volume Methods

OpenFOAM applications are designed for use with unstructured meshes, offering up to 2nd order accuracy, predominantly using collocated variable arrangements [155]. In the 2nd order finite volume methods (FVM), the flow variables (p, T, \mathbf{U}) vary linearly across the cell(control volume (CV)) and these values are stored at the centroid of the control volume [48].

The conservative form of the general scalar transport equation for the property ϕ is:

$$\underbrace{\frac{\partial}{\partial t}(\rho\phi)}_{\text{unsteady}} + \underbrace{\nabla \cdot (\rho\phi\mathbf{u})}_{\text{convection}} - \underbrace{\nabla \cdot (\Gamma\nabla\phi)}_{\text{diffusion}} - \underbrace{S_\phi}_{\text{source}} = 0 \quad (3.108)$$

The Finite Volume Method requires the integration over a control volume such that:

$$\int_V \frac{\partial}{\partial t}(\rho\phi) dV + \int_V \nabla \cdot (\rho\phi\mathbf{u}) dV - \int_V \nabla \cdot (\Gamma\nabla\phi) dV - \int_V S_\phi dV = 0 \quad (3.109)$$

This equation is discretized to produce a system of algebraic equations of the form of a general matrix:

$$\begin{bmatrix} M_{11} & M_{12} & \dots & M_{1n} \\ M_{21} & M_{22} & \dots & M_{2n} \\ \dots & \dots & \ddots & \dots \\ M_{n1} & M_{n2} & \dots & M_{nn} \end{bmatrix} \begin{bmatrix} x_1 \\ x_2 \\ \vdots \\ x_n \end{bmatrix} = \begin{bmatrix} B_1 \\ B_2 \\ \vdots \\ B_n \end{bmatrix} \quad (3.110)$$

Or

$$M\mathbf{x} = \mathbf{B} \quad (3.111)$$

Where, M is the coefficient matrix, \mathbf{x} a vector of unknowns and \mathbf{B} a source vector.

The discretization process employs user selected schemes (fvSchemes file in OpenFOAM) to build M matrix and x vector (e.g. \mathbf{U}). This is where it is defined how to integrated each term in the equation. Integration process of constant source terms, linear source terms, convection terms, and diffusion terms can be found in books such as Perić and Ferziger [48], and Versteeg and Malalasekera [16].

Integration of the convection and diffusion terms, it's very complex, because they contain

the divergence operator. Therefore, the Gauss divergence theorem is used to integrate these terms:

$$\int_V (\nabla \cdot \mathbf{u}) dV = \oint_S (\mathbf{n} \cdot \mathbf{u}) dS \quad (3.112)$$

The above equation is the starting point for the finite volume method [48]. The equation 3.109 can now be written as follows:

$$\frac{\partial}{\partial t} \int_V (\rho\phi) dV + \underbrace{\oint_S (\rho\phi\mathbf{u} \cdot \mathbf{n}) dS}_{\text{convective flux}} - \underbrace{\oint_S (\Gamma\nabla\phi \cdot \mathbf{n}) dS}_{\text{diffusive flux}} - \int_V S_\phi dV = 0 \quad (3.113)$$

Since face centres are now being dealt with, and that is the only information available at the centroid values, face interpolation is needed. The face values appearing in the convective and diffusive fluxes are therefore computed by interpolation from the centroid values of the control volumes at both sides of face f . This is where the face interpolation schemes enter. Some examples are, Upwind, second-order /linear-Upwind, central differencing, Quadratic Upstream Interpolation for Convective Kinematics (QUICK), etc. Many other interpolation schemes exist, and is up to the user to choose which one is the most appropriated [156, 48, 16].

The generic and comparable solution procedure in matrix form, for pressure-velocity coupling algorithms can be described as follows [157] :

1°. Solve the momentum predictor

$$\mathbf{M}\mathbf{U} = -\nabla p \quad (3.114)$$

The coefficient matrix (M) is known. On the right hand side of equation 3.114, an initial guess/previous iteration of the pressure term, and solving for the velocity field (guessed value, since the continuity equation is not yet satisfied), it is possible to calculate a \mathbf{H} matrix. The reason the \mathbf{H} matrix is calculated is because the \mathbf{H} is a source term on the right hand side of the pressure equation.

2°. Extract the \mathbf{A} matrix (the diagonal) from the \mathbf{H} matrix and compute the \mathbf{H} matrix using the computed velocity field.

$$\mathbf{H} = \mathbf{A}\mathbf{U} - \mathbf{M}\mathbf{U} \quad (3.115)$$

the \mathbf{H} matrix depends on the velocity field.

3°. The pressure equation can now be assemble:

$$\nabla \cdot (\mathbf{A}^{-1}\nabla p) = \nabla \cdot (\mathbf{A}^{-1}\mathbf{H}) \quad (3.116)$$

Notice that the \mathbf{H} and the \mathbf{A} appear on the left and right-hand side of the equation. Once solved, the pressure field can be used to correct the velocity field so that it satisfies the continuity equation.

$$\mathbf{U} = \mathbf{A}^{-1}\mathbf{H} - \mathbf{A}^{-1}\nabla p \quad (3.117)$$

the difference in equation 3.117 is that the velocity field is now calculated explicitly. At this point, the velocity field computed will satisfy the continuity equation and this is the velocity field at the end of the algorithm. However, the pressure field is no longer correct even through the velocity field satisfies the continuity equation, and therefore needs updating.

This is where the PISO and SIMPLE algorithms differ, in how to go back and update the pressure equations by updating the \mathbf{H} matrix.

In summation, the SIMPLE and PISO Algorithm procedure are, respectively, the following:

$$\begin{aligned} \mathbf{M}\mathbf{U} &= -\nabla p & (3.118) \\ \mathbf{H} &= \mathbf{A}\mathbf{U} - \mathbf{M}\mathbf{U} & (3.119) \\ \nabla \cdot (\mathbf{A}^{-1}\nabla p) &= \nabla \cdot (\mathbf{A}^{-1}\mathbf{H}) & (3.120) \\ \mathbf{U} &= \mathbf{A}^{-1}\mathbf{H} - \mathbf{A}^{-1}\nabla p & (3.121) \end{aligned}$$

$$\begin{aligned} \mathbf{M}\mathbf{U} &= -\nabla p & (3.122) \\ \mathbf{H} &= \mathbf{A}\mathbf{U} - \mathbf{M}\mathbf{U} & (3.123) \\ \nabla \cdot (\mathbf{A}^{-1}\nabla p) &= \nabla \cdot (\mathbf{A}^{-1}\mathbf{H}) & (3.124) \\ \mathbf{U} &= \mathbf{A}^{-1}\mathbf{H} - \mathbf{A}^{-1}\nabla p & (3.125) \end{aligned}$$

This is the baseline of the PISO and SIMPLE algorithms. However, additional transport equations, such as energy or turbulence exist. This is not a problem, the additional equations are solve within the loops (outer or inner), after the velocity corrector. For example, considering additional transport equations for energy (E) and turbulence scalars (k , ε), and the SIMPLE algorithm the solution procedure yields:

$$\begin{aligned} \mathbf{M}\mathbf{U} &= -\nabla p & (3.126) \\ \mathbf{H} &= \mathbf{A}\mathbf{U} - \mathbf{M}\mathbf{U} & (3.127) \\ \nabla \cdot (\mathbf{A}^{-1}\nabla p) &= \nabla \cdot (\mathbf{A}^{-1}\mathbf{H}) & (3.128) \\ \mathbf{U} &= \mathbf{A}^{-1}\mathbf{H} - \mathbf{A}^{-1}\nabla p & (3.129) \\ \mathbf{M}_E E &= S_E & (3.130) \\ \mathbf{M}_k k &= S_k & (3.131) \\ \mathbf{M}_\varepsilon \varepsilon &= S_\varepsilon & (3.132) \end{aligned}$$

If a mesh is non-orthogonal, when dealing with these algorithms, non-orthogonal correctors must be considered. Due to the non-orthogonality of the mesh, (only) the pressure equation 3.116 requires additional iterations. If two non-orthogonal correctors are used, this means that the pressure equation will be solved three times within each loop (inner

or outer loops) and only then is the velocity field updated.

A more detailed description of the SIMPLE and PISO algorithms is presented in the following subsections. Another algorithm used by OpenFOAM is also presented, the PIMPLE Algorithm.

3.4.2 SIMPLE Algorithm

Semi-Implicit Method for Pressure-Linked Equations (SIMPLE Method) derived by Patankar [8], proceeds in a successive guess-and-correct manner of the Eulerian partial-differential equations for the conservation of mass, momentum, energy and other properties [158]. The SIMPLE procedure is implemented by executing the following sequence of steps⁵

- (1) Guess a pressure field p^* ;
- (2) Solve the momentum equations to obtain u^* , v^* , w^* , variables that describe the velocity field based on a guessed pressure field, p^* ;
- (3) Solve the p' equation;
- (4) Calculate p from $p = p^* + p'$;
- (5) Calculate u , v , w from their starred values using the velocity-correction formulas;
- (6) Solve the discretization equation for other variables (such as temperature or turbulence quantities) if they influence the flow field through fluid properties, source terms, etc.;
- (7) Treat the corrected pressure p as a new guessed pressure p^* , return to step 2, and cycle through this loop until a converged solution is achieved.

3.4.3 PISO Algorithm

The Pressure-Implicit with Splitting of Operators (PISO) method utilises the splitting of operations [159] in the solution of the discretized momentum and pressure equations such that the fields obtained at each time-step are close approximations of the exact solution of the difference equations [160].

Although the method is cast in a time-dependent form, it is also useful for steady-state calculations due to its stability for fairly large time-steps.

Presently, the final form of the operator-split equations, including the modifications deemed necessary by the accuracy and stability consideration presented by Issa [159] are as follows:

- (1) *Predictor Step* for velocity. Here, the previous time steps are used to calculate the coefficients of the momentum equations and solve this implicit equations;
- (2) *Predictor Step* for pressure. Using the predicted velocity, calculate coefficients of pressure equation and solve for the pressure field.

⁵Auxiliar information for the way pressure and velocity are establish can be found in 7.2 - Annex 2.

- (3) *First corrector step* for the velocity. Correct the velocity field, using explicit-type equations.
- (4) Using the corrected velocities, calculate the coefficients of the pressure equation in the corrector step and solve the implicit system of equations to obtain an updated pressure field.
- (5) *Second corrector step* for the velocity. Using the corrected pressure field, re-evaluate the velocity field using explicit-type equations.
- (6) Next time step.

The PISO algorithm was intended for unsteady, incompressible flows. In this case, we have a time derivative. As a result, the diagonal in the M matrix is a lot larger and the system is more diagonally dominant, so under-relaxation is not usually necessary [157], on the condition that the time step is very small. If the time step is very small and the Courant number is less than 1, it is possible to not use relaxation at all, this is how the PISO algorithm was originally proposed.

The PISO algorithm is deliberately a lot shorter than the SIMPLE algorithm, usually it is performed one momentum predictor and then two inner loops of the pressure corrector which is often fairly sufficient to converge the time steps after having proceeded over the initial transient in the simulation.

3.4.4 PIMPLE Algorithm

OpenFOAM has an algorithm that combines the PISO and SIMPLE algorithms, the PIMPLE Algorithm [155]. This algorithm merges the outer-correction tools of SIMPLE with the inner-corrector loop of PISO in order to achieve a more robust and generalizable pressure-velocity coupling [161].

The PIMPLE Algorithm allows the use of larger time steps and then converge the time steps partially, doing less iterations within a time step, when compared with the PISO algorithm, allowing to extend the Courant Number greater than 1.

3.5 Convergence Criteria

In every simulation it is necessary to have a criteria to determine the solution convergence. The decision of stopping an iterative method, on each level(inner or outer iterations), is important from both accuracy and efficiency standpoint.

In an iterative method the criteria is to estimate the iteration error in order to decide when to stop iterating. Some methods of estimating the iteration error and criteria for stopping iterations can be found in [48].

One of the most common convergence criteria is based in controlling the dimensionless error of the algebraic equations (values between 0.001 and 0.00001 are usual) [162]. Because the Navier-Stokes equations are non-linear, the iterations may become unstable

in some cases while remaining stable in others. The instability often can be overcome by adjustment in numerical parameters, such as relaxation factors or time-steps. Grid quality also can have an influence on convergence (smoothness and/or resolution).

The unknown error can be measured by residuals that monitor the rate that the iterations progress toward convergence.

In the unsteady problems, the solution itself is changing in time. The time-dependent solution is converged when the periodic limit cycle is approached. In cases like this, it is very difficult to judge convergence by an examination of residuals without also examining a solution variable.

Convergence is perhaps the most important propriety of a numerical solution, although not the only. Other properties such as consistency, stability, conservation, boundedness and realizability must be taken into account [48, 162].

3.6 Meshing

A mesh divides a geometry into a finite number of (non-overlapping) sub-domains which are used by the CFD solver to construct a mesh of cells, control volumes or elements. In these sub-domains, the variables are to be calculated at discrete locations (cell centres, face centres, etc.), some examples can be observed in figure 3.2.

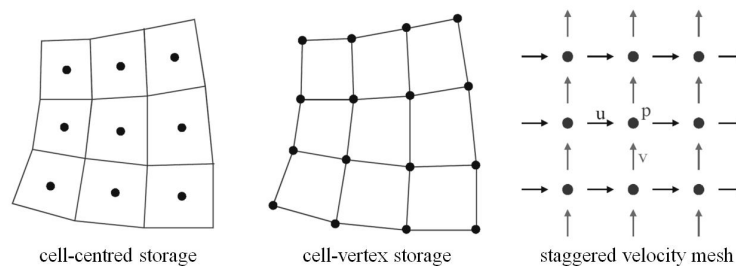


Figure 3.2 – Some possible locations to store information at cells [3].

Mesh design and generation has huge literature, that is not possible to be dealt within the length of this dissertation. Therefore only a few aspects will be referred. For more information on mesh type and generation see [163, 5, 164].

3.6.1 Type of Numerical Grid

There are several types numerical grid or mesh, however they can be typically grouped into three large families: structured, unstructured and hybrid [5]. The classification of meshes is based on the way in which the grid cells and their nodes are locally organized. Typically the mesh is considered to be structured when the grid nodes and the form of the grid cells are defined by a general rule [164]. An unstructured mesh is one in which

vertices may have arbitrarily varying local neighbourhoods, in other words the connection of the neighbouring grid nodes varies from point to point [4]. If a number of small structured meshes are combined into a general unstructured pattern is formed a hybrid mesh. Figure 3.3 shows an example of the referred types of meshes applied to a simple geometry.

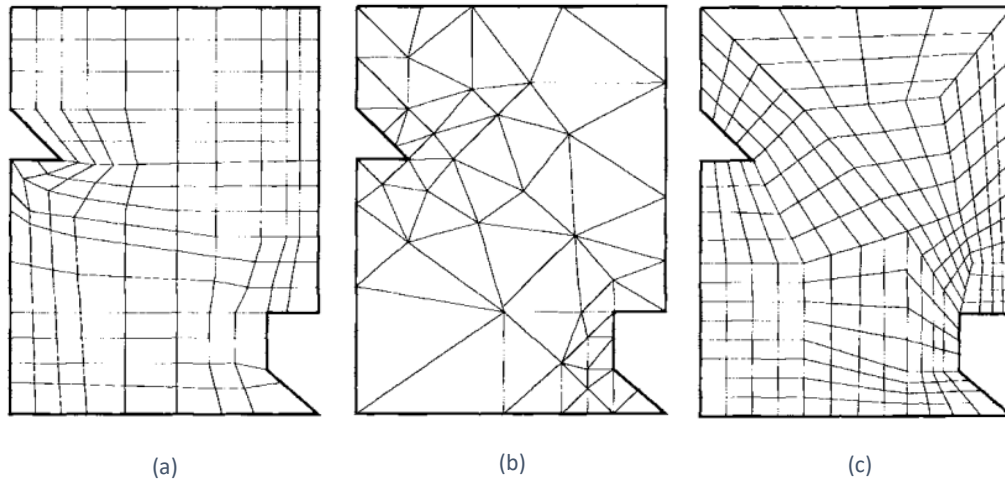


Figure 3.3 – Types of meshes: (a) structured, (b) unstructured, and (c) hybrid [4].

Unstructured meshes are particularly useful when dealing with very complex geometries. They are more flexible in the way they lay out the elements or volumes in space and offer more convenient mesh adaptivity (refinement) [162].

3.6.2 Mesh Quality and Generation

The creation of a high quality mesh is a crucial factor to ensure simulation accuracy. It is possible to evaluate mesh quality through some mesh proprieties, such as [5, 48]

- Smoothness - The difference between cell sizes should not be very abrupt.
- Aspect ratio - The ratio between the longest and the shortest length.
- Skewness - The distance between the intersection of the line connecting two cell centres with their common face and the centre of that face.
- Non-orthogonality - angle between a line connecting two cell centers in a mesh and a face normal vector [165].

OpenFOAM provides a tool to verify mesh quality, the *checkMesh* utility, that and evaluates this quality parameters and others [155]. The meshes created in this dissertation were produced by making use of an open-source software, *FreeCAD* and combining it with two OpenFOAM mesh generation utilities, *blockMesh* and *snappyHexMesh*.

All the subjects covered so far contribute to the understanding of CFD simulation basics and provide sufficient information to decide which steps to take when preparing a CFD

case. It also raises awareness of some key moments in a CFD simulation, where special attention must be given, to prevent possible errors or uncertainties. Figure 3.4 summarizes this process.

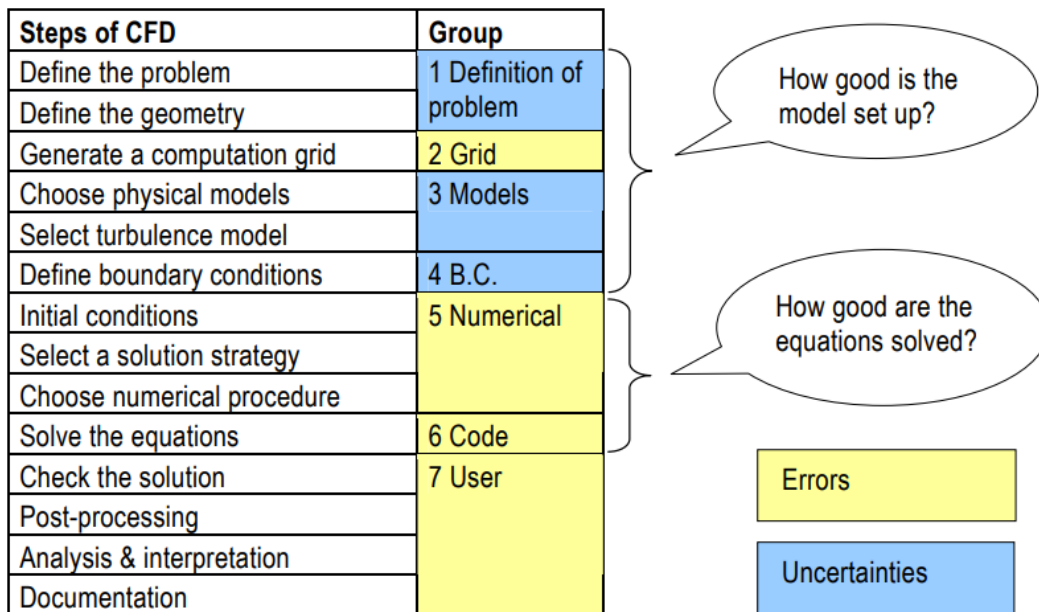


Figure 3.4 – Steps of CFD simulation and groups of error sources [5].

TURBULENCE MODELS VALIDATION

4.1 TURBULENT CHANNEL FLOW

4.2 2D ISOTHERMAL TEST CASE IN ANNEX 20

4.3 2D NON-ISOTHERMAL TEST CASE IN ANNEX 20

4.4 3D ISOTHERMAL TEST CASE IN ANNEX 20

4 TURBULENCE MODELS VALIDATION

4.1 Turbulent Channel Flow

4.1.1 Introduction

In order to define a proper entrance for the supplied air, it is of interest to study the behaviour of a flow across a channel. The motive for its choice is that the channel simple geometry allows to evaluate a few important aspects more quickly (less computational power is required), such as:

- the develop of a flow through the channel (velocity, pressure, etc.);
- boundary layer behaviour;
- hydrodynamic entrance region. The time-averaged velocity profile remains unchanged when the flow is fully developed [130].

4.1.2 Test Case Specifications

The case geometry is shown in figure 4.1.



Figure 4.1 – Channel Geometry

The test case here considered has the following dimensions:

$$H = 0.168 \text{ m} \quad \text{and} \quad L = 10 \text{ m}, \quad (4.1)$$

which denotes the height and length of the channel, respectively.

For this test case, the air is supplied on the left and exhausted through the right of the channel. The inlet velocity is

$$U_0 = 0.455 \text{ m/s}. \quad (4.2)$$

and the kinematic viscosity $\nu \approx 15.3 \times 10^{-6} \text{ m}^2/\text{s}$ (at an assumed uniform temperature of 20°C). This leads to Reynolds number calculated with equation 7.12:

$$Re = \frac{U_0 H}{\nu} = \frac{0.455 \times 0.168}{15.3 \times 10^{-6}} \approx 5000 \quad (4.3)$$

A turbulent intensity of 4% is used. Nielsen [20] proposed that the turbulent length scale could be estimated from:

$$L_{ref} = \frac{H}{10} \quad (4.4)$$

Therefore, the free-stream values for the channel case, can be estimated from equations (3.39-3.40):

$$k_0 = \frac{3}{2} (0.04 \times 0.455)^2 \approx 4.9686 \times 10^{-4} \text{ m}^2/\text{s}^2 \quad (4.5)$$

and

$$\varepsilon_0 = \frac{0.09^{0.75} \cdot (4.9686 \times 10^{-4})^{1.5}}{0.0168} \approx 1.0832 \times 10^{-4} \text{ m}^2/\text{s}^3 \quad (4.6)$$

4.1.3 Pre-Processing

4.1.3.1 Boundary Conditions

A 2D channel flow is considered and therefore an *empty* boundary condition for the front and back walls of the channel is used. This means that the equations in the z -direction are not solved. The boundary conditions for the inlet, outlet and walls are presented in tables 4.1, 4.2 and 4.3, respectively.

Table 4.1 – Inlet boundary conditions.

Field	Boundary Condition
\mathbf{U}	(0.455 0 0)
p	<i>zeroGradient</i>
k	4.9686×10^{-4}
ε	1.0832×10^{-4}

Table 4.2 – Outlet boundary conditions.

Field	Boundary Condition
\mathbf{U}	<i>zeroGradient</i>
p	0
k	<i>zeroGradient</i>
ε	<i>zeroGradient</i>

Table 4.3 – Walls boundary conditions.

Field	Boundary Condition
\mathbf{U}	<i>noSlip</i>
p	<i>zeroGradient</i>
k	<i>kqRWallFunction</i>
ε	<i>epsilonWallFunction</i>

The *zeroGradient* condition extrapolates the variables value to the boundary from the nearest cell value, which means that the gradient is equal to zero in the direction perpendicular to the boundary. *Fixed value* of the variables provide a constant value at the boundary. *noSlip*, fixes the velocity to zero at the walls. *kqRWallFunction* wall function simply implements a *zeroGradient* condition for turbulent kinetic energy, square-root of turbulent kinetic energy or Reynolds stress tensor. *epsilonWallFunction* wall function [166] provides a wall constraint on the turbulent kinetic energy dissipation rate, i.e. ε , and the turbulent kinetic energy production contribution. It inherits the traits of the *fixedValue* boundary condition, that is used as initial "guess".

4.1.3.2 Turbulence Model and Numerics

For this study, the standard $k - \varepsilon$ was used to model the fluctuating quantities. From the previous chapter (chapter 3), it was found that the standard $k - \varepsilon$ model has been proven to be a robust, simple model with good convergence and insensitive to inlet values and therefore a reasonable model to implement for a initial simulation test.

A first order divergence scheme, Gauss Upwind, was used to discretize the convection and diffusion terms, due to its stability and simplicity [5].

For the pressure-velocity coupling, the SIMPLE algorithm was used for steady-state simulations. For transient simulations, the PIMPLE algorithm is used for the coupling. In the transient simulations, the time step Δt is based on the maximum CFL (Courant, Friedrichs, and Lewy condition) number of 0.5.

First order *Euler* implicit time scheme was implemented, in order to determine time derivative of variables in transient simulations (unsteady component of the transport equation (eq. 3.108)). For steady state simulations, the temporal derivative's contributions were set to zero ($\frac{\partial}{\partial t}(\phi) = 0$).

Under-relaxation factors were implemented. Smooth solvers based on the Gauss-Seidel method were used to converge the solution to the required tolerance.

The simulations were carried out on a desktop computer (Intel quad core i3-9100f, 3.60 GHz processor) with OpenFOAM 6.

4.1.3.3 Mesh Independence

The mesh used in a CFD study has a significant impact on the results accuracy of the simulation, since the code will use cells (control volumes) to perform the calculations. Ideally, higher the number of cells, higher the independence of the results on the mesh. However, it is not always attainable to indefinitely increase the mesh density (higher computational time and cost). Nevertheless, it is not necessary to create meshes that are too dense, because after a certain number of cells the differences in the results are negligible and the results are nearly mesh independent. Therefore, results accuracy can be achieved with a much lesser mesh density (coarse meshes) and thus lower computational time and cost.

Figure 7.4 in Annex 7.4 shows the meshes studied for the channel case. The ratio between the maximum value of the velocity profile (U) and the initial velocity (U_0) across the channel (fig. 4.2), in particular at the exhaust opening ($L = 10\text{m}$)(fig. 4.3), was evaluated in order to assess mesh independence.

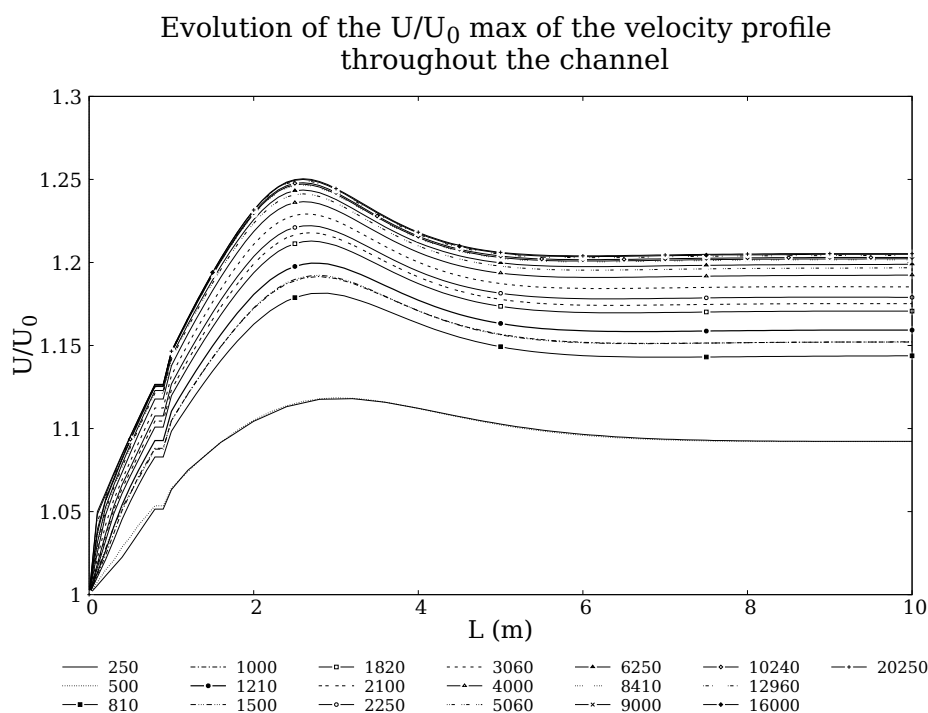


Figure 4.2 – Evolution of the U/U_0 at the point of the velocity gradient maximum, for velocity profile throughout the channel for different meshes.

It is possible to observe that for the last four meshes (cells number = 10240, 12960, 16000 and 20250) the results are similar, this means that increasing the number of cells of the mesh will not bring any advantages, the results will be very much the same and the computational cost will increase.

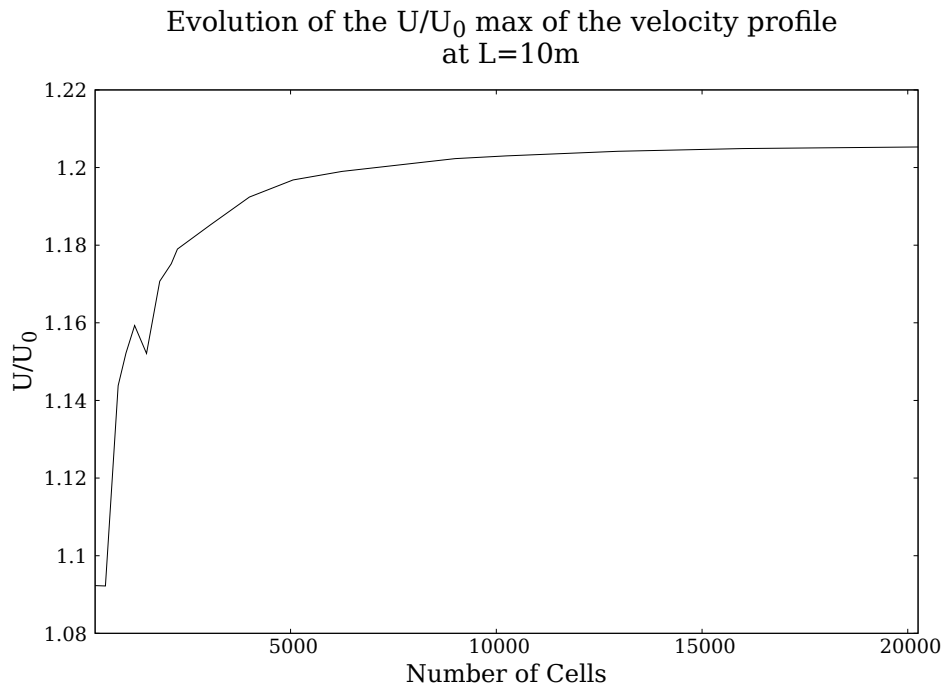


Figure 4.3 – Evaluation of the ratio (U/U_0 max) independence on the mesh at $L = 10\text{m}$.

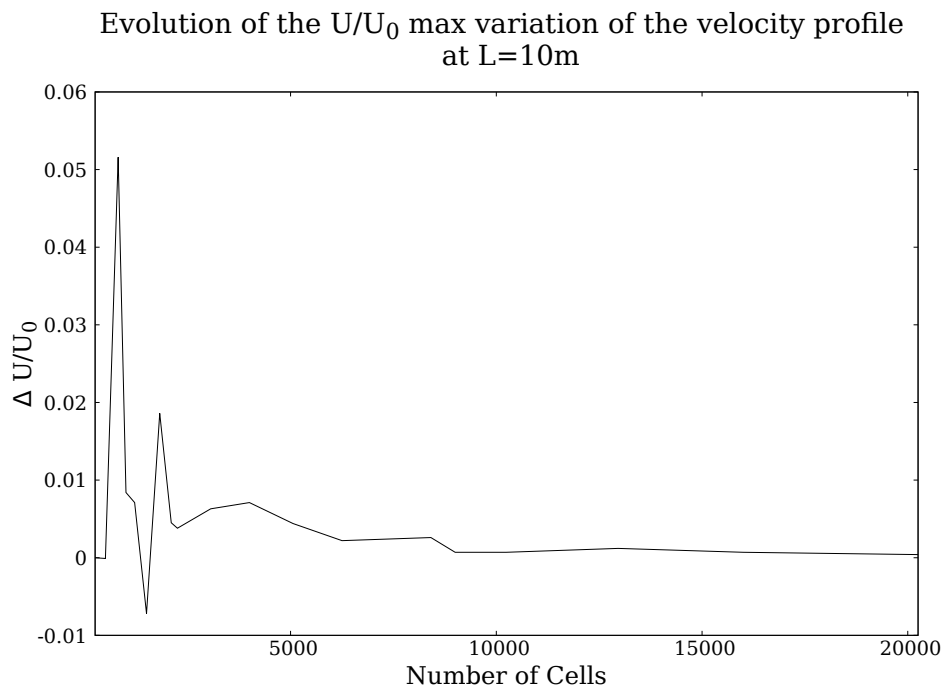


Figure 4.4 – Evolution of the variation of the ratio (U/U_0 max) of the velocity profile at $L = 10\text{m}$ with increasing number of cells.

From figures 4.3 and 4.4 it is possible to clearly confirm that from approximately 10000 cells, (nearly) grid independence is achieved and the final mesh can be chosen.

To complement this mesh study, quality parameters must be analysed. This was achieved by using an OpenFOAM utility, *checkMesh* (fig. 4.5), and parameters such as mesh aspect ratio, skewness and non-orthogonality, among others, were evaluated.


```

Checking geometry...
Overall domain bounding box (0 0 0) (10 0.168 0.005)
Mesh has 2 geometric (non-empty/wedge) directions (1 1 0)
Mesh has 2 solution (non-empty) directions (1 1 0)
All edges aligned with or perpendicular to non-empty directions.
Boundary openness (6.06827e-20 1.62395e-17 -6.12513e-15) OK.
Max cell openness = 1.59097e-16 OK.
Max aspect ratio = 34.3809 OK.
Minimum face area = 6.46354e-06. Maximum face area = 0.000222222. Face area magnitudes OK.
Min volume = 2.87268e-07. Max volume = 5.74537e-07. Total volume = 0.0084. Cell volumes OK.
Mesh non-orthogonality Max: 0 average: 0
Non-orthogonality check OK.
Face pyramids OK.
Max skewness = 3.19739e-13 OK.
Coupled point location match (average 0) OK.

Mesh OK.

End

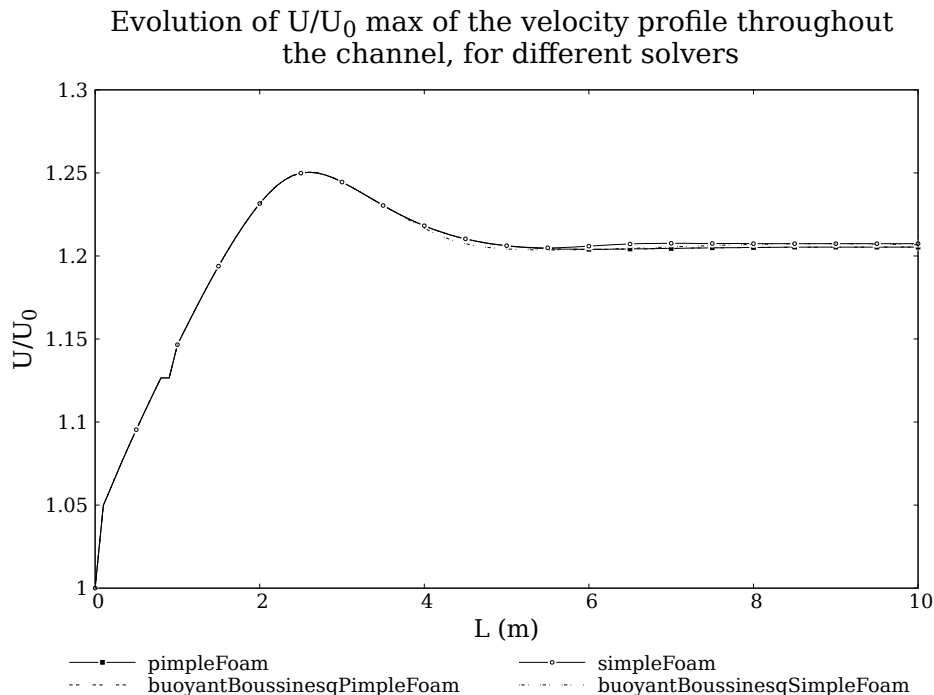
```

Figure 4.5 – *checkMesh* excerpt.

4.1.3.4 Solver

Four different solvers from the OpenFOAM library were chosen:

- *simpleFoam*, steady-state solver for incompressible, turbulent flows;
- *pimpleFoam*, transient solver for incompressible, turbulent flow;
- *buoyantBoussinesqPimpleFoam*, transient solver for buoyant, turbulent flow of incompressible fluids. Uses the Boussinesq approximation;
- *buoyantBoussinesqSimpleFoam*, steady-state solver for buoyant, turbulent flow of incompressible fluids.

Figure 4.6 – Solver comparison for the evolution of U/U_0 max of the velocity profile.

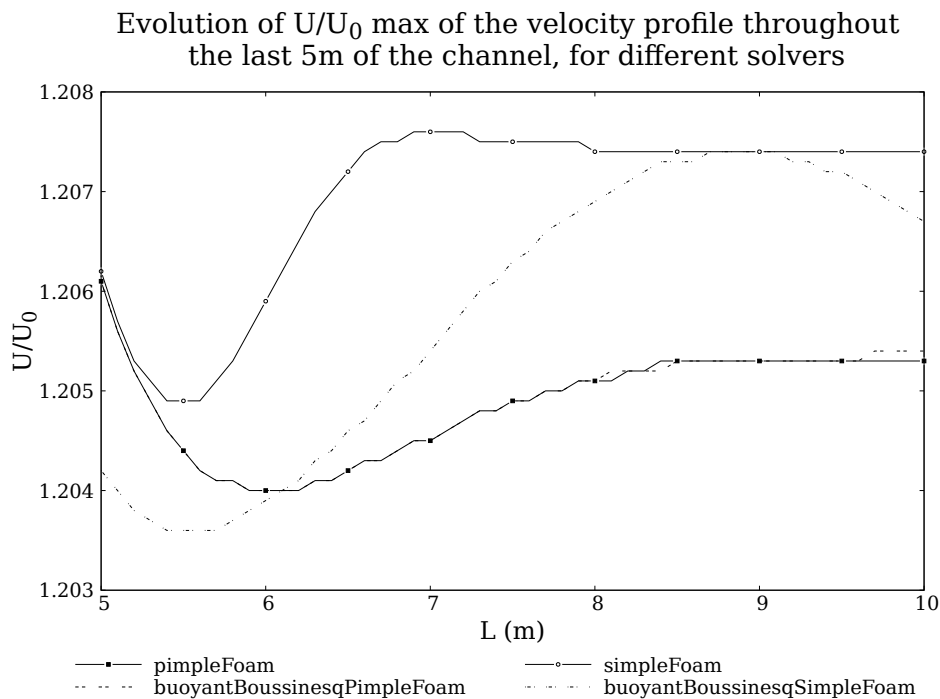


Figure 4.7 – Solver comparison for the evolution of U/U_0 max of the velocity profile in the last 5m of the channel.

From the simulations performed with the four solvers it was possible to verify, that all show good performance with negligible differences (figure 4.6).

The transient solver for incompressible flow (*pimpleFoam*) and transient thermal solver at constant temperature (*buoyantBoussinesqPimpleFoam*) (treating the case as isothermal) show almost identical behaviour. However, the steady-state solvers differ among them (*simpleFoam* and *buoyantBoussinesqSimpleFoam*). Nevertheless, these differences are not significant (variations in the order of 10^{-3}) and is up to the user to choose which solver to use.

4.1.3.5 Parallel Running

Simulations are often run in parallel to reduce computational time. The method of parallel computing used by OpenFOAM is known as domain decomposition. In it, the geometry and associated fields are divided and allocated into separate processors to be solved [155]. The 2D channel case was decomposed up to four processors by using a simple geometric decomposition by direction (2 2 1), respectively in the x , y and z -directions.



Figure 4.8 – Cells distribution by processors.

The number of cells distributed per each processors should not be much different, to ensure stability and quality¹ while reconstructing the case. An example of cells distribution per processor is shown in table 4.4, for the mesh with a total cell number of 20250.

Table 4.4 – Number of cells distributed by processors.

Processor	Number of cells
0	5149
1	4976
2	4976
3	5149

4.1.4 Post-Processing

4.1.4.1 Residuals and Convergence

Convergence is a major issue in CFD. CFD problems are usually non-linear (Navier-Stokes equations, turbulence, etc.) and the solution methods use iterative processes as already approached in chapter 3. Therefore simulations can become unstable in some cases while remaining stable in others [43]. The solution should converge to some value, to evaluate this, usually what is done is the analysis of the residuals. They are quantities that measure the unknown error. Figure 4.9 shows the residuals of the channel case simulation, convergence is achieved (the residuals show a periodic development).

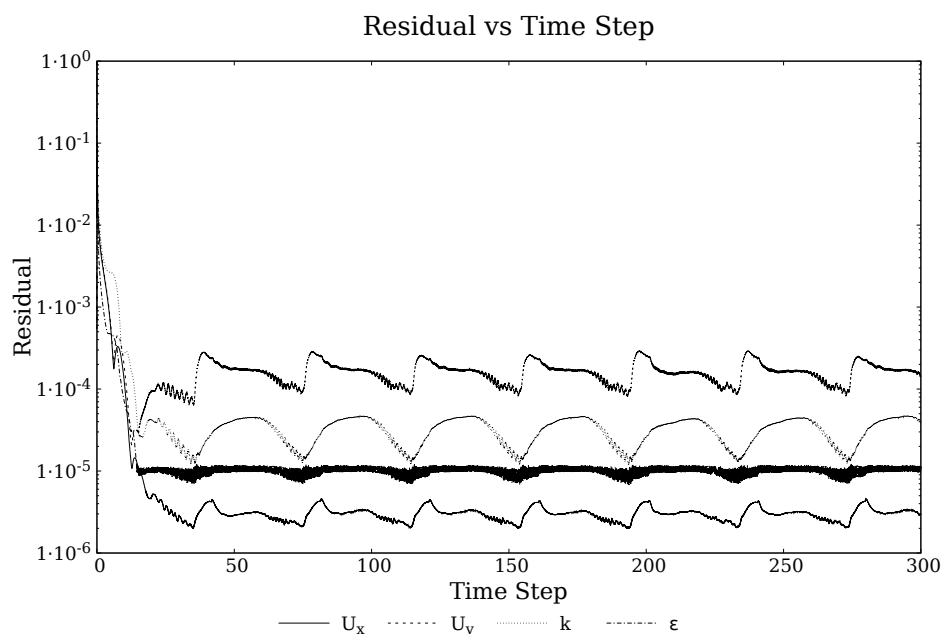


Figure 4.9 – Residuals for the main variables at study (U , k and ϵ).

¹It is advised to use an equal number of cells on each core, in order to have an uniform simulation time (a core doesn't have to "wait" for the other to finish). This also leads to low number of faces between cores, reducing the interdependency between cores.

4.1.4.2 Results

The development of the velocity and turbulent kinetic energy can be observed in figures 4.10 and 4.11. The velocity profile across the channel is presented in figure 4.14, here it is possible to verify that from $L = 6$ m onwards the velocity profile is fully developed.

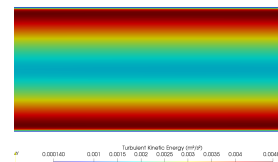
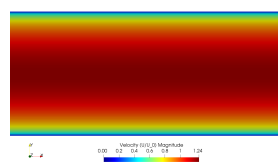
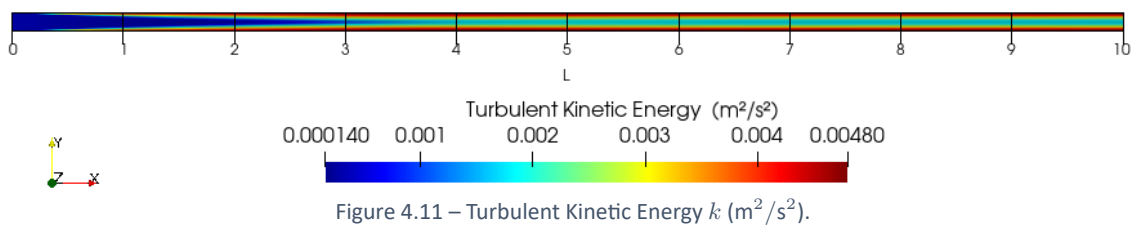
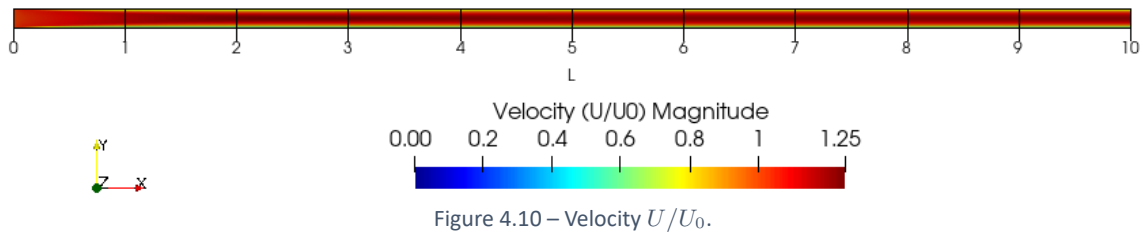
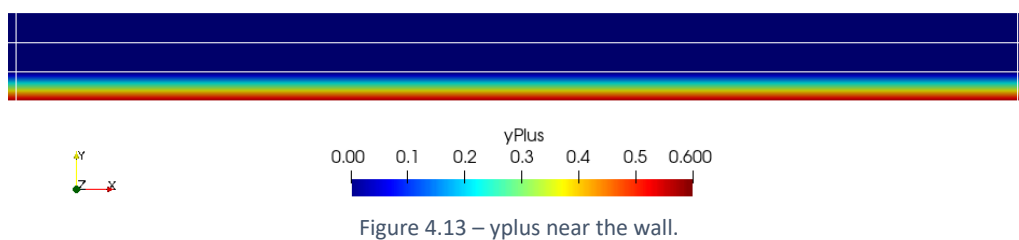


Figure 4.12 – Section of the channel in the fully developed region of the flow at $L = 7m$.



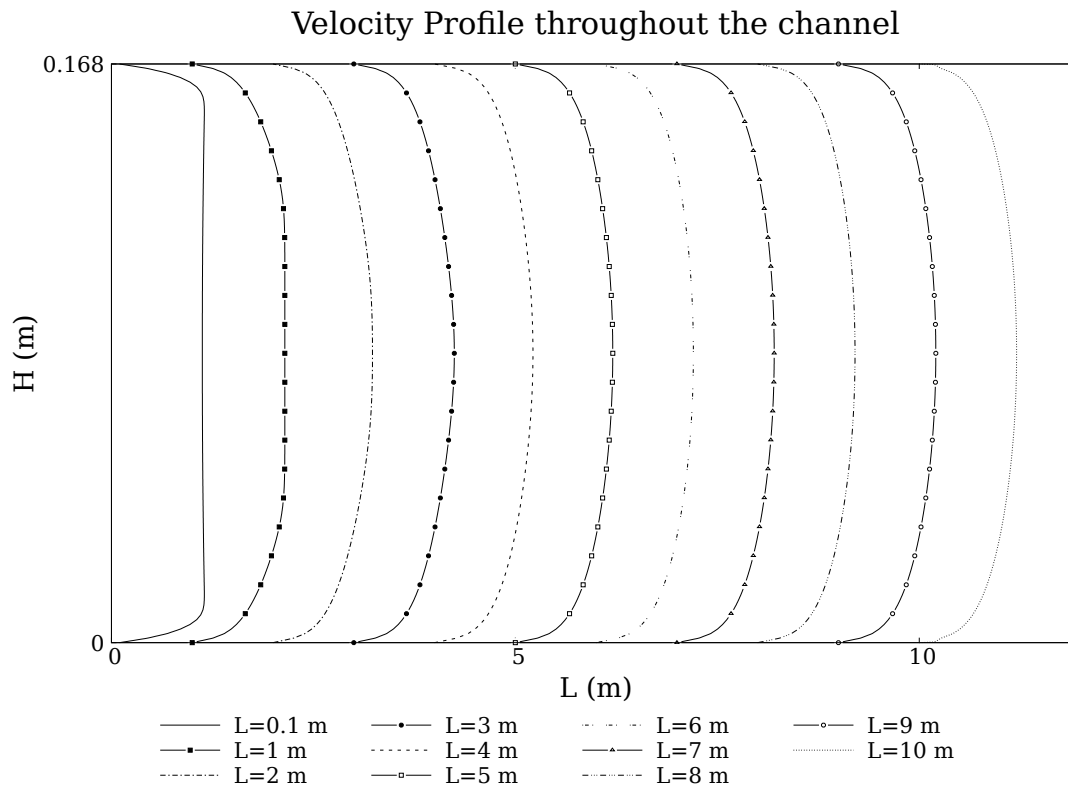


Figure 4.14 – Velocity Profile across the channel.

4.1.4.3 Conclusions

This case allowed to assess some important aspects of CFD simulations:

- 1°. Inadequate **boundary conditions** can lead to physically incorrect results. An initial simulation performed with an ill boundary condition for the pressure at the supply opening ($\neq zeroGradient$), lead to unrealistic velocity profiles;
- 2°. Boundary layer behaviour and proper **wall treatment** are extremely important. Turbulence was integrated near the wall region through the use of wall functions, in order to satisfy the physics in the near wall region.
- 3°. **Mesh independence** studies should always be performed.
- 4°. **Mesh quality** is a factor of weight, since, for example, high aspect ratio or skewness can lead to unrealistic results or lack of convergence.
- 5°. The flow across the channel developed as expected. For a certain number of cells and a length of about 6 m the flow is fully developed.

4.2 2D Isothermal Test Case in Annex 20

4.2.1 Introduction

In this section a 2D benchmark from the IEA Annex 20 [6] was studied in order to evaluate some important modelling aspects of CFD that influence the prediction accuracy in room ventilation. Boundary and numerical conditions, mesh design and turbulence models are some some topics addressed. Six turbulence models, standard $k-\varepsilon$, RNG $k-\varepsilon$, realizable $k-\varepsilon$, $\overline{v'^2}-f$, $k-\omega$ and $k-\omega$ SST, were tested. The results were compared with the Laser Doppler Anemometry (LDA) experiment measurements, performed by Nielsen [20].

4.2.2 Test Case Specifications

The case geometry, from the Annex 20 room benchmark is shown in figure 4.15.



Figure 4.15 – Sketch of the two-dimensional test case [6].

The room has the following dimensions:

$$H = 3 \text{ m}, \quad L = 9 \text{ m}, \quad h = 0.168 \text{ m} \quad \text{and} \quad t = 0.48 \text{ m}, \quad (4.7)$$

here, H and L are respectively the room high and length, h is the supply high and t is the exhaust opening high. The air is supplied on the left at the top and exhausted through the right at the bottom of the room.

A Reynolds number of $Re = 5000$ was used, according to the IEA Annex 20. For isothermal flow at a constant temperature of 20°C the kinematic viscosity is $\nu \approx 15.3 \times 10^{-6} \text{ m}^2/\text{s}$. In this benchmark a turbulence intensity of 4% is used and the turbulent length scale is estimated as proposed by Nielsen [20]:

$$L_{ref} = \frac{h}{10} \quad (4.8)$$

The mean supplied velocity and free-stream values for the IEA Annex 20 room are in table 4.5:

Table 4.5 – Mean supplied velocity U_0 and free-stream values for the IEA Annex 20 room.

Variable	Equation	Free-stream value	Units
U_0	7.12	0.455	m/s
k	3.39	4.9686×10^{-4}	m^2/s^2
ε	3.40	1.0832×10^{-4}	m^2/s^3
ω	3.90	14.7423	s^{-1}
$\overline{v'^2}$	3.84	3.3124×10^{-4}	m^2/s^2

4.2.3 Pre-Processing

4.2.3.1 Boundary Conditions

As seen in chapter 3 and the previous case, a poor definition of boundary conditions can give rise to a lack of convergence of the simulation, or even convergence to a wrong solution. The boundary conditions for the velocity and turbulence parameters of Annex 20 2D isothermal room, for the different turbulence models variables, for the inlet, outlet and walls are presented in tables 4.6, 4.7 and 4.8, respectively.

Table 4.6 – Room supply opening boundary conditions.

Field	Boundary Condition
\mathbf{U}	(0.455 0 0)
p	<i>zeroGradient</i>
ν_t	<i>calculated</i>
k	4.9686×10^{-4}
ε	1.0832×10^{-4}
ω	14.7423
$\overline{v'^2}$	3.3124×10^{-4}
f	<i>zeroGradient</i>

Table 4.7 – Room exhaust opening boundary conditions.

Field	Boundary Condition
\mathbf{U}	<i>zeroGradient</i>
p	0
ν_t	<i>calculated</i>
k	<i>zeroGradient</i>
ε	<i>zeroGradient</i>
ω	<i>zeroGradient</i>
$\overline{v'^2}$	<i>zeroGradient</i>
f	<i>zeroGradient</i>

Table 4.8 – Room walls boundary conditions.

Field	Boundary Condition
\mathbf{U}	<i>noSlip</i>
p	<i>zeroGradient</i>
ν_t	<i>nutkWallFunction</i>
k	<i>kqRWallFunction</i>
ε	<i>epsilonWallFunction</i>
ω	<i>omegaWallFunction</i>
$\overline{v'^2}$	<i>v2WallFunction</i>
f	<i>fWallFunction</i>

nutkWallFunction boundary condition provides a wall constraint on the turbulent viscosity (ν_t), based on the turbulent kinetic energy (k)². The *omegaWallFunction* boundary condition provides a wall constraint on the specific dissipation rate and the turbulent kinetic energy production contribution. *v2WallFunction* provides a turbulence stress normal to streamlines wall function condition. *fWallFunction* gives a turbulence damping wall function condition. Both the *v2WallFunction* and the *fWallFunction* operate in two ways, based on the computed laminar-to-turbulent then switch-over y^+ value derived from the Von Kármán constant and a model coefficient.

4.2.3.2 Mesh Independence

Thirteen meshes were tested in order to evaluate the the results dependency on the mesh density. For a quicker analysis three meshes were selected to demonstrate the mesh independence evolution and they are highlighted in table 4.9 as *coarse*, *medium* and *fine*. The extended comparison with all the meshes can be found in annex 7.5.

Table 4.9 – Number of cells of the meshes studied for the room geometry.

Mesh	Number of cells		Mesh	Number of cells	
0	1 850	-	7	90 650	-
1	7 400	-	8	110 400	-
2	16 650	<i>coarse</i>	9	118 400	-
3	29 600	-	10	149 850	-
4	46 250	-	11	154 800	-
5	66 600	-	12	159 750	<i>fine</i>
6	76 200	<i>medium</i>			

²The model equations used to calculate ν_t can be found in OpenFOAM code guide [155].

In order to evaluate mesh independence, for this case three different vertical sections were chosen (fig. 4.16) and the variable compared was the velocity (U/U_0):

- $x = 0H$, supply opening;
- $x = H$ and $x = 2H$.

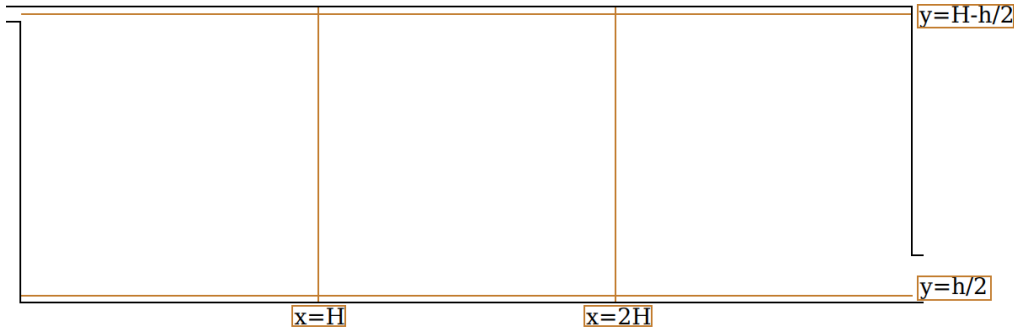


Figure 4.16 – Test case measurement lines.

Figure 4.17 shows the evolution of the mean velocity (U) over the supplied average velocity (U_0) at the point of maximum ratio for all the meshes studied. From about 70 000 cells the results become similar. The same behaviour for other measurement sections, the results of which can be found in annex 7.5 figures 7.8 - 7.11.

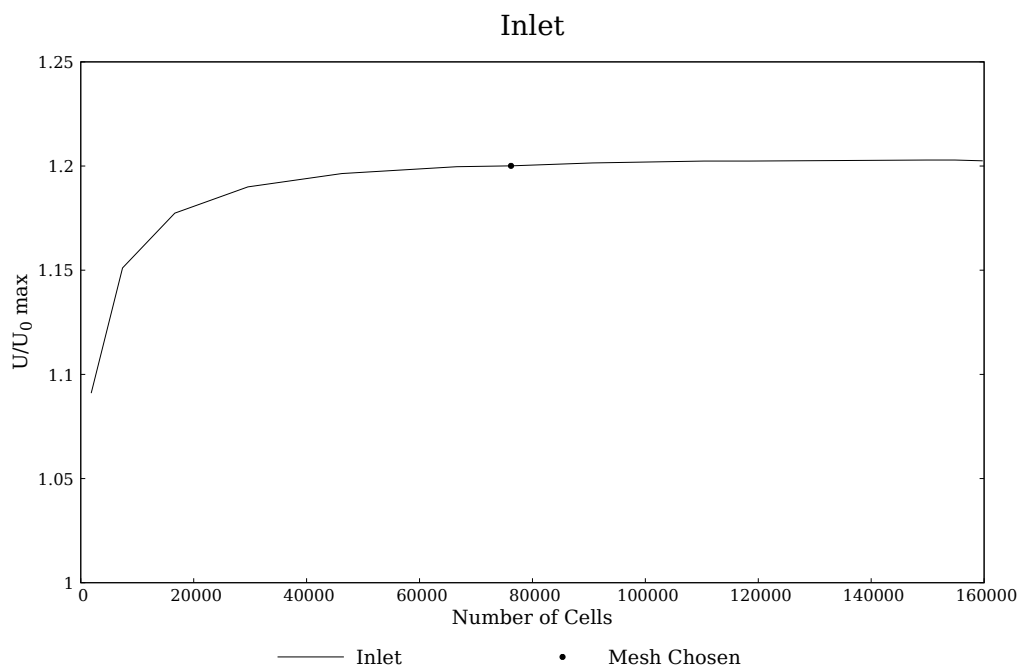


Figure 4.17 – Evolution of U/U_0 maximum at the supply opening (inlet).

The velocity (U/U_0) vertical profiles for the measurements sections chosen to analyse the mesh independence, $x = H$ and $x = 2H$, including a detail analysis near top and bottom walls, for all meshes, are shown in annex 7.5, figures 7.12 - 7.15.

By comparing, as referred, the coarse, medium and fine meshes, it is possible to see that the medium mesh presents essentially the same results accuracy as a more refined mesh (fine). Therefore it is possible to conclude that mesh independence is achieved.

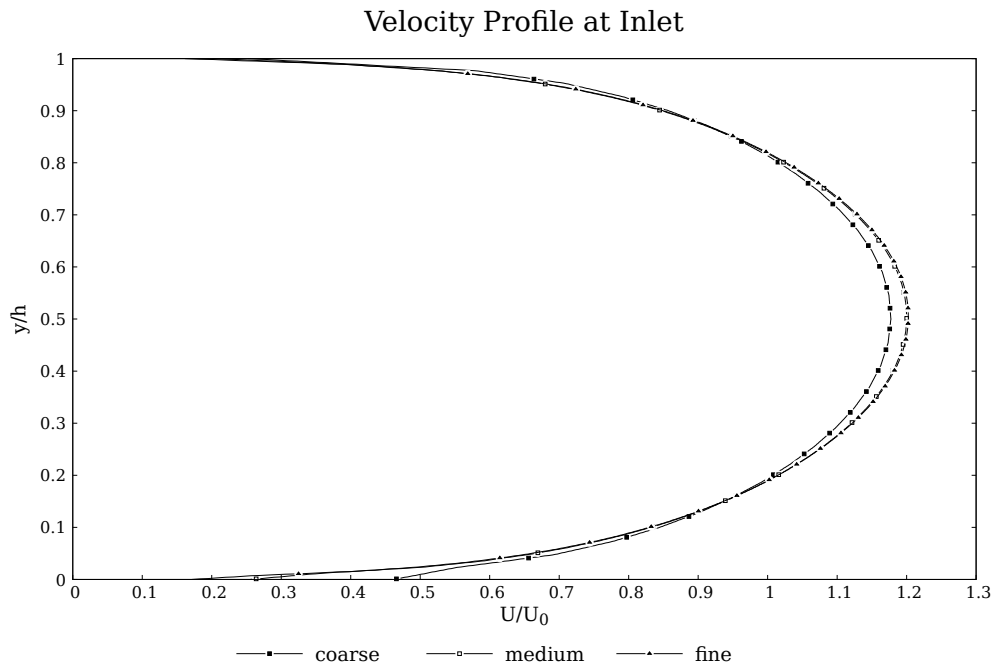


Figure 4.18 – Velocity profile (U/U_0) at the room inlet for meshes 2(coarse), 6(medium) and 12(fine).

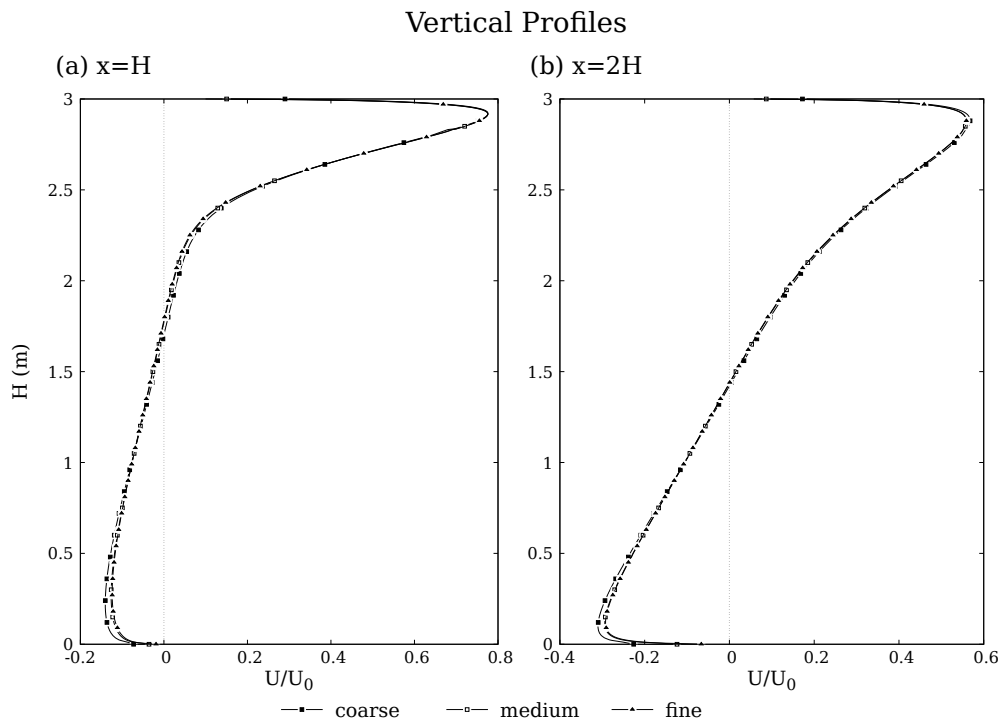


Figure 4.19 – Velocity profile (U/U_0) at $x=H$ and $x=2H$ for meshes 2(coarse), 6(medium) and 12(fine).

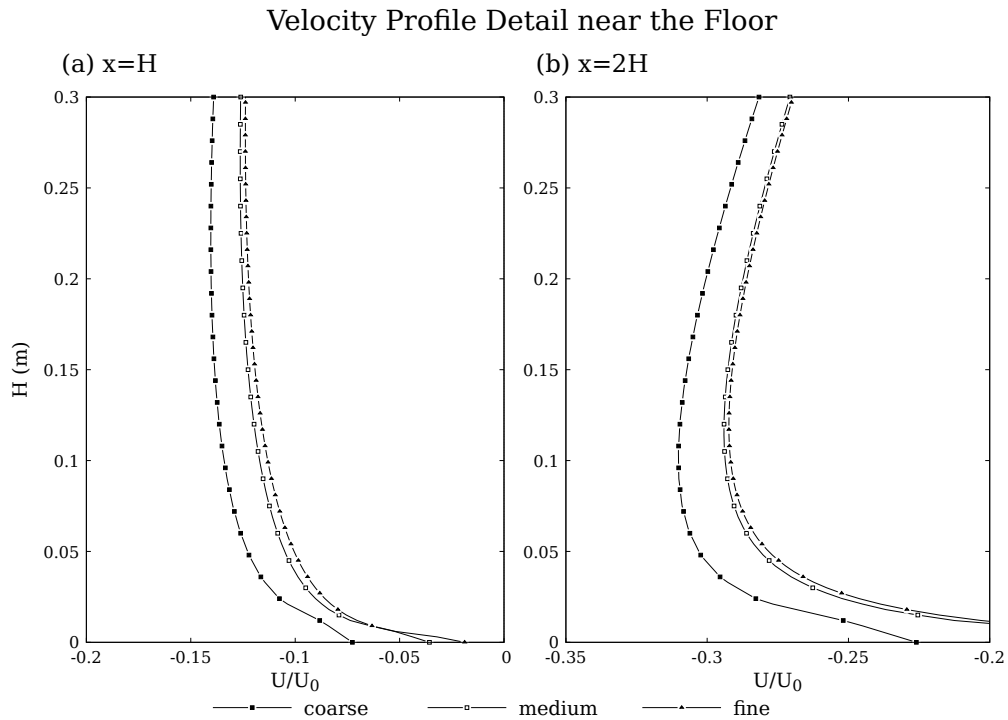


Figure 4.21 – Velocity profile (U/U_0) at $x=H$ and $x=2H$, near the room floor.

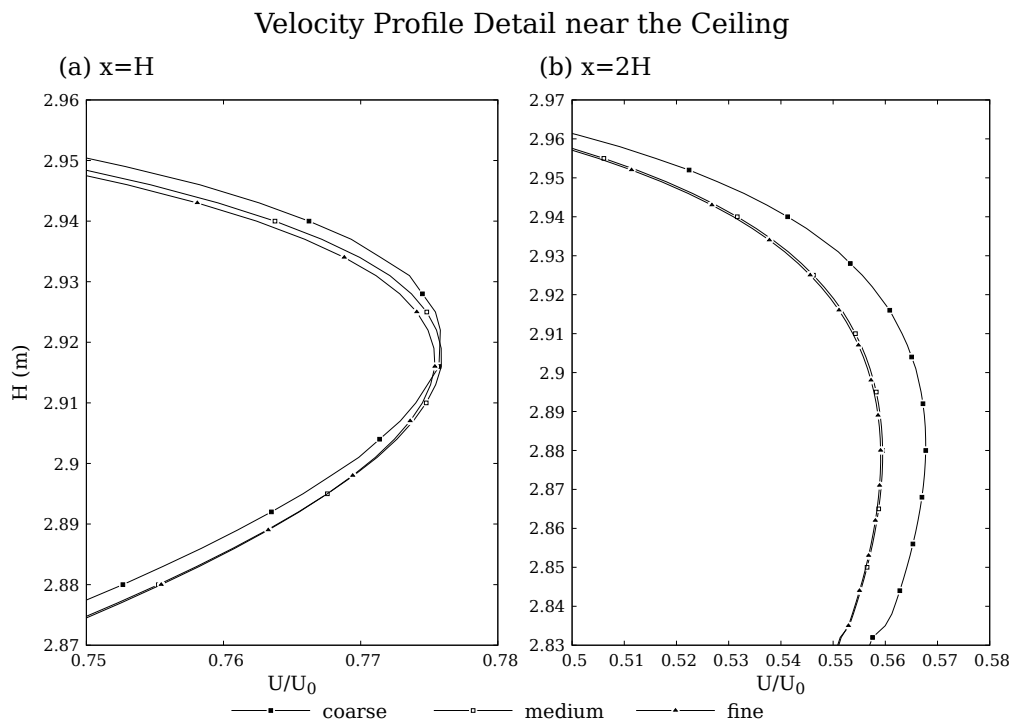


Figure 4.20 – Velocity profile (U/U_0) at $x=H$ and $x=2H$, near the room ceiling.

Similar to the previous case, quality parameters were evaluated. Figure 4.22 shows the maximum aspect ratio and skewness for the various room meshes studied. The analysis of the quality parameters reinforce the choice of mesh 6 (medium), as they present very low aspect ratio and skewness values. This contributes to simulation stability.

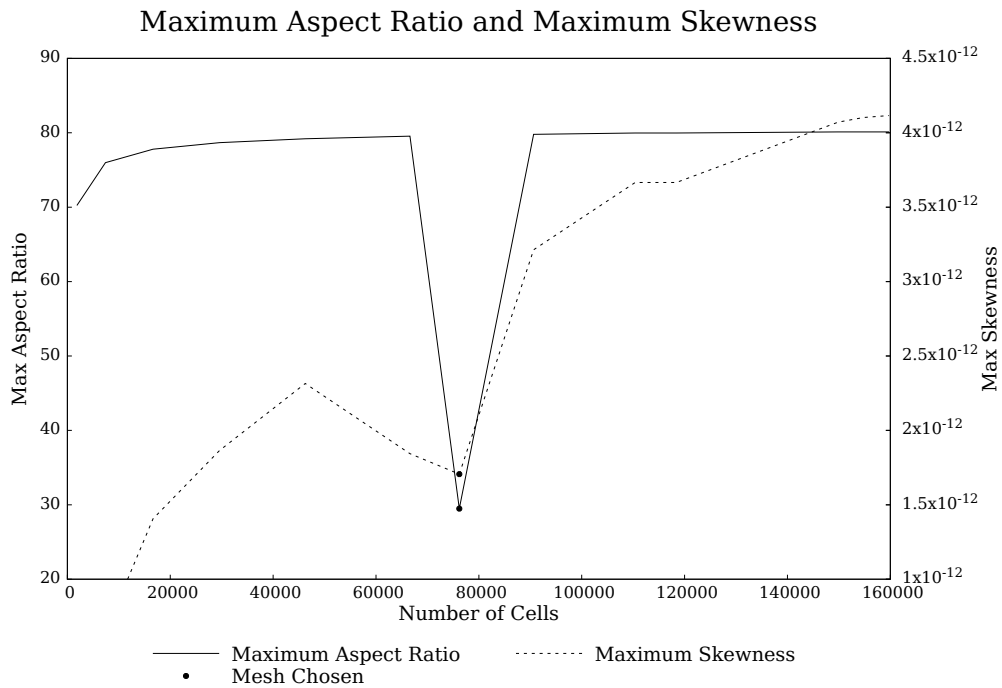


Figure 4.22 – Aspect ratio and maximum skewness.

4.2.3.3 Parallel Running

The Annex 20 2D isothermal test case was decomposed up to six processors by using a simple geometric decomposition by direction (3 2 1), respectively in the x , y and z –directions.

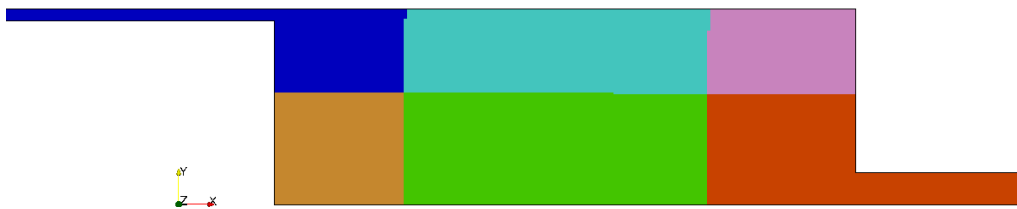


Figure 4.23 – Cell distribution by processor for the Annex 20 room.

For the mesh chosen, the cells are distributed by processors as shown in table 4.10.

Table 4.10 – Cell distribution by processor for the Annex 20 room.

Processor	Number of cells
0	7645
1	13037
2	17418
3	17755
4	12363
5	7982

4.2.3.4 Solver

Two different solvers from the OpenFOAM library were compared, *simpleFoam* and *pimpleFoam*.

Solver results are compared with LDA experiment measurements performed by Nielsen [20]. The measurements sections are the ones already shown in figure 4.16. The results compared are the dimensionless velocity field (U/U_0) and the root mean square (RMS) velocity ($\sqrt{u'^2}/U_0$). The latter can be related, according to Nielsen [20], to the turbulent kinetic energy by:

$$\sqrt{k} \approx 1.1 \sqrt{u'^2}, \quad (4.9)$$

since the flow can be regarded as a flow with wall jet.

Figures 4.24 - 4.26 show the results for the different solvers at the measurement sections of figure 4.16.

The transient solver, *pimpleFoam* shows the better agreement with the experimental results, specially at $x = H$ bottom region. At this location, the steady-state solver, *simpleFoam*, under-predicts the velocity.

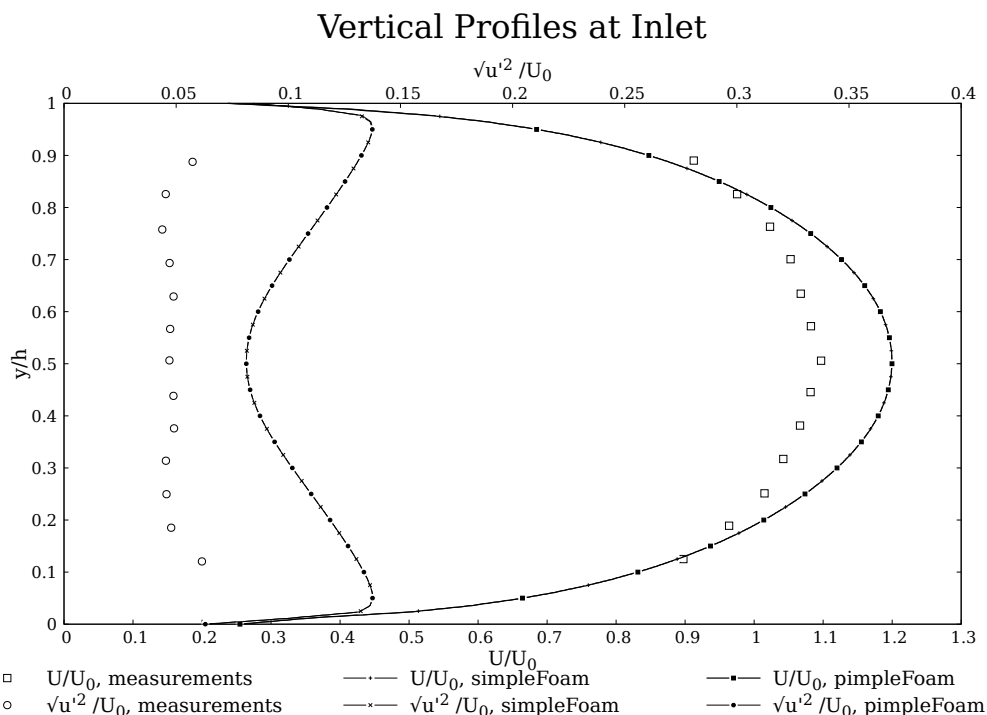


Figure 4.24 – Transient and steady-state solver comparison, for the velocity field magnitude (U/U_0) and RMS velocity ($\sqrt{u'^2}/U_0$) at the inlet.

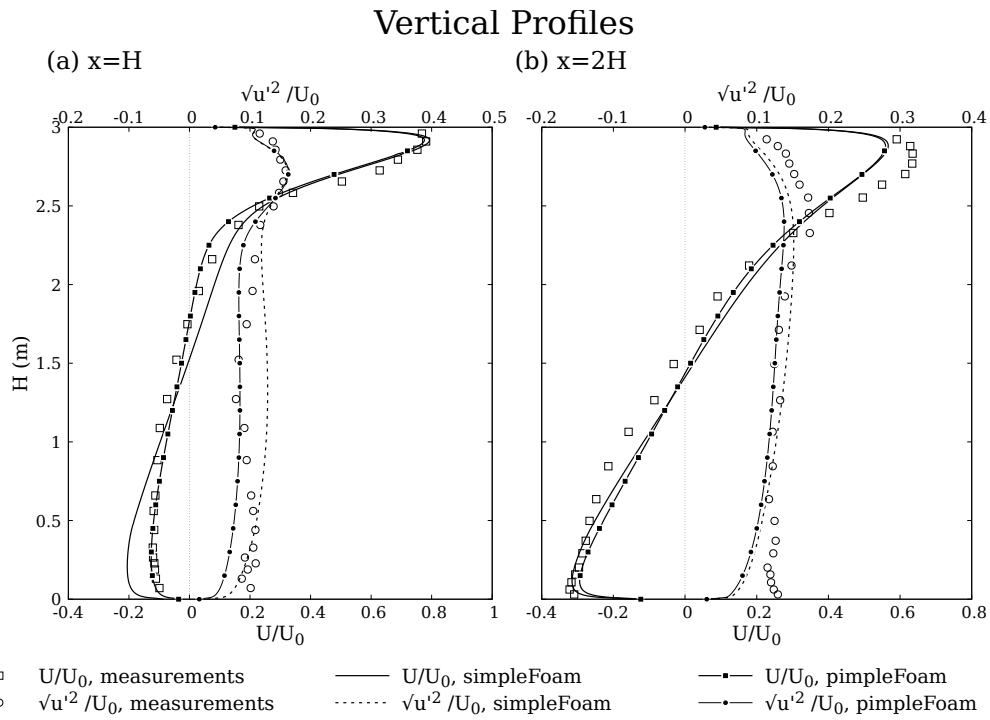


Figure 4.25 – Transient and steady-state solver comparison, for the velocity field magnitude (U/U_0) and RMS velocity ($\sqrt{u'^2}/U_0$) at $x = H$ and $x = 2H$.

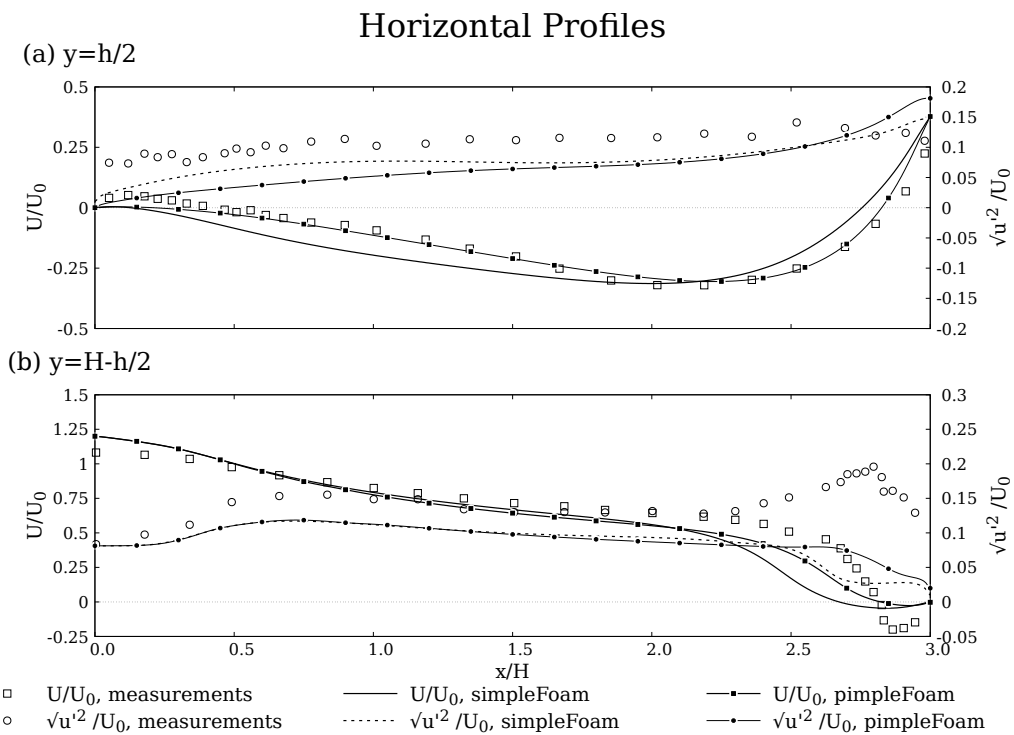


Figure 4.26 – Transient and steady-state solver comparison, for the velocity field magnitude (U/U_0) and RMS velocity ($\sqrt{u'^2}/U_0$) at $y = H - h/2$ and $y = h/2$.

4.2.3.5 Turbulence Models and Numerics

Nielsen et al. [5] states that second order schemes are always recommended if available, and if convergence can be achieved. For the discretization of the convection and diffusion terms, it was chosen a second order divergence scheme, Gauss linearUpwind and bounded Gauss linearUpwind to yield more accurate results than first order schemes, however for some models convergence was no longer possible and it was necessary to go back to first order schemes.

First order *Euler* implicit time scheme was used, in order to determine time derivative of variables in transient simulations. For steady state simulations, the temporal derivative's contributions were set to zero ($\frac{\partial}{\partial t}(\phi) = 0$).

For the pressure-velocity coupling, the SIMPLE algorithm was used for steady-state simulations. For transient simulations, the PIMPLE algorithm is used for the coupling. For transient simulations, an adjustable time step function was used with a maximum Courant number up to 5 (studies were performed with $Co = 0.5, 1, 2$ and 5). Under-relaxation factors were implemented. Smooth solvers based on the Gauss-Seidel method were used to converge the solution to the required tolerance.

The six RaNS turbulence models, previously mentioned, were tested and its validated for room ventilation.

The simulations were carried out on a desktop computer (Intel quad core i3-9100f, 3.60 GHz processor) with OpenFOAM 6.

Figure 4.27 shows the streamlines of the velocity magnitude for the various turbulence models tested.

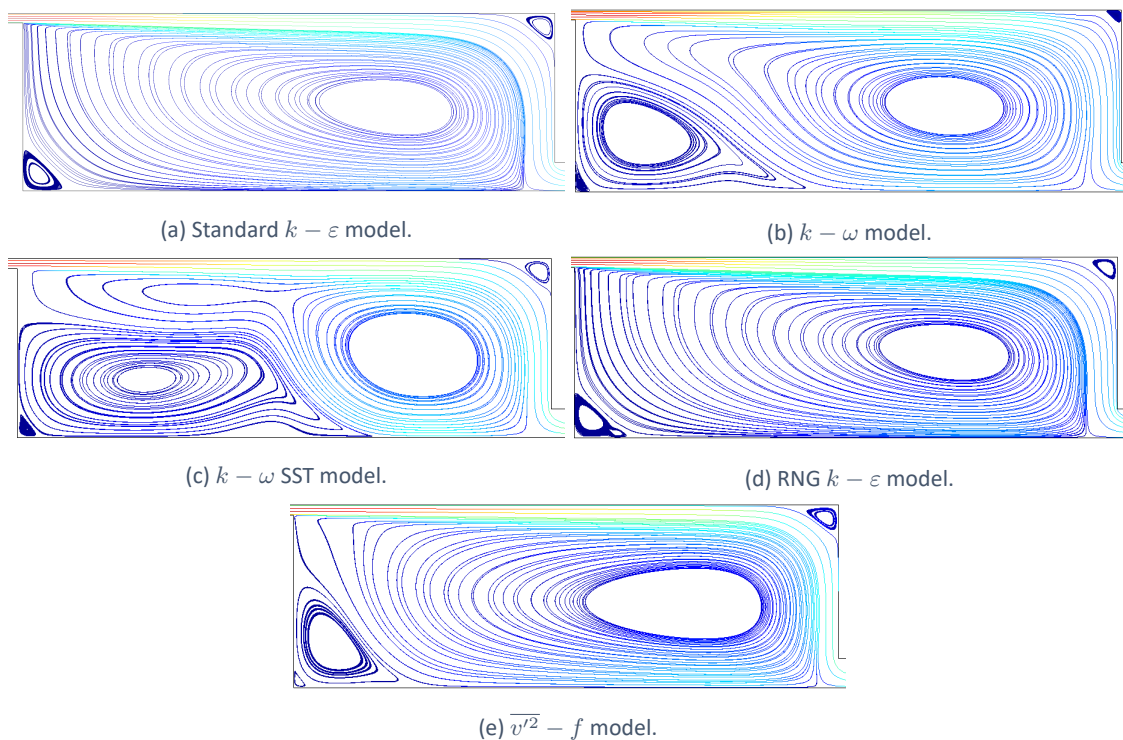


Figure 4.27 – Velocity magnitude (U/U_0) for the turbulence models tested.

Results for the realizable $k-\varepsilon$ turbulence model are absent because it was not possible to achieve convergence. The standard and RNG $k-\varepsilon$ models, figures 4.27a and 4.27d, show similar flow patterns:

- large flow circulation was produced between the inlet and outlet;
- recirculating flow is found on the top, right corner and bottom, left corner;
- large stagnant flow region is generated slightly to the right of the room center.

The $\overline{v'^2}-f$ model shows the same tendency as the standard and RNG $k-\varepsilon$ models. However, it produces a larger recirculation on the bottom left corner than the $k-\varepsilon$ models. For the $k-\omega$ SST model the flow detaches from the bottom wall (floor) closely to the room center. A considerably large recirculating zone is generated below the supplied jet at $0 < x/H < 2$. The $k-\omega$ model produces resembling results, but with a smaller recirculation area below the supplied jet, $0 < x/H < 1.5$. These models also present a large stagnation flow region as the $k-\varepsilon$ models.

The turbulent kinetic energy, k , for all models is shown in figure 4.28.

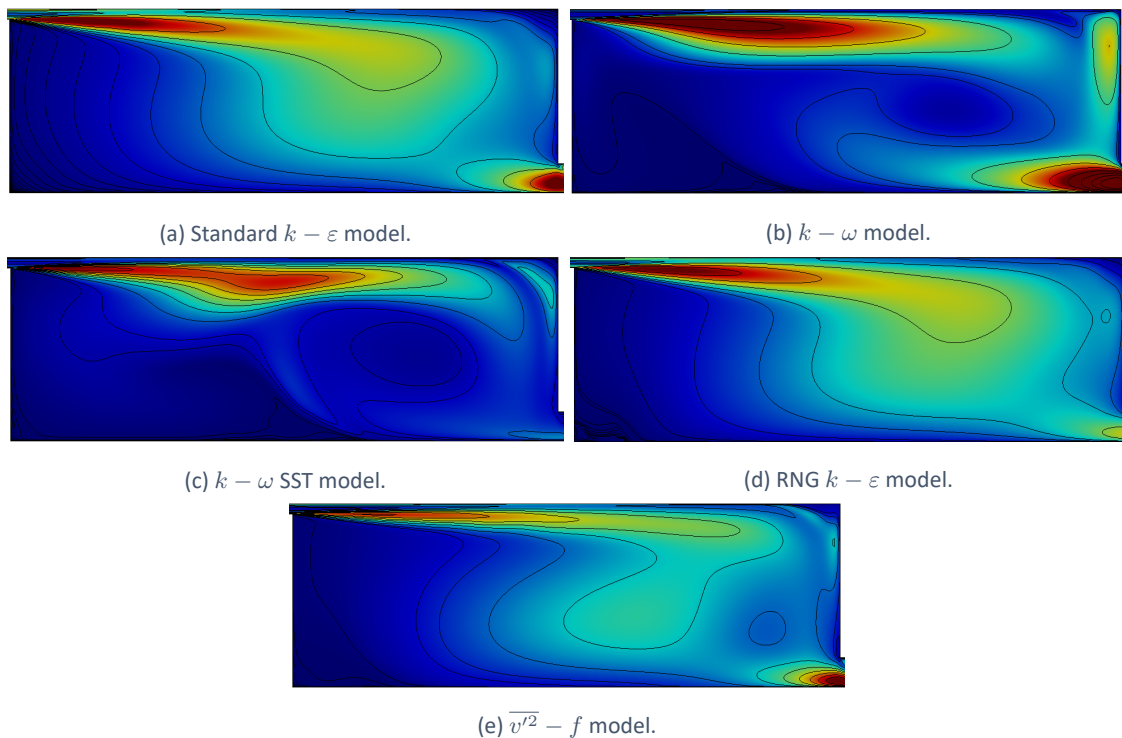


Figure 4.28 – Turbulent kinetic energy (k) for the turbulence models tested.

Turbulent kinetic energy predictions are very much like the same between the standard and RNG $k-\varepsilon$ models. The RNG $k-\varepsilon$ generates, in the occupied room, a slightly larger area of turbulence levels than the standard $k-\varepsilon$. The $\overline{v'^2}-f$ model predicts lower values and more disperse area of the turbulent kinetic energy, when compared with the $k-\varepsilon$ models. The $k-\omega$ models generate jets with higher levels of turbulence, although low levels of turbulent kinetic energy in the occupied room are shown. At the exhaust opening, the $k-\omega$ model, the standard $k-\varepsilon$ model and the $\overline{v'^2}-f$ model present higher levels of turbulent intensity, specially the $k-\omega$ SST model.

Vertical and horizontal sections, as in the mesh independence study (fig. 4.16), were taken to analyse the velocity profile, U/U_0 , and turbulent kinetic energy, calculated from equation 4.9. The computational models data shown in figures 4.29 - 4.34, are compared with experimental measurements [20].

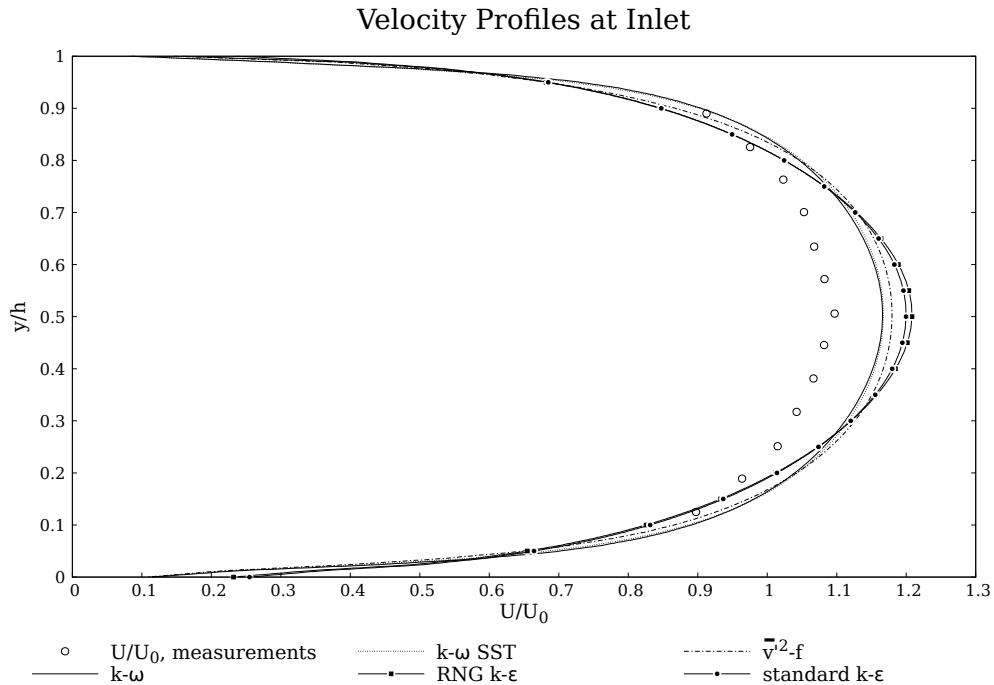


Figure 4.29 – Velocity Profiles (U/U_0) at the inlet for different turbulence models and experiment measurements performed by Nielsen [7].

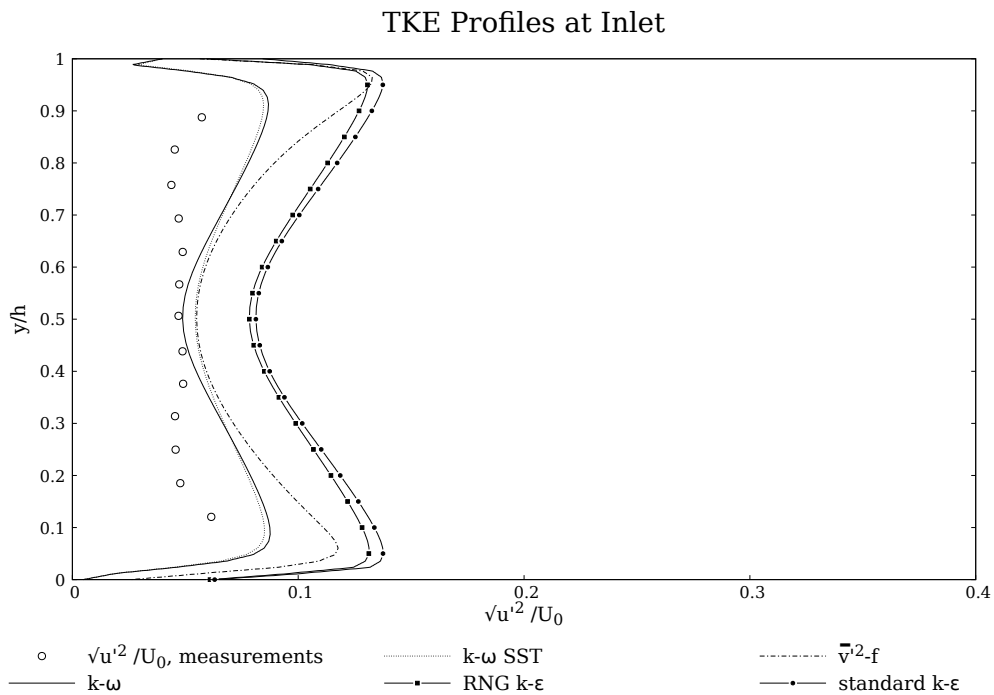


Figure 4.30 – Turbulent kinetic energy in terms of root-mean square (RMS) velocity profiles ($\sqrt{u'^2}/U_0$) at the inlet, for different turbulence models and experiment measurements performed by Nielsen [7].

Horizontal Velocity Profiles

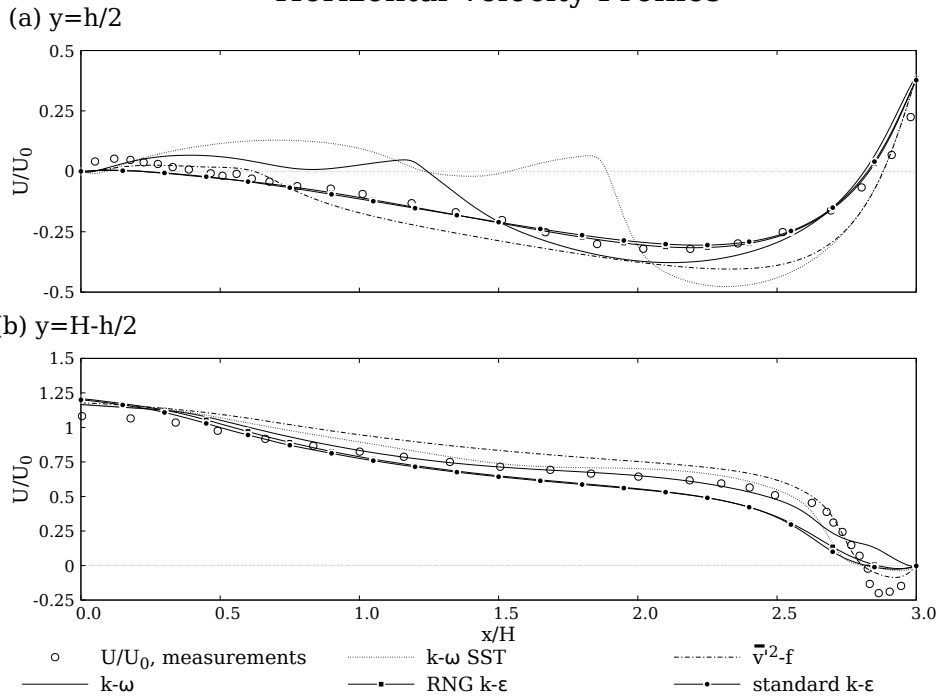


Figure 4.31 – Velocity Profiles (U/U_0) at $y = H - h/2$ and $y = h/2$ for different turbulence models and experiment measurements performed by Nielsen [7].

Horizontal TKE Profiles

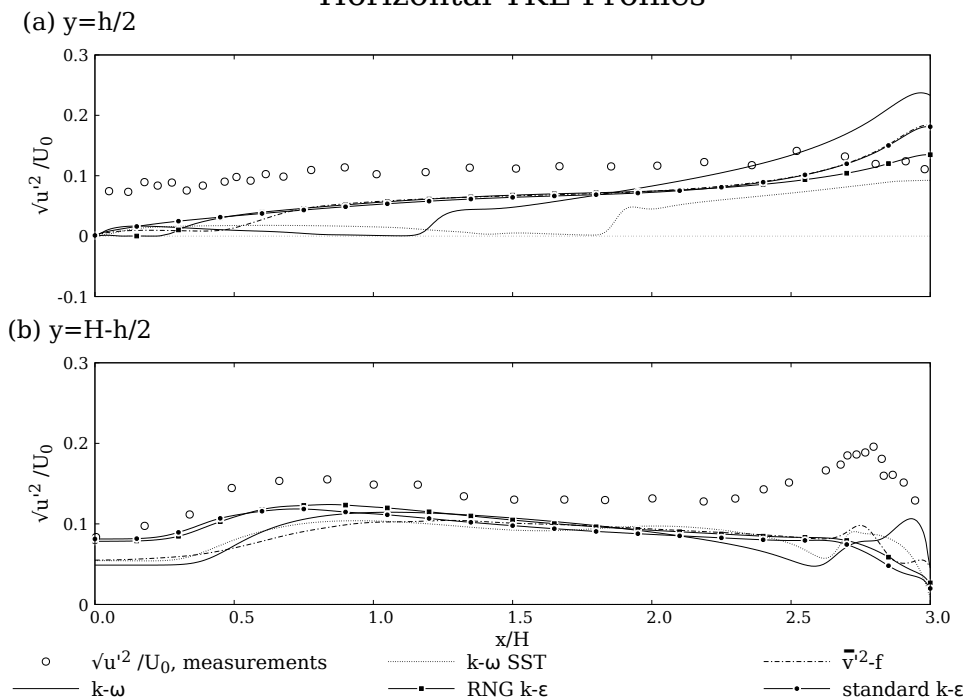


Figure 4.32 – RMS velocity profiles ($\sqrt{u'^2}/U_0$) at $y = H - h/2$ and $y = h/2$ for different turbulence models and experiment measurements performed by Nielsen [7].

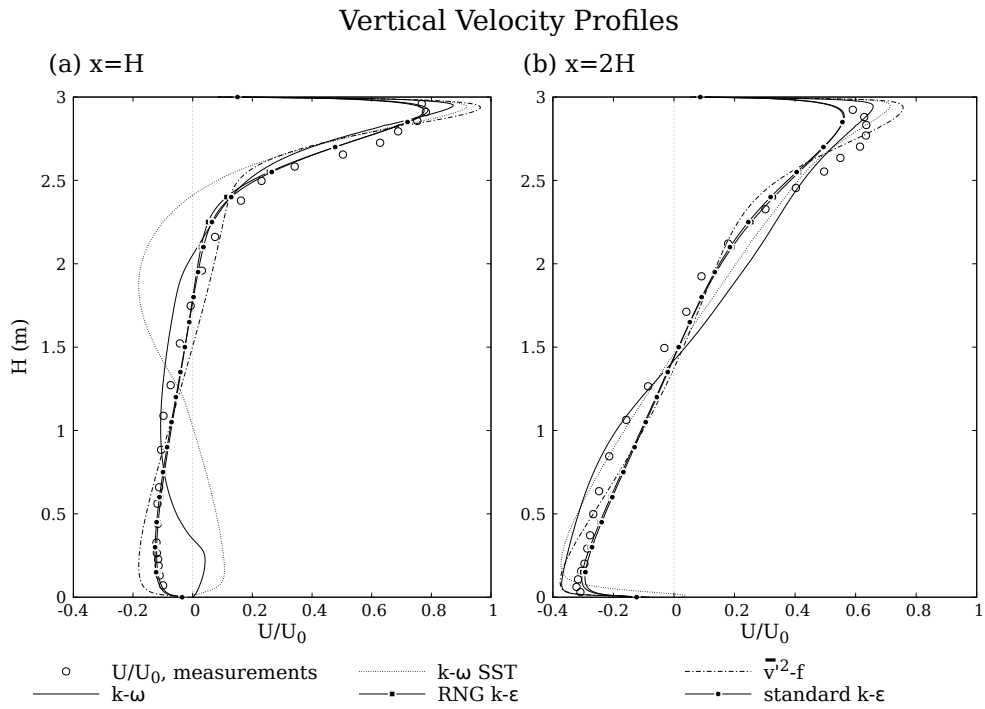


Figure 4.33 – Velocity Profiles (\mathbf{U}/U_0) at $x = H$ and $x = 2H$ for different turbulence models and experiment measurements performed by Nielsen [7].

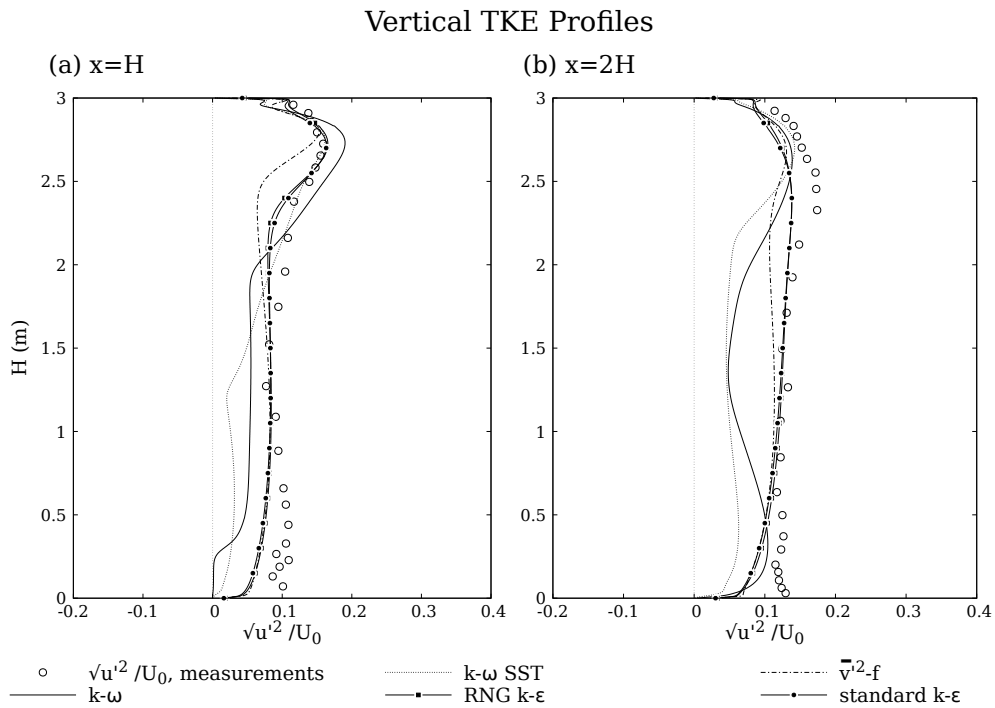


Figure 4.34 – RMS velocity profiles ($\sqrt{u'^2}/U_0$) at $x = H$ and $x = 2H$ for different turbulence models and experiment measurements performed by Nielsen [7].

The velocity profiles, for the different models at the inlet (fig. 4.29), show similar predictions, however slightly higher values than the experimental data. The turbulent energy is over-predicted at the inlet by all turbulence models (fig. 4.30), in particularly by the $k - \varepsilon$ models. The same behaviour is not verified inside the room (occupied area).

The $k - \omega$ and $k - \omega$ SST, present very disparate results from the experimental data. This is noticeable at the middle region (far from the walls) and near the floor at $x = H$ (fig. 4.33). This near wall behaviour at $x = H$ is caused by the $k - \omega$ models prediction of the flow recirculation area (fig. 4.27b; fig. 4.27c), which can be reinforced by the velocity profile analysis at $y = h/2$ (fig. 4.31).

Overall, the predictions made by the $k - \varepsilon$ and the RNG $k - \varepsilon$ models are the ones in closest agreement with the experimental results. Nonetheless, the $k - \varepsilon$ present more stability and required less time to converge, therefore this model was chosen to perform the following simulations.

4.2.4 Post-Processing

4.2.4.1 Residuals and Convergence

For a steady-state simulation the number of iterations is limited (fig. 4.36). However, for a transient simulation the number of iterations per time step is defined (fig. 4.35).

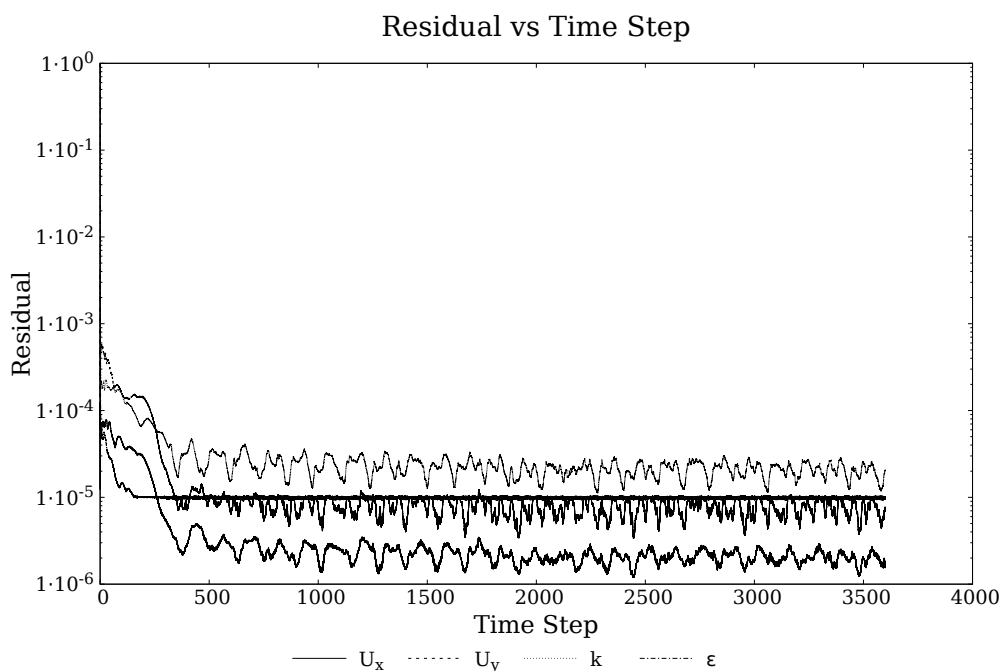


Figure 4.35 – Residuals for the main variables at study (U , k and ε) for transient solver.

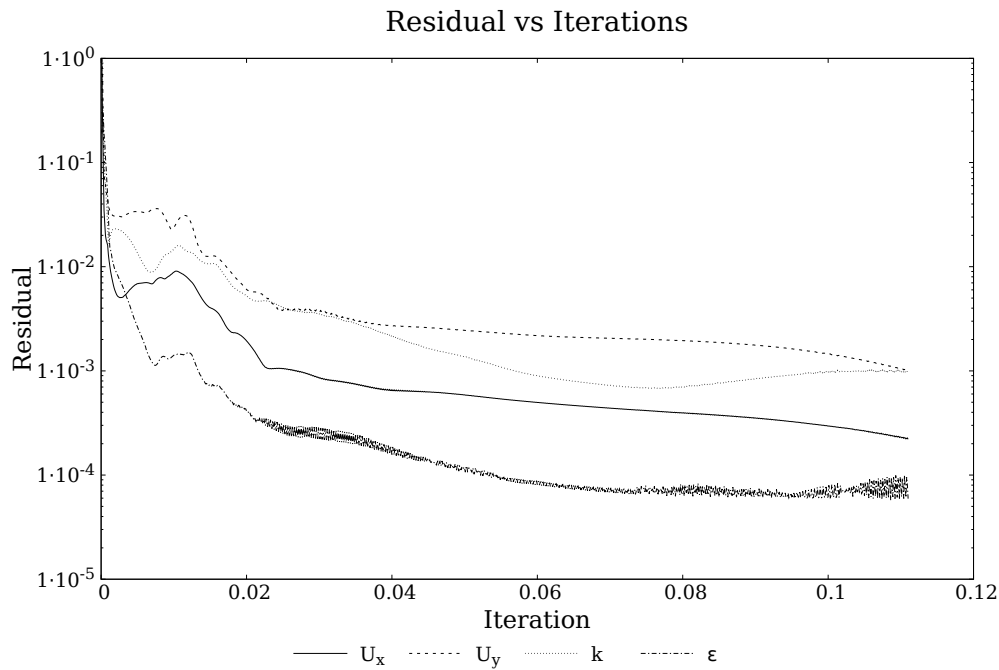


Figure 4.36 – Residuals for the main variables at study (U , k and ϵ) for steady-state solver.

4.2.4.2 Results

The computational results here highlighted are those generated with the standard $k - \epsilon$ model. The mean velocity, the velocity vector field and the turbulent kinetic energy are shown in figures 4.37, 4.38 and 4.39, respectively.

The computational results are compared at the horizontal and vertical lines from figure 4.16, $x = H$, $x = 2H$, $y = H - h/2$, $y = h/2$ and $x = 0H$ (inlet), with the experimental measurements performed by Nielsen [20].

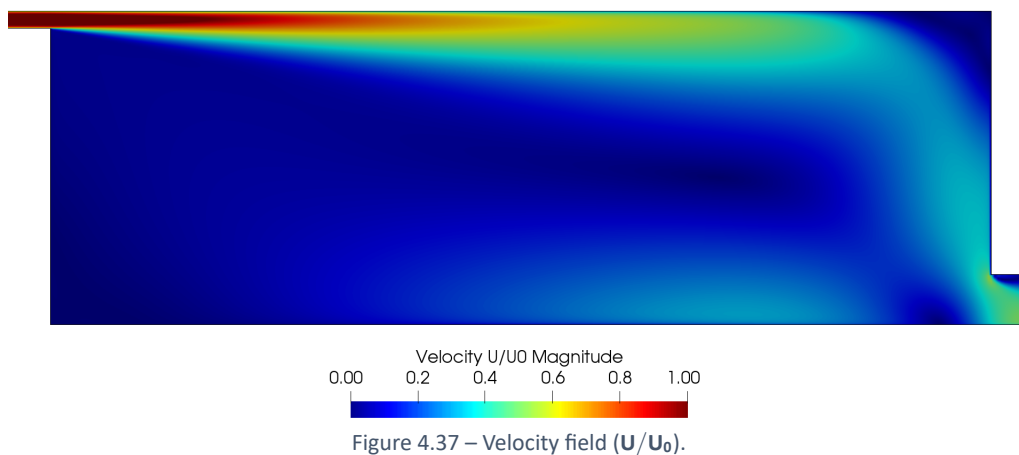


Figure 4.37 – Velocity field (U/U_0).

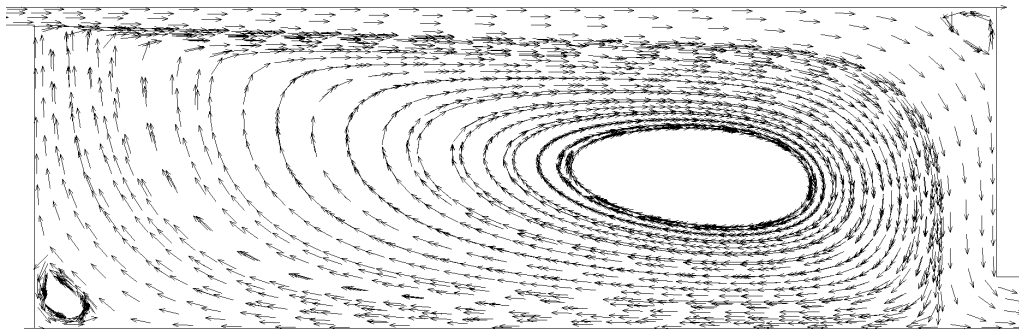


Figure 4.38 – Velocity vector field.

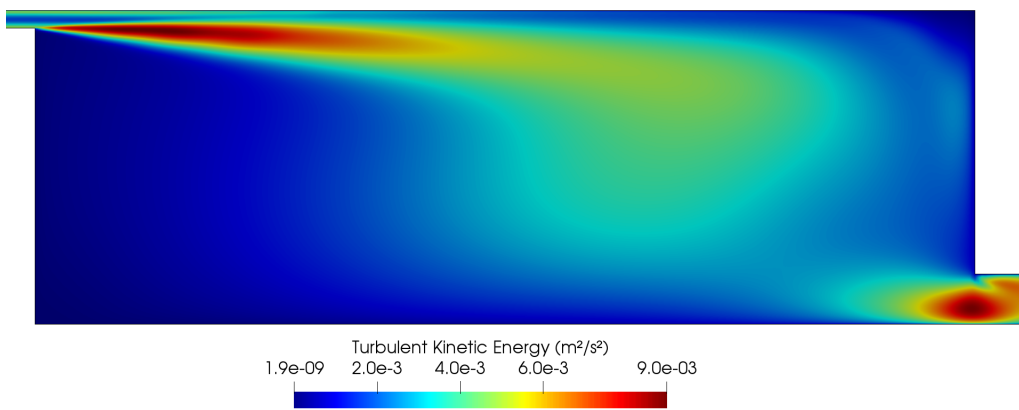


Figure 4.39 – Turbulent kinetic energy (k (m²/s²)).

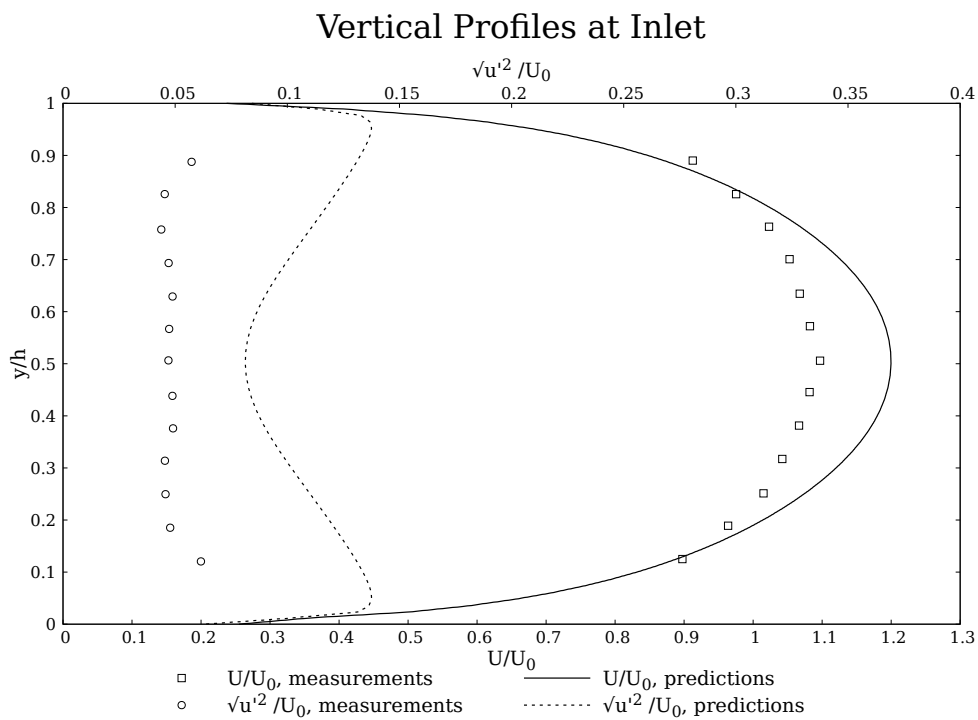


Figure 4.40 – Comparison between computed results for mean velocity (U/U_0) and RMS velocity ($\sqrt{u'^2}/U_0$) with experiment measurements performed by Nielsen [7] at the supply opening.

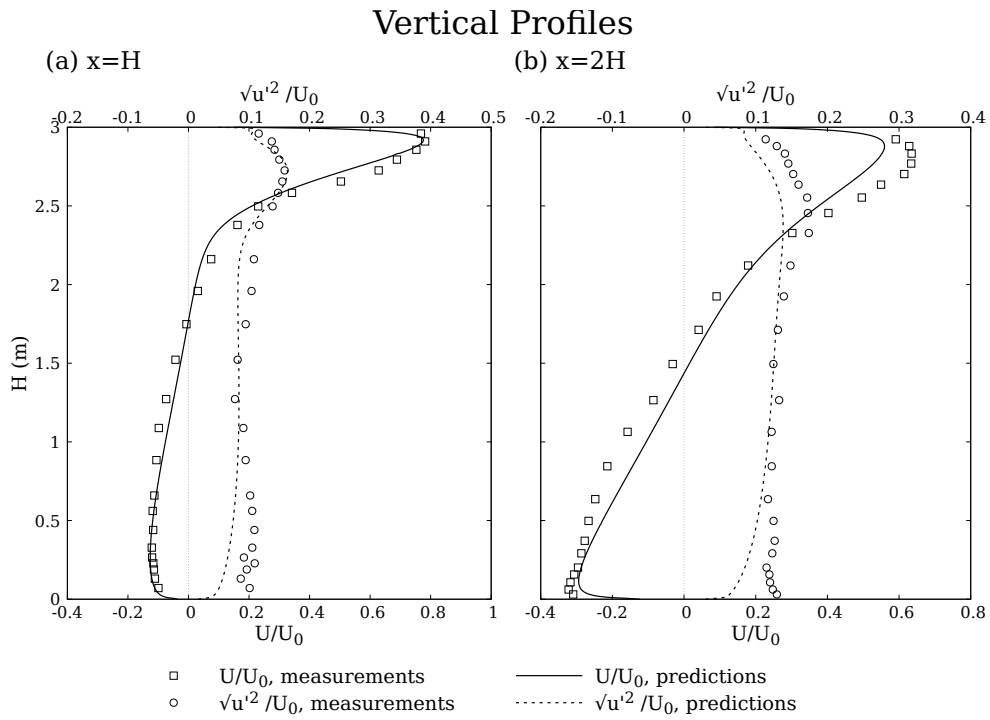


Figure 4.41 – Comparison between computed results for mean velocity (U/U_0) and RMS velocity ($\sqrt{u'^2}/U_0$) with experiment measurements performed by Nielsen [7] at $x = H$ and $x = 2H$.

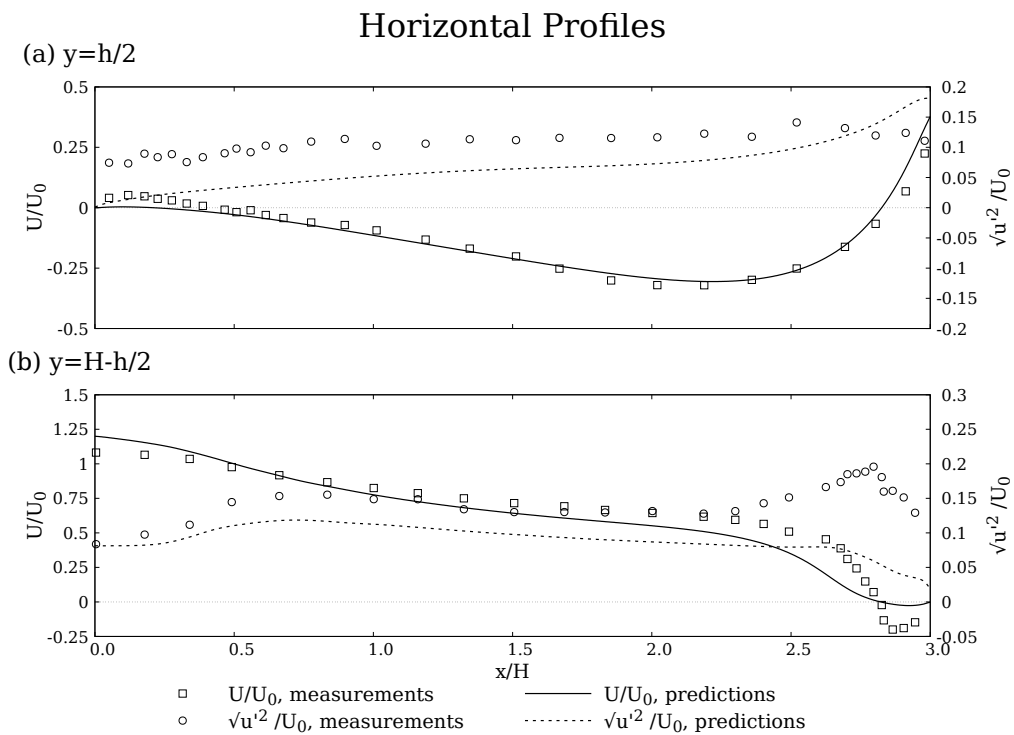


Figure 4.42 – Comparison between computed results for mean velocity (U/U_0) and RMS velocity ($\sqrt{u'^2}/U_0$) with experiment measurements performed by Nielsen [7] at $y = h/2$ and $y = H - h/2$.

4.2.4.3 Conclusions

This case allowed to draw some of the same conclusions as the previous case. Boundary conditions must be evaluated, wall treatment and mesh independence studies should always be performed, to ensure mesh quality and results accuracy.

Here additional conclusions can be made:

- 1°. Better simulation performance with the transient solver. The steady-state solution achieved by the transient solver proved to be superior to the use of a steady-state solver. In this situation, the computational results are in good agreement with experimental data.
- 2°. From the turbulence models studied, the standard and RNG $k - \varepsilon$, are the ones in closest agreement with the experimental results.
- 3°. The performed turbulence models simulations showed some main common features:
 - a. large flow was produced between the supply and exhaust opening;
 - b. stagnant flow region was produced near the middle of the room;
 - c. small recirculation was observed in the top right corner;
 - d. recirculation bellow the supplied air jet was observed and it varies between models. The $k - \omega$ models exhibit larger recirculation area than the $k - \varepsilon$ models.
- 4°. The $\overline{v'^2} - f$ model showed a similar behaviour tendency as the $k - \varepsilon$ models. Considering the $\overline{v'^2} - f$ model formulation, presenter in chapter 3, it it was reasonably concluded that results closely to the $k - \varepsilon$ models will be possible to achieved for a higher number of mesh cells. This can be explained, by the fact that the $\overline{v'^2} - f$ model uses a damping approach of the turbulent transport close to the wall technique (use of the elliptic relaxation function, f).

4.3 2D non-Isothermal Test Case in Annex 20

4.3.1 Introduction

In this section a 2D non-isothermal benchmark from the IEA Annex 20 [6] was studied. Temperature gradients are usually present in ventilated rooms. Energy is transported throughout the room and interacts with the flow, inducing buoyancy effects that affect the mean velocity and the turbulence [167]. This case goal is to predict flow with strong buoyancy effects, which are often expressed by an Archimedes number.

4.3.2 Test Case Specifications

The case geometry, from the Annex 20 room benchmark is shown in figure 4.43, it is the same as the 2D isothermal test case. For the present case the mesh independence study was already performed in the isothermal case. Therefore, the mesh used for this case is the same as before (mesh 6, fig. 7.6).

For this case a constant heat flux (q'') is added to the floor of the room. The remaining walls are assumed to be adiabatic. Several simulations were performed for increasing Archimedes number (increasing heat flux). As a result, the influence of temperature variation (buoyancy effects) on the flow and wall jet behaviour can be assessed. The experiment was performed for two different Reynolds numbers, $Re = 5000$ and $Re = 7100$.

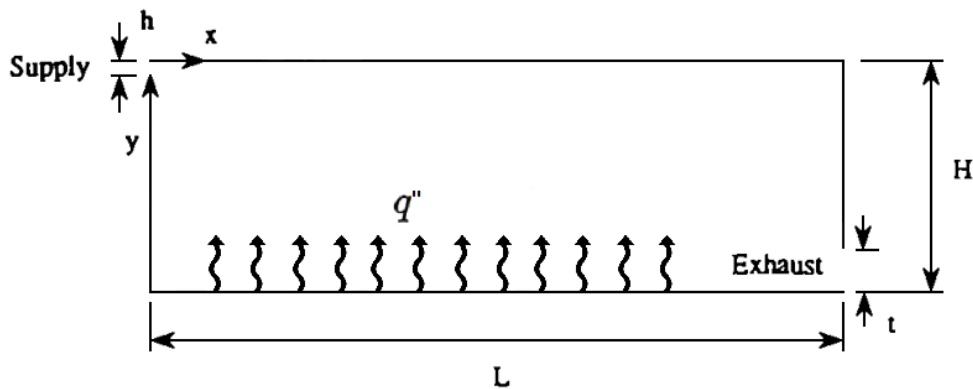


Figure 4.43 – Sketch of the two-dimensional non-isothermal test case.

The Archimedes number is defined as:

$$Ar = \frac{\beta \cdot g \cdot h \cdot \Delta T_0}{U_0^2} \quad (4.10)$$

where β is the volumetric expansion coefficient, g is the gravitational acceleration and ΔT_0 is the mean temperature difference between supply and exhaust opening.

4.3.3 Pre-Processing

4.3.3.1 Boundary Conditions

The boundary conditions for the velocity and turbulence parameters of Annex 20 2D non-isothermal room, for the two Reynolds numbers, for the inlet, outlet and walls are presented in tables 4.11, 4.12 and 4.13, respectively.

Table 4.11 – Non-isothermal room supply opening boundary conditions.

Field	Boundary Condition	
	$Re = 5000$	$Re = 7100$
\mathbf{U}	(0.455 0 0)	(0.65 0 0)
p	<i>zeroGradient</i>	<i>zeroGradient</i>
ν_t	<i>calculated</i>	<i>calculated</i>
k	4.9686×10^{-4}	1.0140×10^{-3}
ε	1.0832×10^{-4}	3.1581×10^{-4}
p_{rgh}	<i>fixedFluxPressure</i>	<i>fixedFluxPressure</i>
T	293.15	293.15
α_t	0	0

Table 4.12 – Non-isothermal room exhaust opening boundary conditions.

Field	Boundary Condition	
	$Re = 5000$	$Re = 7100$
\mathbf{U}	<i>zeroGradient</i>	<i>zeroGradient</i>
p	0	0
ν_t	<i>calculated</i>	<i>calculated</i>
k	<i>zeroGradient</i>	<i>zeroGradient</i>
ε	<i>zeroGradient</i>	<i>zeroGradient</i>
p_{rgh}	0	0
T	<i>zeroGradient</i>	<i>zeroGradient</i>
α_t	<i>zeroGradient</i>	<i>zeroGradient</i>

For the temperature boundary condition at all the walls, except the room floor, was implemented a *zeroGradient* boundary condition. In the room floor *groovyBC* tools were used to implement a gradient expression to introduce a constant heat flux (q'') at the wall. From Fourier's law

$$q'' = -k_{fluid} \nabla T \quad \text{W/m}^2 \quad (4.11)$$

where k_{fluid} is the thermal conductivity and $q'' = q/A$. Therefore the gradient expression normal to the wall is:

$$\nabla T = \frac{q}{k_{fluid} A} \quad (4.12)$$

Table 4.13 – Non-isothermal room walls boundary conditions.

Field	Boundary Condition	
	$Re = 5000$	$Re = 7100$
\mathbf{U}	<i>noSlip</i>	<i>noSlip</i>
p	<i>zeroGradient</i>	<i>zeroGradient</i>
ν_t	<i>nutkWallFunction</i>	<i>nutkWallFunction</i>
k	<i>kqRWallFunction</i>	<i>kqRWallFunction</i>
ε	<i>epsilonWallFunction</i>	<i>epsilonWallFunction</i>
p_{rgh}	<i>fixedFluxPressure</i>	<i>fixedFluxPressure</i>
T	<i>zeroGradient</i>	<i>zeroGradient</i>
α_t	<i>alphatJayatillekeWallFunction</i> ($Pr_t = 0.85$) ^a	<i>alphatJayatillekeWallFunction</i> ($Pr_t = 0.85$)

^aTurbulent Prandtl number was retrieved from experimental data [168, 169].

4.3.3.2 Solver

Solver validation was performed by comparing the transient solver for buoyant, turbulent flow of incompressible fluids, *buoyantBoussinesqPimpleFoam*, with the transient solver for incompressible, turbulent flow previously studied *pimpleFoam*. Simulations were performed by considering an uniform temperature of the room and all walls assumed to be adiabatic (isothermal test case conditions).

Vertical Profiles at Inlet for different solvers

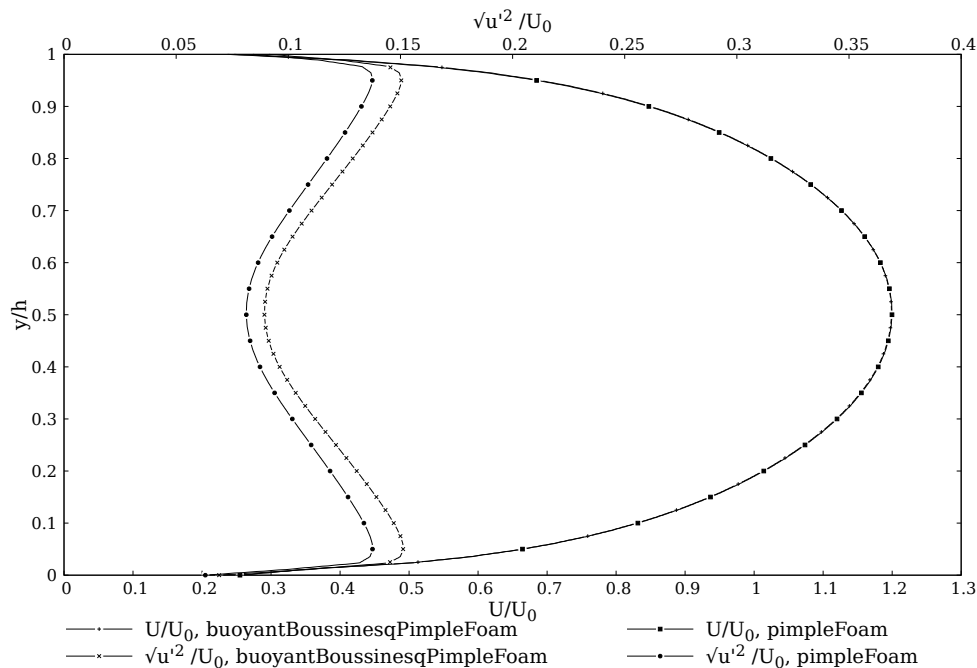


Figure 4.44 – Isothermal and non-Isothermal solver comparison, for the velocity field magnitude (\mathbf{U}/U_0) and RMS velocity ($\sqrt{u'^2}/U_0$) at the inlet.

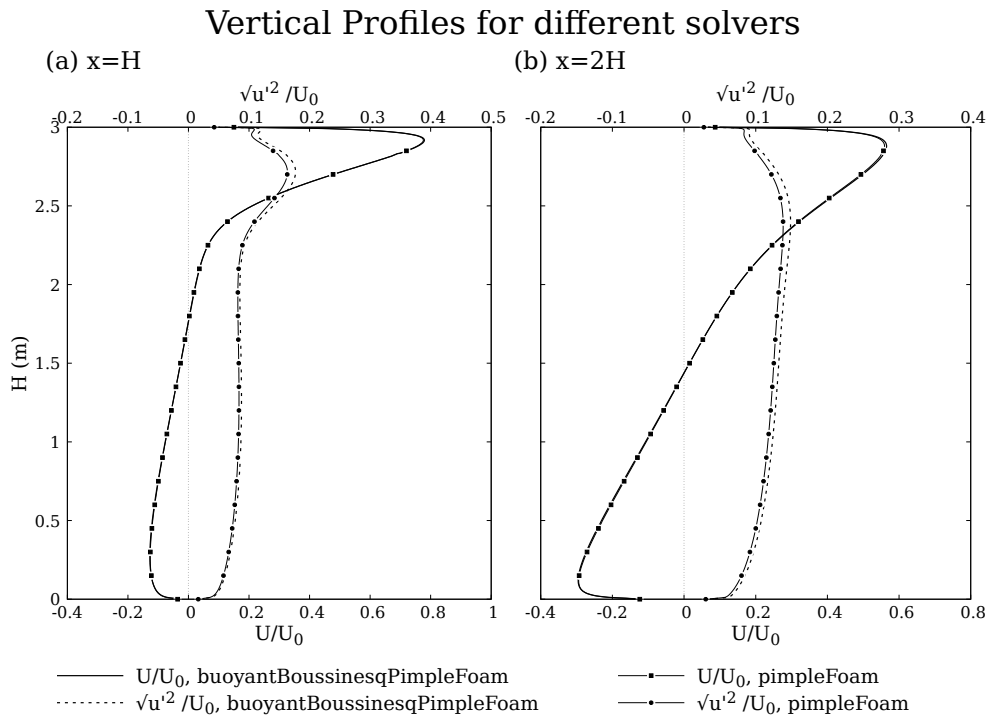


Figure 4.45 – Isothermal and non-Isothermal solver comparison, for the velocity field magnitude (\mathbf{U}/U_0) and RMS velocity ($\sqrt{u'^2}/U_0$) at $x = H$ and $x = 2H$.

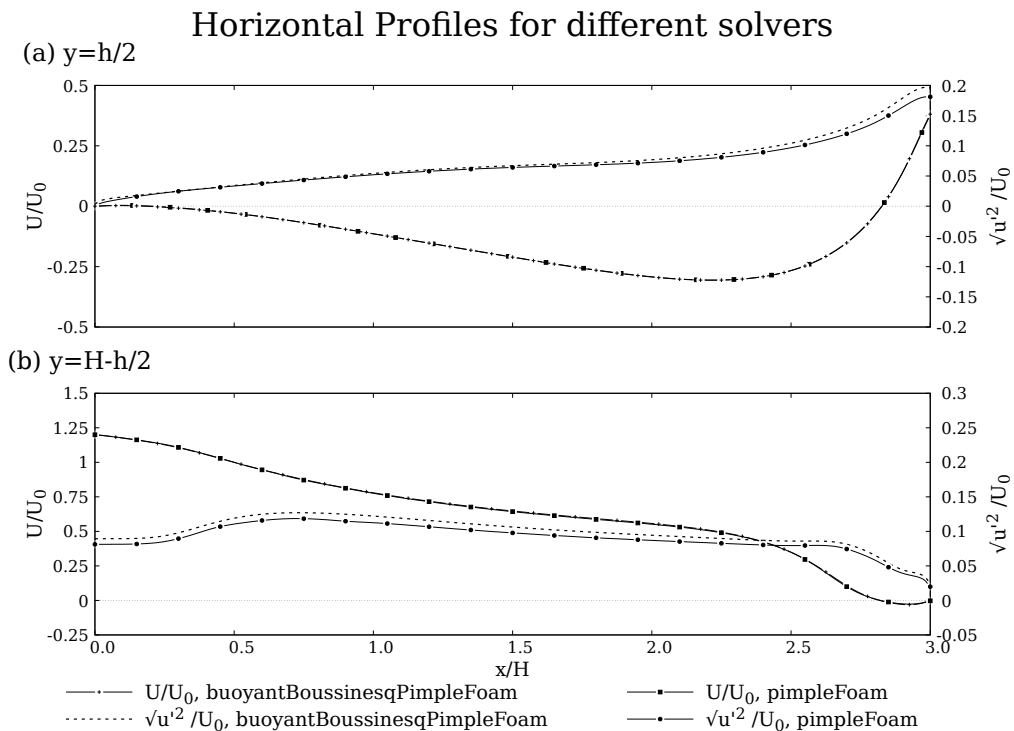


Figure 4.46 – Isothermal and non-Isothermal solver comparison, for the velocity field magnitude (\mathbf{U}/U_0) and RMS velocity ($\sqrt{u'^2}/U_0$) at $y = h/2$ and $y = H - h/2$.

The *buoyantBoussinesqPimpleFoam* solver shows good agreement with *pimpleFoam* in predicting the velocity field. In terms of turbulent kinetic energy, the results are slightly over-predicted when compared to the incompressible solver (maximum increase of about 7%.)

4.3.3.3 Turbulence Model and Numerics

In agreement with the previous cases conclusions, first order divergence schemes, Gauss Upwind, was used to discretize the convection and diffusion terms. First order *Euler* implicit time scheme was implemented, in order to determine time derivative of variables. For the pressure-velocity coupling, the PIMPLE algorithm is used. Correctors are used ($nOuterCorrectors = 1$ and $nCorrectors = 2$). An adjustable time step function was used with a maximum Courant number of 1.

Under-relaxation factors were implemented. For matrix manipulation, the here solvers used to converge the solution to the required tolerance were:

- For p_{rgh} , a preconditioned conjugate gradient solver for symmetric matrices (PCG), with a simplified diagonal-based incomplete Cholesky preconditioner for symmetric matrices (DIC);
- For U , T , k and ε was used a preconditioned bi-conjugate gradient stabilized solver for asymmetric matrices (PBiCGStab) with a DILU (equivalent to DIC) preconditioner.

The standard $k - \varepsilon$ model is used to predict turbulent quantities, for motives shown in the previous case.

The simulations were carried out on a desktop computer (Intel quad core i3-9100f, 3.60 GHz processor) with OpenFOAM 6.

4.3.4 Post-Processing

4.3.4.1 Results

The effects of the temperature on the mean flow were studied by increasing the heat flux at floor for the two Reynolds numbers. The values testes can be found in table 4.14.

Table 4.14 – Temperature gradient (∇T), heat flux (q'') and ΔT_0 for different Archimedes numbers.

∇T (K/m)	q'' (W/m ²)	ΔT_0 (K or °C)		Ar	
		$Re = 5000$	$Re = 7100$	$Re = 5000$	$Re = 7100$
10	0.25	0.0242	0.0172	6.60×10^{-4}	2.30×10^{-4}
100	2.52	0.2426	0.1706	6.62×10^{-3}	2.28×10^{-3}
500	12.59	1.2137	0.8552	3.31×10^{-2}	1.14×10^{-2}
1000	25.17	2.4321	1.6972	6.64×10^{-2}	2.27×10^{-2}
2000	50.36	4.8694	3.3981	1.33×10^{-1}	4.55×10^{-2}
3000	75.51	7.3050	5.1015	1.99×10^{-1}	6.83×10^{-2}

Nielsen [6] predicted that for the same conditions here presented, for $Re = 5000$, at a $\Delta T_0 = 0.74^\circ\text{C}$ the correspondent Archimedes number is 0.02. The evolution of the Archimedes number for $Re = 5000$ is shown in figure 4.47.

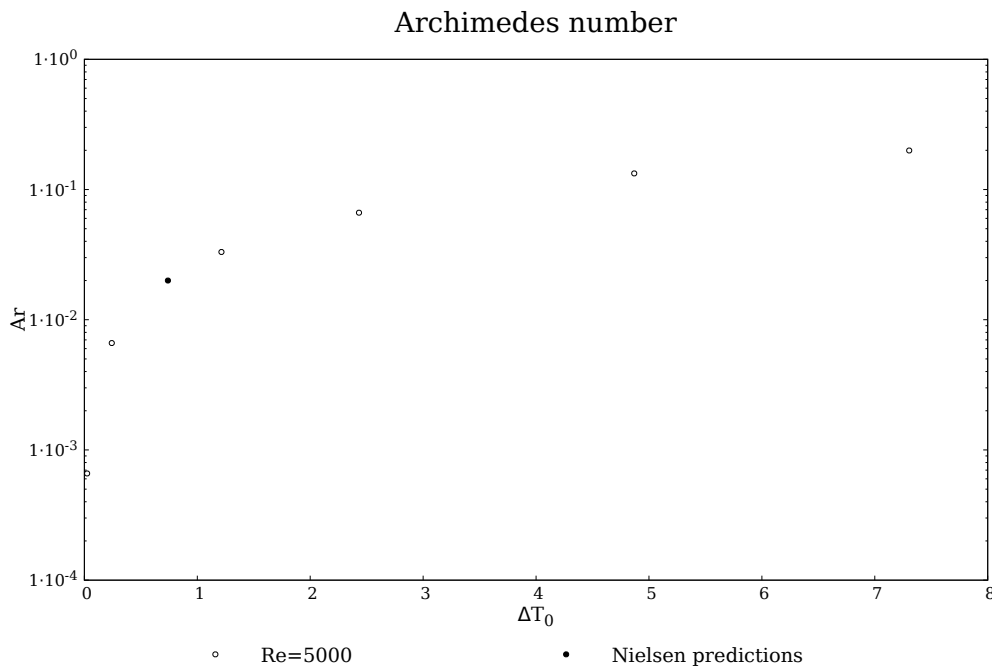


Figure 4.47 – Comparison of Nielsen predictions for $Ar = 0.02$ at $Re = 5000$ and the computational results at $Re = 5000$.

The figures 4.48 and 4.49 present computational results for increasing Archimedes numbers at $Re = 5000$ and $Re = 7100$, respectively. Temperature contours and velocity streamlines can be found in annex 7.6, figures 7.16 and 7.17.

$Re = 5000$

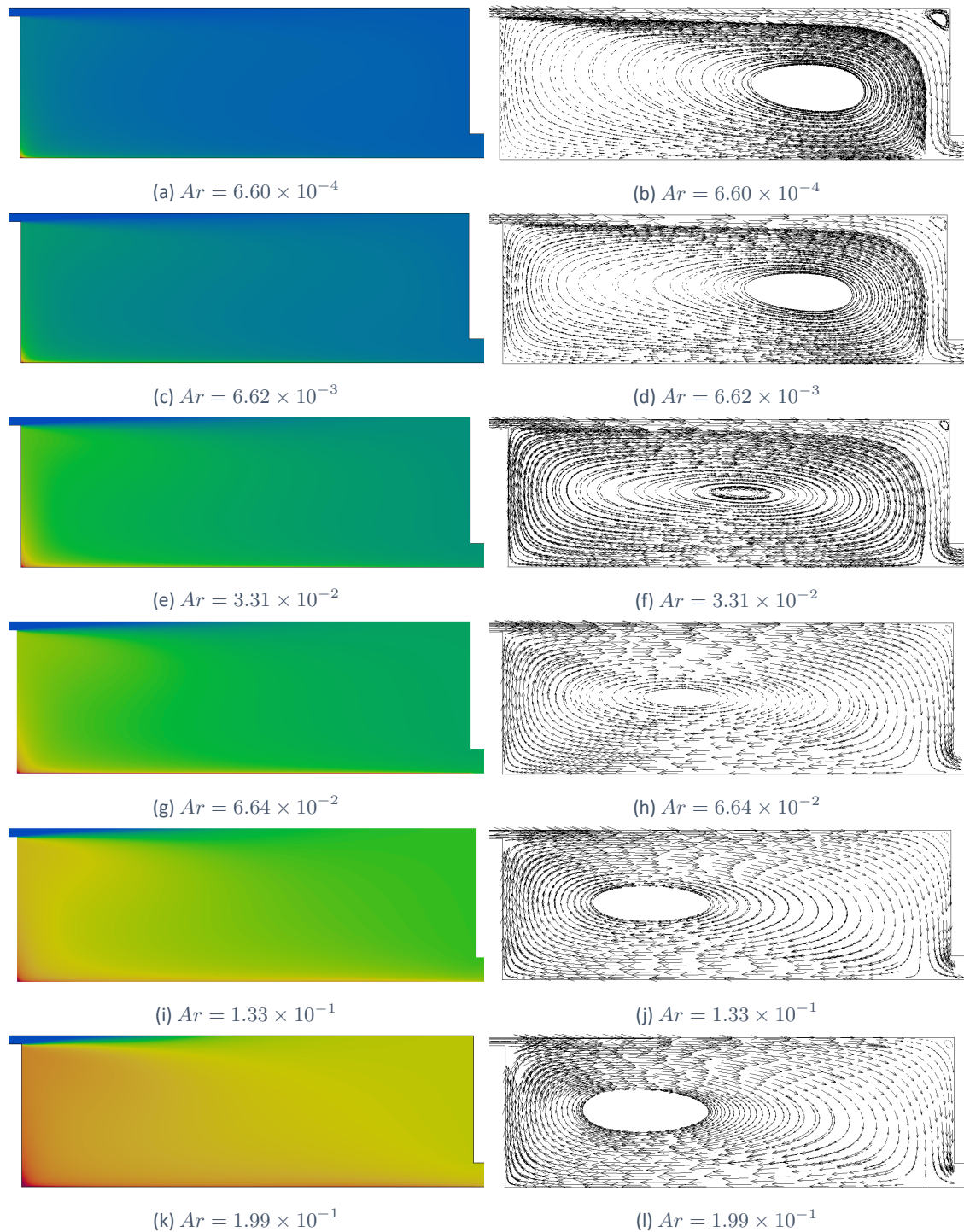


Figure 4.48 – Temperature stratification and velocity vector field at $Re = 5000$, for different Archimedes numbers.

By increasing the heat flux applied to the bottom wall, it was possible to verify that for these velocities ($Re = 5000$ and $Re = 71000$), buoyancy affects significantly the flow. Buoyancy has more influence in flows with lower velocities (fig. 4.48) than slightly higher ones (fig. 4.49). The stagnation area "moves" to the left side of the room at inferior Archimedes number, for example figure 4.48f compared with figure 4.49f.

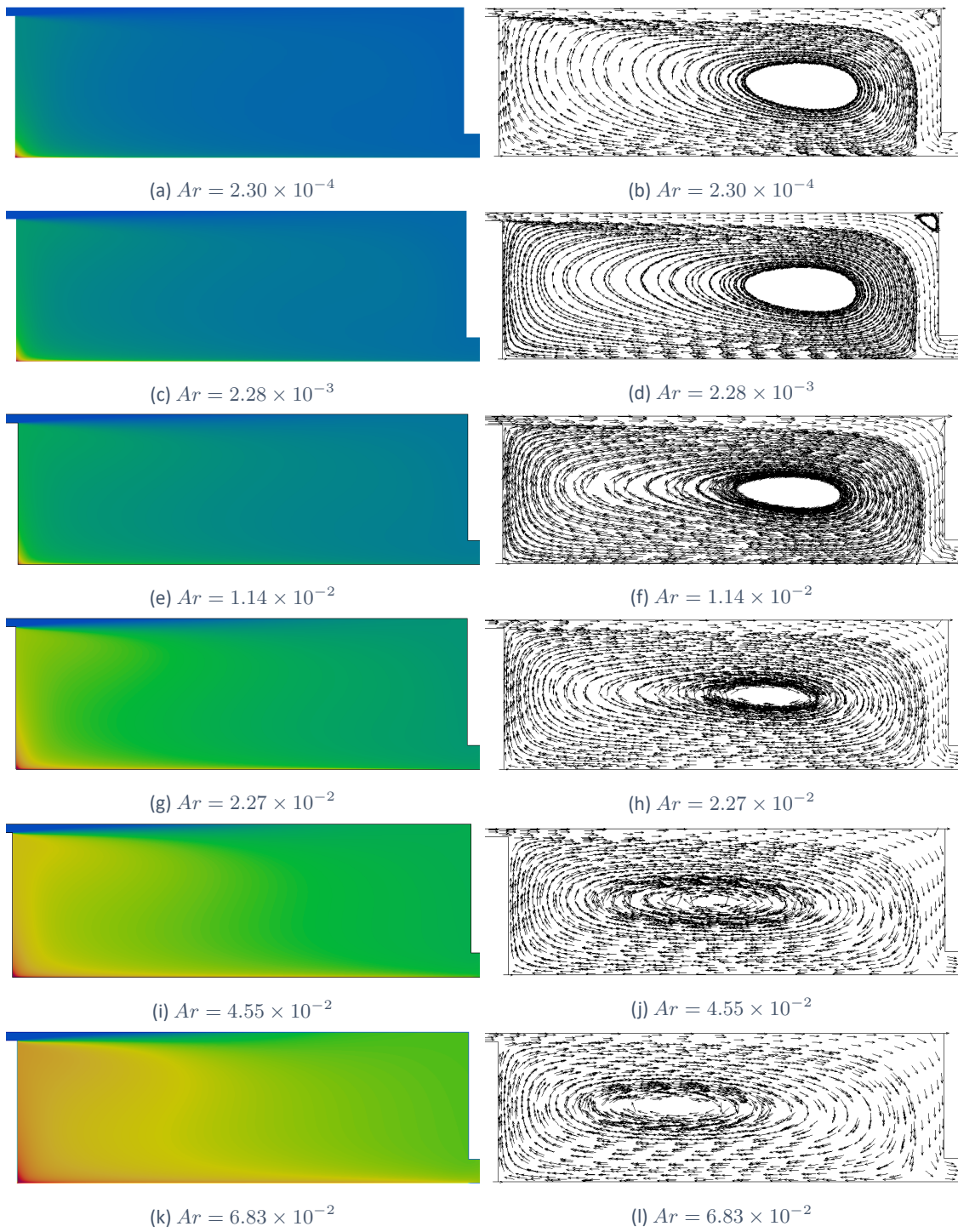
$Re = 7100$ 

Figure 4.49 – Temperature stratification and velocity vector field at $Re = 7100$, for different Archimedes numbers.

4.3.4.2 Conclusions

The introduction of a constant heat flux at the floor, shown strong influence on the mean velocity field:

- 1°. The recirculation near the top, right corner is reduced until it disappears;
- 2°. The recirculation initially present in the bottom left corner does not exist;
- 3°. With the temperature increasing, the stagnation flow region is being "moved" to the left of the occupied room, caused by the increasing of the mean velocity at the floor;
- 4°. The jet maximum velocity decreases;
- 5°. The temperature is significantly higher in the bottom left corner ($x = 0$), due to the small velocity in this region.

4.4 3D Isothermal Test Case in Annex 20

4.4.1 Introduction

It is not always possible to use a two-dimensional geometry. This happens when, for example, the case geometry does not present any symmetry whatsoever or the physical boundary conditions do not allow it, etc. Furthermore, it is possible that certain physical phenomena are being overlooked in the 3rd direction, such as flow recirculation, or turbulence levels are not being predicted correctly.

Thus, in this section a 3D isothermal benchmark from the IEA Annex 20 [6] was studied.

4.4.2 Test Case Specifications

The case geometry, from the Annex 20 3D room benchmark is shown in figure 4.50.

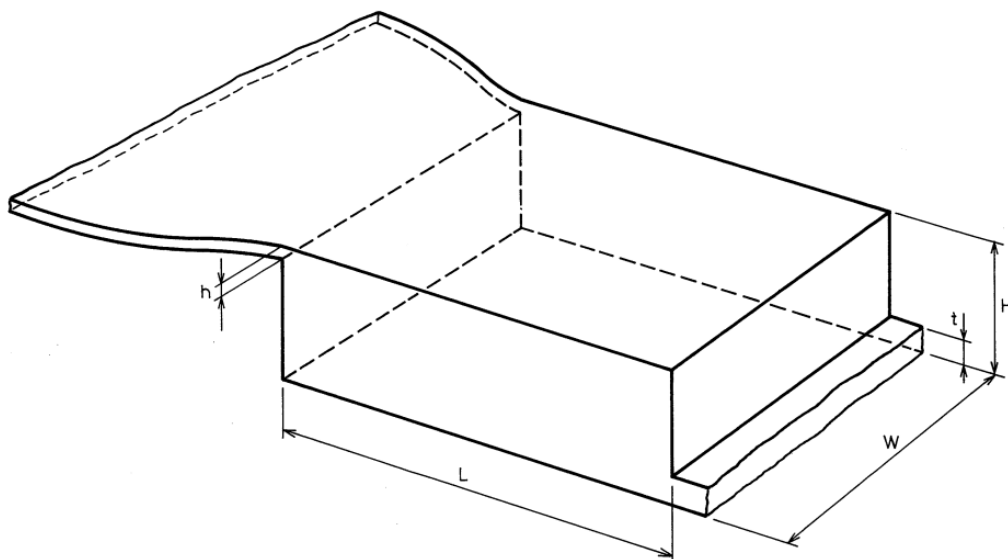


Figure 4.50 – Sketch of the three-dimensional isothermal test case.

The room has the following dimensions:

$$H = 3 \text{ m}, \quad L = 9 \text{ m}, \quad W = 3 \text{ m}, \quad h = 0.168 \text{ m} \quad \text{and} \quad t = 0.48 \text{ m}, \quad (4.13)$$

here, H , L and W are respectively the room high, length and width, h is the supply high and t is the exhaust opening high. The air is supplied on the left at the top and exhausted through the right at the bottom of the room.

The test case conditions are the same as the 2D isothermal room.

4.4.3 Pre-Processing

4.4.3.1 Boundary Conditions

The boundary conditions for the velocity and turbulence parameters of Annex 20 3D isothermal room, for the inlet, outlet and walls are presented in tables 4.15, 4.16 and 4.17, respectively.

Table 4.15 – Room supply opening boundary conditions.

Field	Boundary Condition
U	(0.455 0 0)
<i>p</i>	<i>zeroGradient</i>
ν_t	<i>calculated</i>
<i>k</i>	4.9686×10^{-4}
ε	1.0832×10^{-4}

Table 4.16 – Room exhaust opening boundary conditions.

Field	Boundary Condition
U	<i>zeroGradient</i>
<i>p</i>	0
ν_t	<i>calculated</i>
<i>k</i>	<i>zeroGradient</i>
ε	<i>zeroGradient</i>

Table 4.17 – Room walls boundary conditions.

Field	Boundary Condition
U	<i>noSlip</i>
<i>p</i>	<i>zeroGradient</i>
ν_t	<i>nutkWallFunction</i>
<i>k</i>	<i>kqRWallFunction</i>
ε	<i>epsilonWallFunction</i>

4.4.3.2 Mesh Independence

Three meshes were tested in order to evaluate the the results dependency on the mesh density. There number of cells is presented in table 4.18 and shown in annex 7.7.

Table 4.18 – Number of cells of the meshes studied for the 3D room geometry.

Mesh	Number of cells
coarse	53 000
medium	106 000
fine	462 500

To evaluate mesh independence, for this case three different vertical sections of the room symmetry plane (fig. 4.16) and the variable compared with the LDA experimental results was the velocity (U/U_0).

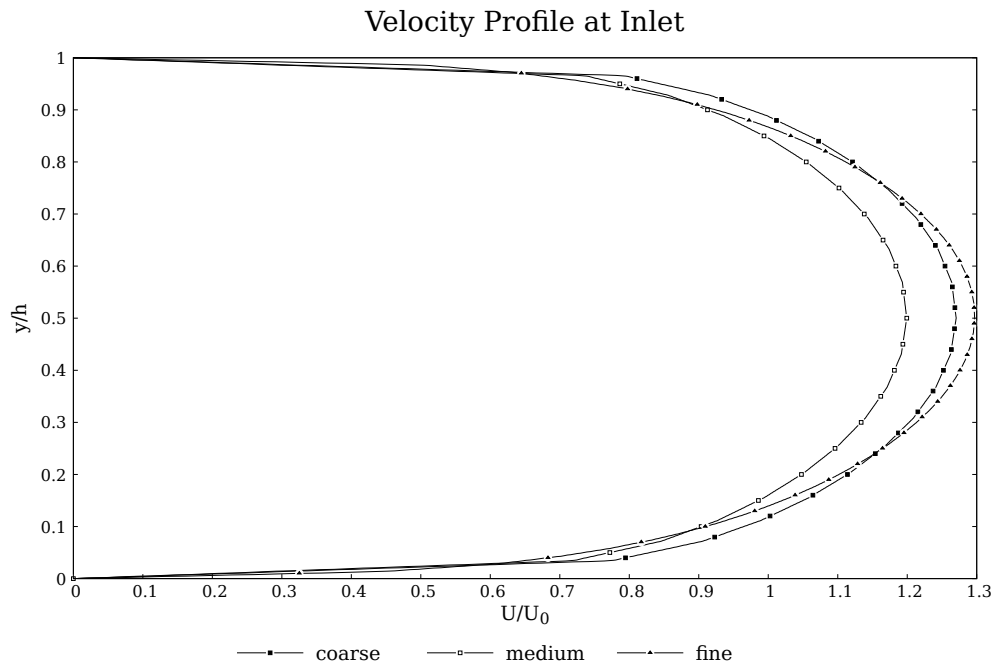


Figure 4.51 – Velocity profile (U/U_0) at the room inlet at the symmetry plane.

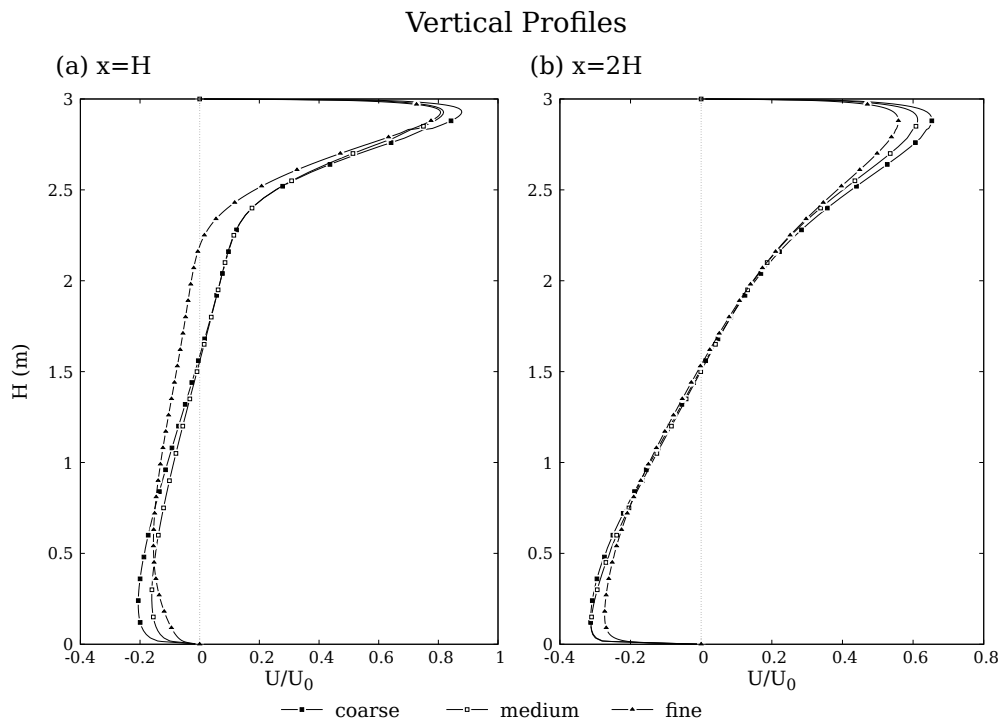


Figure 4.52 – Velocity profile (U/U_0) at $x = H$ and $x = 2H$ at the symmetry plane.

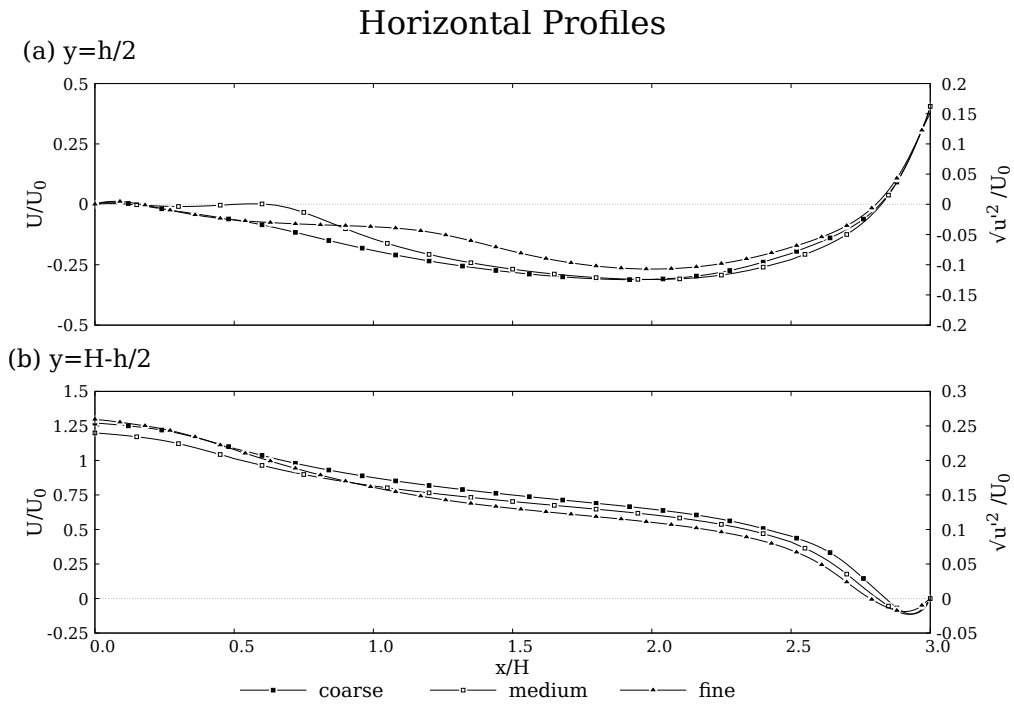


Figure 4.53 – Velocity profile (U/U_0) at $y = h/2$ and $y = H - h/2$ at the symmetry plane.

4.4.3.3 Parallel Running

The Annex 20 3D isothermal test case was decomposed up to six processors by using a simple geometric decomposition by direction (3 2 1), respectively in the x , y and z –directions.

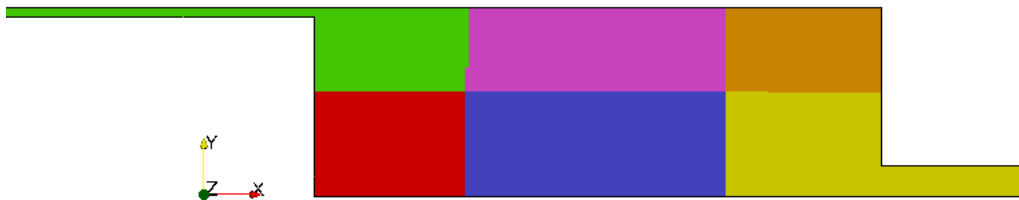


Figure 4.54 – Cell distribution by processor for the IEA Annex 20 3D room.

For the mesh chosen, the cells are distributed by processors as shown in table 4.19.

Table 4.19 – Cell distribution by processor for the IEA Annex 20 3D room.

Processor	Number of cells
0	45759
1	77091
2	108400
3	108408
4	77076
5	45766

4.4.3.4 Turbulence Models and Numerics

In the 3D room case, for the discretization of the convection and diffusion terms, it was chosen a second order divergence scheme, Gauss linearUpwind and bounded Gauss linearUpwind to yield more accurate results than first order schemes.

First order *Euler* implicit time scheme was implemented, in order to determine time derivative of variables.

For the pressure-velocity coupling, the PIMPLE algorithm was used. The implemented Courant number of 1. Smooth solvers based on the Gauss-Seidel method were used to converge the solution to the required tolerance.

The standard $k - \varepsilon$ model is used to predict turbulent quantities, for motives shown in the previous case.

The simulations were carried out on a desktop computer (Intel quad core i3-9100f, 3.60 GHz processor) with OpenFOAM 6.

4.4.4 Post-Processing

4.4.4.1 Results

The figures 4.55, 4.56 and 4.57, show the comparison between computed results for mean velocity (U/U_0) and RMS velocity ($\sqrt{u'^2}/U_0$) with experiment measurements performed by Nielsen [7] at the symmetry plane.

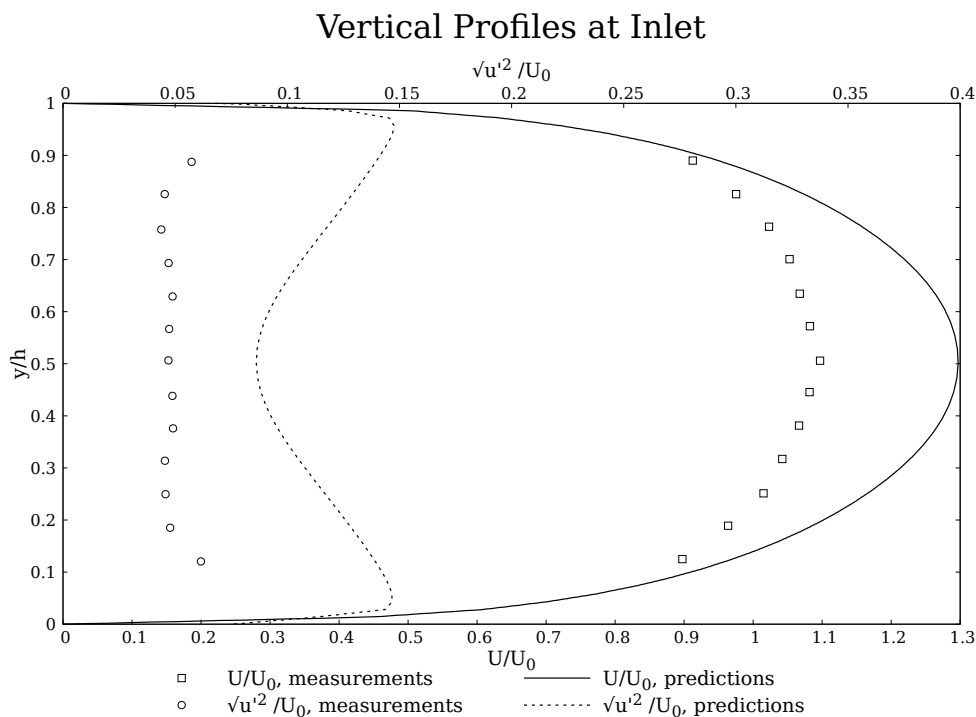


Figure 4.55 – Comparison between computed results for mean velocity (U/U_0) and RMS velocity ($\sqrt{u'^2}/U_0$) with experiment measurements performed by Nielsen [7] at the supply opening (symmetry plane).

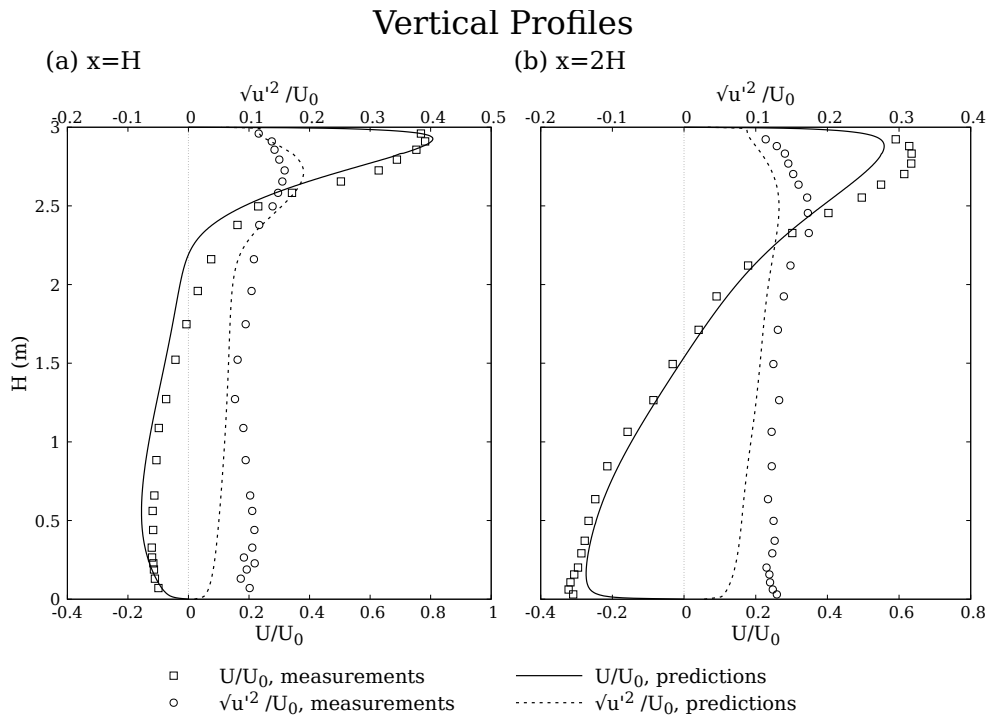


Figure 4.56 – Comparison between computed results for mean velocity (U/U_0) and RMS velocity ($\sqrt{u'^2}/U_0$) with experiment measurements performed by Nielsen [7] at $x = H$ and $x = 2H$ (symmetry plane).

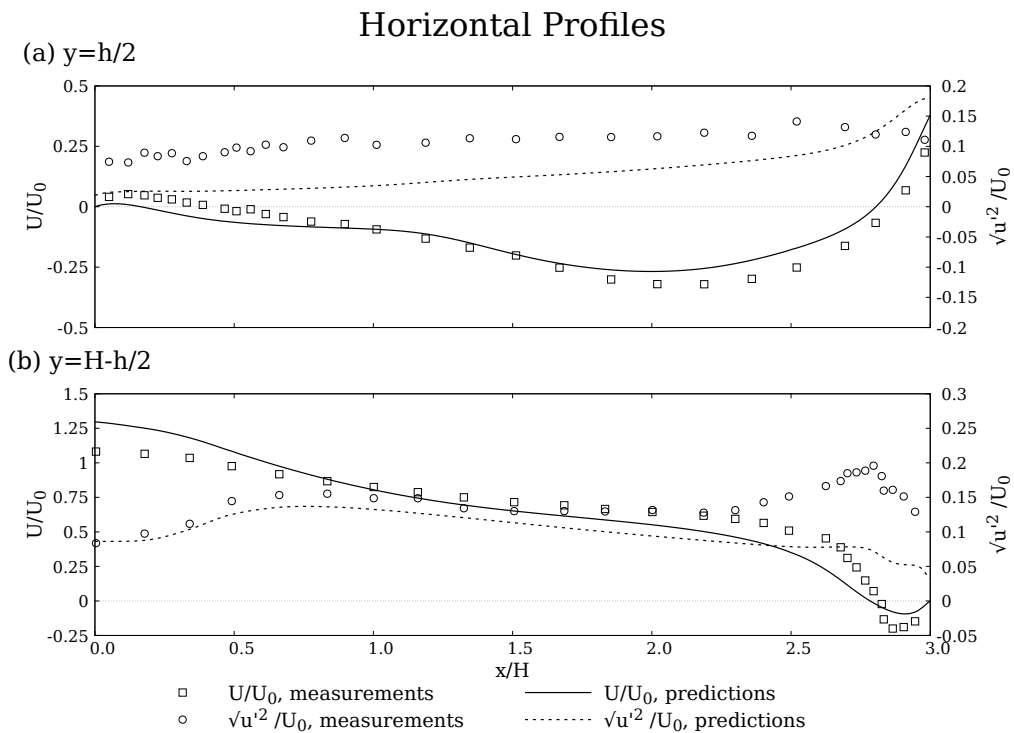


Figure 4.57 – Comparison between computed results for mean velocity (U/U_0) and RMS velocity ($\sqrt{u'^2}/U_0$) with experiment measurements performed by Nielsen [7] at $y = h/2$ and $y = H - h/2$ (symmetry plane).

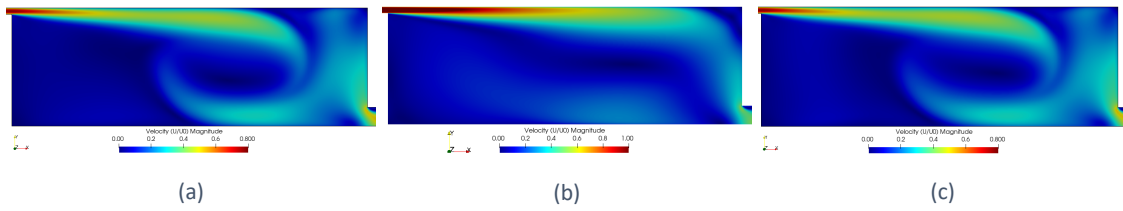


Figure 4.58 – Velocity distribution at the (a) and (c) near wall regions, and at the (b) symmetry plane.

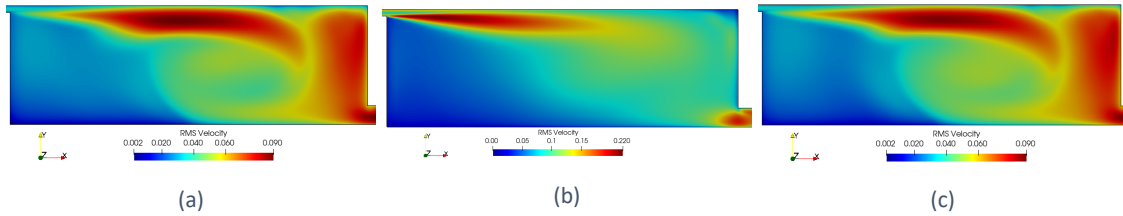


Figure 4.59 – RMS velocity ($\sqrt{u'^2}/U_0$) distribution at the near wall regions (a) and (c), and at the symmetry plane (b).

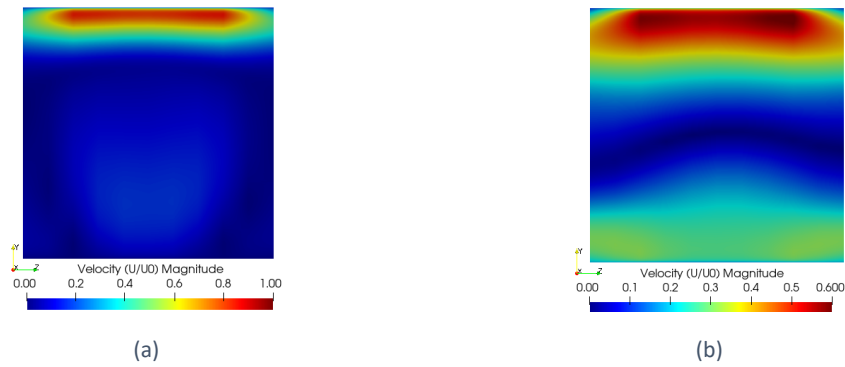


Figure 4.60 – Velocity predictions (U/U_0) at (a) $x = H$ and (b) $x = 2H$.

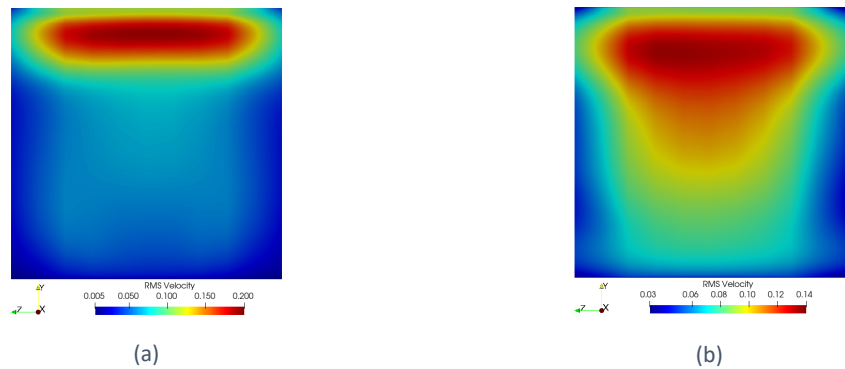


Figure 4.61 – RMS velocity predictions ($\sqrt{u'^2}/U_0$) at (a) $x = H$ and (b) $x = 2H$.

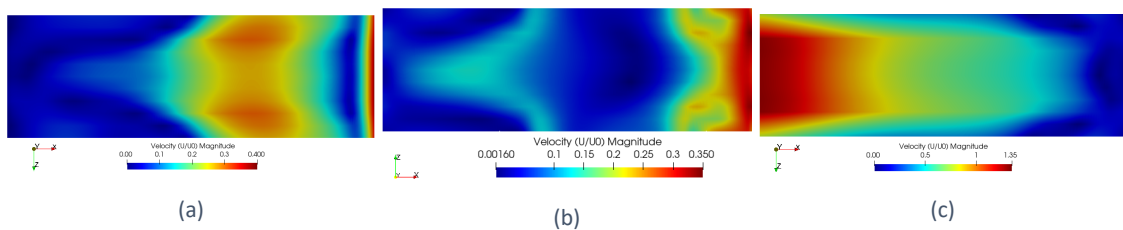


Figure 4.62 – Velocity predictions (U/U_0) at (a) $y = h/2$, (b) $y = 0.5H$ and (c) $y = H - h/2$.

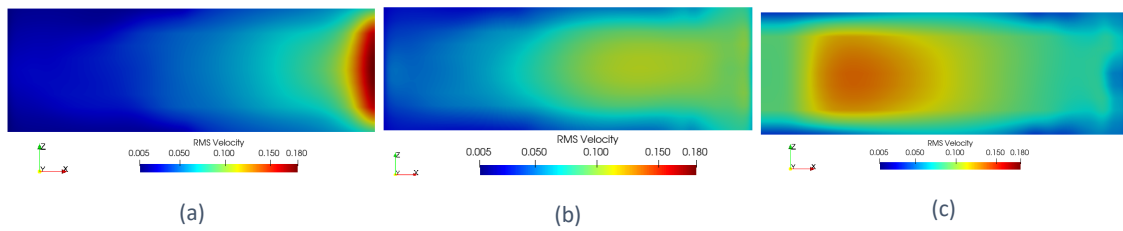


Figure 4.63 – RMS velocity predictions ($\sqrt{u'^2/U_0}$) at (a) $y = h/2$, (b) $y = 0.5H$ and (c) $y = H - h/2$.

4.4.4.2 Conclusions

The simulations of the 3D room of IEA Annex 20 allow to draw the following conclusions:

- 1°. The room presents symmetry of the results in the z –direction.
- 2°. Near the back and front walls, the jet deflects early from the ceiling.
- 3°. The results at the symmetry plane present lesser good agreement with the experimental data than the 2D predictions. However, this differences can not be fully justified by the change to a 3D simulation. This is also, probably the result of few number of cells (from the mesh study independence it is not possible to affirm that the results are completely mesh independent).

CONCLUSIONS AND FUTURE WORK

5.1 CONCLUSIONS

5.2 FUTURE WORK

5 CONCLUSIONS AND FUTURE WORK

5.1 Conclusions

The work presented in this dissertation was focused on the CFD simulations of airflow in indoor environments. The two main goals were the validation of turbulence models and the development of a CFD work-flow to study ventilation. The CFD software used was *OpenFOAM*.

From the chapter 1 it is possible to conclude that Reynolds-averaged Navier-Stokes (RaNS) models and large eddy simulation (LES) models are the most common ones. Whilst, direct numeric simulation models are often used for research purposes. RaNS models require less computational effort due to the fact that they average the variables values. This is also the reason why they are preferable when in comparison with LES, for most engineering problems.

In chapter 3 the governing equations are presented and assumptions often made were analysed. Some of these are, the concept of eddy viscosity, the Boussinesq approximation, turbulent flow near walls approach (law of the wall) and the Reynolds decomposition.

Boundary conditions and mesh quality are crucial in CFD simulations, since a simulation may not achieve convergence simply due to unfit meshes (high skewness and/or high aspect ratios). When it comes to boundary conditions, for some cases it is necessary to try several numerical possibilities and evaluate from experience or through experimental comparison, which ones to choose. This idea was reinforced by a simulation performed for the turbulent channel case presented in chapter 4.

The turbulence models studied in chapter 3 were the standard $k - \varepsilon$ model, the RNG $k - \varepsilon$ model, the realizable $k - \varepsilon$ model, the $\overline{v'^2} - f$ model, the $k - \omega$ model and the SST $k - \omega$ model.

In chapter 4 presents results for a 2D simple channel case and for the IEA Annex 20 2D benchmark. 3D simulations were also carried out for the IEA Annex 20 benchmark. The six RaNS turbulence models studied in 3 were tested and validated for indoor ventilation. The standard $k - \varepsilon$ model presented the most satisfactory results of all the studied turbulence models. The RNG model also showed good agreement with the experimental data, however it spends more time converging. The $k - \omega$ models results show poor agreement with the experimental data. These models predict a higher recirculation area than the $k - \varepsilon$ models.

The influence of temperature in the flow field was also studied, for different Reynolds and Archimedes numbers. Comparison between transient and steady-state solvers was made. Transient solvers prove to be more suitable.

Finally, it was possible to validate the work-flow process taken. Briefly the work-flow includes:

1. Define the physical problem and geometry;
2. Perform mesh convergence studies;
3. Choose physical and turbulence models;
4. Define boundary and initial conditions;
5. Select a solution method and adequate solver;
6. Run the case;
7. Post-processing.

5.2 Future Work

Although the work performed within this dissertation provides a good starting point, much work is yet to be developed.

1. 1st order upwind discretization schemes were used in the 2D simulations, investigations of 2nd order schemes is recommended;
2. Study of different types of meshes should be performed;
3. Comparison of the different turbulence models should be made for non-isothermal flows and for 3D simulations.
4. Further investigation of wall treatment and wall functions is recommended;
5. Comparative analysis of the wall functions and low Reynolds formulations.
6. Validation of the performance of compressible solvers, without the Boussinesq approximation, should be addressed.
7. Radiation models should be also look into.

BIBLIOGRAPHY AND OTHER SOURCES OF INFORMATION

6 BIBLIOGRAPHY AND OTHER SOURCES OF INFORMATION

- [1] S. Deck, F. Gand, V. Brunet, and S. Ben Khelil, “High-fidelity simulations of unsteady civil aircraft aerodynamics: stakes and perspectives. Application of zonal detached eddy simulation,” *Philosophical Transactions of the Royal Society A: Mathematical, Physical and Engineering Sciences*, vol. 372, no. 2022, p. 21, aug 2014. [Online]. Available: <https://royalsocietypublishing.org/doi/10.1098/rsta.2013.0325>
- [2] D. C. Wilcox, *Turbulence Modeling for CFD*. DCW Industries, Inc., 2006.
- [3] “All there is to know about different mesh types in CFD!” [Online]. Available: <https://www.manchestercfd.co.uk/post/all-there-is-to-know-about-different-mesh-types-in-cfd>
- [4] M. Bern and P. Plassmann, “Mesh Generation,” in *Handbook of Computational Geometry*, 1st ed., J.-R. Sack and J. Urrutia, Eds. Amsterdam: North-Holland, 2000, ch. 6, pp. 291–332. [Online]. Available: <https://www.sciencedirect.com/science/article/pii/B9780444825377500073>
- [5] P. V. Nielsen, F. Allard, H. B. Awbi, L. Davidson, and A. Schälin, *Computational Fluid Dynamics in Ventilation Design*. Brussels: Rehva, 2007.
- [6] A. D. Lemaire, Q. Chen, M. Ewert, J. Heikkinen, C. Hard, A. Moser, P. V. Nielsen, and G. Whittle, “Room Air and Contaminant Flow, Evaluation of Computational Methods Subtask-1 Summary Report,” International Energy Agency, Tech. Rep., 1993. [Online]. Available: https://www.iea-ebc.org/Data/publications/EBC_Annex_20_room_air_and.pdf
- [7] P. V. Nielsen, “Flow in air conditioned rooms,” PhD. Thesis, Technical University of Denmark, 1974. [Online]. Available: <https://vbn.aau.dk/da/publications/flow-in-air-conditioned-rooms-model-experiments-and-numerical-sol>
- [8] S. V. Patankar, *Numerical Heat Transfer and Fluid Flow*. CRC Press, oct 1980. [Online]. Available: <https://www.taylorfrancis.com/books/9781482234213>
- [9] T. van Hooff, B. Blocken, and G. J. F. van Heijst, “On the suitability of steady RANS CFD for forced mixing ventilation at transitional slot Reynolds

- numbers,” *Indoor Air*, vol. 23, no. 3, pp. 236–249, jun 2013. [Online]. Available: <http://doi.wiley.com/10.1111/ina.12010>
- [10] I. E. Agency, “Total final consumption (TFC) by sector, World 1990-2018,” 2021. [Online]. Available: <https://www.iea.org/data-and-statistics?country=WORLD&fuel=Energyconsumption&indicator=TFCShareBySector>
- [11] —, “Total consumption by end use – Residential, Portugal 2000-2018,” 2021. [Online]. Available: <https://www.iea.org/data-and-statistics?country=PORTUGAL&fuel=Energyconsumption&indicator=ResidentialConsByEndUse>
- [12] —, “Total consumption by end use – Services, Portugal 2005-2018,” 2021. [Online]. Available: <https://www.iea.org/data-and-statistics?country=PORTUGAL&fuel=Energyconsumption&indicator=ServicesConsByEndUse>
- [13] —, “Total final consumption (TFC) by sector, Portugal 1990-2018,” 2018. [Online]. Available: <https://www.iea.org/data-and-statistics?country=PORTUGAL&fuel=Energyconsumption&indicator=TFCShareBySector>
- [14] Y. Wang, Y. Cao, and X. Meng, “Energy efficiency of industrial buildings,” *Indoor and Built Environment*, vol. 28, no. 3, pp. 293–297, mar 2019. [Online]. Available: <http://journals.sagepub.com/doi/10.1177/1420326X19826192>
- [15] Y. Li and P. V. Nielsen, “CFD and ventilation research,” *Indoor Air*, vol. 21, no. 6, pp. 442–453, dec 2011. [Online]. Available: <http://doi.wiley.com/10.1111/j.1600-0668.2011.00723.x>
- [16] H. K. Versteeg and W. Malalasekera, *An Introduction to Computational Fluid Dynamics: The Finite Volume Method*, 2nd ed. Pearson Education, 2007.
- [17] B. Blocken, T. van Druenen, Y. Toparlar, F. Malizia, P. Mannion, T. Andrianne, T. Marchal, G.-J. Maas, and J. Diepens, “Aerodynamic drag in cycling pelotons: New insights by CFD simulation and wind tunnel testing,” *Journal of Wind Engineering and Industrial Aerodynamics*, vol. 179, pp. 319–337, aug 2018. [Online]. Available: <https://linkinghub.elsevier.com/retrieve/pii/S0167610518303751>
- [18] C. News, “Peloton Project: Largest-ever Sports Simulation Yields surprising Results - Empowering Engineers,” 2018. [Online]. Available: https://www.carhs.de/en/news/items/Peloton_Project_Largest-ever_Sports_Simulation_Yields_surprising_Results_8335.html
- [19] P. V. Nielsen, “Prediction of Air Flow and Comfort in Air Conditioned Spaces,” *ASHRAE Transactions*, vol. Vol. 81, no. Part II, pp. 247–259, 1975. [Online]. Available: <https://vbn.aau.dk/en/publications/prediction-of-air-flow-and-comfort-in-air-conditioned-spaces>
- [20] —, “Specification of a Two-Dimensional Test Case (IEA),” Institut for Bygningsteknik, Aalborg Universitet, Tech. Rep., 1990.

- [Online]. Available: https://vbn.aau.dk/ws/portalfiles/portal/197503356/Specification_of_a_TwoDimensional_Test_Case.pdf
- [21] —, “Moisture Transfer in Air Conditioned Rooms and Cold Stores,” in *Introduction to the Second International Symposium on Moisture Problems in Buildings*. Rotterdam, Netherlands: Aalborg Universitet, 1974, pp. 1–9. [Online]. Available: <https://vbn.aau.dk/en/publications/moisture-transfer-in-air-conditioned-rooms-and-cold-stores>
- [22] P. J. Jones and G. E. Whittle, “Computational fluid dynamics for building air flow prediction-current status and capabilities,” *Building and Environment*, vol. 27, no. 3, pp. 321–338, jul 1992.
- [23] M. Russell and P. Surendran, “Use of computational fluid dynamics to aid studies of room air distribution: A review of some recent work,” *Building Services Engineering Research and Technology*, vol. 21, no. 4, pp. 241–247, nov 2000. [Online]. Available: <http://journals.sagepub.com/doi/10.1177/014362440002100405>
- [24] K. Ito, K. Inthavong, T. Kurabuchi, T. Ueda, T. Endo, T. Omori, H. Ono, S. Kato, K. Sakai, Y. Suwa, H. Matsumoto, H. Yoshino, W. Zhang, and J. Tu, “CFD Benchmark Tests for Indoor Environmental Problems: Part 3 Numerical Thermal Manikins,” *International Journal of Architectural Engineering Technology*, vol. 2, no. 1, pp. 50–75, apr 2015. [Online]. Available: <http://www.avantipublishers.com/downloads/ijaetv2n1a3/>
- [25] A. Baskaran and A. Kashef, “Investigation of air flow around buildings using computational fluid dynamics techniques,” *Engineering Structures*, vol. 18, no. 11, pp. 861–873, nov 1996.
- [26] P. Blondeau, M. Spérandio, and F. Allard, “Night ventilation for building cooling in summer,” *Solar Energy*, vol. 61, no. 5, pp. 327–335, nov 1997.
- [27] D. N. Sørensen and P. V. Nielsen, “Quality control of computational fluid dynamics in indoor environments,” *Indoor Air*, vol. 13, no. 1, pp. 2–17, mar 2003. [Online]. Available: <http://doi.wiley.com/10.1111/j.1600-0668.2003.00170.x>
- [28] K. Goethals and A. Janssens, “Turbulent mixed convection in an enclosure with different inlet and outlet configurations,” in *10th REHVA World Congress: Sustainable energy use in buildings*. (Clima 2010), 2010.
- [29] P. V. Nielsen, L. Rong, and I. O. Cortes, “The IEA Annex 20 two-dimensional benchmark test for CFD predictions,” in *Clima 2010: 10th Rehva World Congress: Sustainable Energy Use in Buildings*. Antalya, Turkey: Clima 2010: 10th Rehva World Congress, 2010.
- [30] T. van Hooff and B. Blocken, “Low-Reynolds number mixing ventilation flows: Impact of physical and numerical diffusion on flow and dispersion,” *Building*

- Simulation*, vol. 10, no. 4, pp. 589–606, aug 2017. [Online]. Available: <http://link.springer.com/10.1007/s12273-017-0354-3>
- [31] T. van Hooff, B. Blocken, and Y. Tominaga, “On the accuracy of CFD simulations of cross-ventilation flows for a generic isolated building: Comparison of RANS, LES and experiments,” *Building and Environment*, vol. 114, pp. 148–165, mar 2017.
- [32] P. Heiselberg, Y. Li, A. Andersen, M. Bjerre, and Z. Chen, “Experimental and CFD evidence of multiple solutions in a naturally ventilated building,” *Indoor Air*, vol. 14, no. 1, pp. 43–54, feb 2004. [Online]. Available: <http://doi.wiley.com/10.1046/j.1600-0668.2003.00209.x>
- [33] G. Evola and V. Popov, “Computational analysis of wind driven natural ventilation in buildings,” *Energy and Buildings*, vol. 38, no. 5, pp. 491–501, may 2006. [Online]. Available: <https://linkinghub.elsevier.com/retrieve/pii/S0378778805001702>
- [34] Z. Sun and S. Wang, “A CFD-based test method for control of indoor environment and space ventilation,” *Building and Environment*, vol. 45, no. 6, pp. 1441–1447, jun 2010. [Online]. Available: <https://linkinghub.elsevier.com/retrieve/pii/S0360132309003606>
- [35] Z. J. Zhai, M. E. Mankibi, and A. Zoubir, “Review of Natural Ventilation Models,” *Energy Procedia*, vol. 78, pp. 2700–2705, nov 2015. [Online]. Available: <https://linkinghub.elsevier.com/retrieve/pii/S1876610215020871>
- [36] S.-W. Hong, V. Exadaktylos, I.-B. Lee, T. Amon, A. Youssef, T. Norton, and D. Berckmans, “Validation of an open source CFD code to simulate natural ventilation for agricultural buildings,” *Computers and Electronics in Agriculture*, vol. 138, pp. 80–91, jun 2017. [Online]. Available: <https://linkinghub.elsevier.com/retrieve/pii/S016816991630535X>
- [37] J. Cheng, D. Qi, A. Katal, L. L. Wang, and T. Stathopoulos, “Evaluating wind-driven natural ventilation potential for early building design,” *Journal of Wind Engineering and Industrial Aerodynamics*, vol. 182, pp. 160–169, nov 2018. [Online]. Available: <https://linkinghub.elsevier.com/retrieve/pii/S0167610518303027>
- [38] A. Khosronejad, C. Santoni, K. Flora, Z. Zhang, S. Kang, S. Payabvash, and F. Sotiropoulos, “Fluid dynamics simulations show that facial masks can suppress the spread of COVID-19 in indoor environments,” *AIP Advances*, vol. 10, no. 12, p. 125109, dec 2020. [Online]. Available: <http://aip.scitation.org/doi/10.1063/5.0035414>
- [39] S. Bhattacharyya, K. Dey, A. R. Paul, and R. Biswas, “A novel CFD analysis to minimize the spread of COVID-19 virus in hospital isolation room,” *Chaos, Solitons & Fractals*, vol. 139, p. 110294, oct 2020. [Online]. Available: <https://linkinghub.elsevier.com/retrieve/pii/S0960077920306901>

- [40] K. Ito, K. Inthavong, T. Kurabuchi, T. Ueda, T. Endo, T. Omori, H. Ono, S. Kato, K. Sakai, Y. Suwa, H. Matsumoto, H. Yoshino, W. Zhang, and J. Tu, "CFD Benchmark Tests for Indoor Environmental Problems: Part 1 Isothermal/Non-Isothermal Flow in 2D and 3D Room Model," *International Journal of Architectural Engineering Technology*, vol. 2, no. 1, pp. 01–22, apr 2015. [Online]. Available: <http://www.avantipublishers.com/downloads/ijaetv2n1a1/>
- [41] K. Ito, K. Inthavong, T. Kurabuchi, T. Ueda, T. Endo, T. Omori, H. Ono, S. Kato, K. Sakai, Y. S. Yoshihide Suwa, M. Matsumoto, H. Yoshino, W. Zhang, and J. Tu, "CFD Benchmark Tests for Indoor Environmental Problems: Part 2 Cross-Ventilation Airflows and Floor Heating Systems," *International Journal of Architectural Engineering Technology*, vol. 2, no. 1, pp. 23–49, apr 2015. [Online]. Available: <http://www.avantipublishers.com/downloads/ijaetv2n1a2/>
- [42] T. B. Gatski, M. Y. Hussaini, and J. L. Lumley, *Simulation and Modeling of Turbulent Flows*. Oxford University Press Inc, 1998.
- [43] P. A. Durbin and G. Medic, *Fluid Dynamics with a Computational Perspective*, 1st ed. United States of America: Cambridge University Press, 2007.
- [44] G. Alfonsi, "On Direct Numerical Simulation of Turbulent Flows," *Applied Mechanics Reviews*, vol. 64, no. 2, 2011.
- [45] H. Abe, H. Kawamura, and Y. Matsuo, "Direct Numerical Simulation of a Fully Developed Turbulent Channel Flow With Respect to the Reynolds Number Dependence," *Journal of Fluids Engineering*, vol. 123, no. 2, pp. 382–393, jun 2001. [Online]. Available: <https://asmedigitalcollection.asme.org/fluidsengineering/article/123/2/382/463150/Direct-Numerical-Simulation-of-a-Fully-Developed>
- [46] P. Schlatter and R. Örlü, "Assessment of direct numerical simulation data of turbulent boundary layers," *Journal of Fluid Mechanics*, vol. 659, pp. 116–126, sep 2010. [Online]. Available: https://www.cambridge.org/core/product/identifier/S0022112010003113/type/journal_article
- [47] P. Moin and K. Mahesh, "DIRECT NUMERICAL SIMULATION: A Tool in Turbulence Research," *Annual Review of Fluid Mechanics*, vol. 30, no. 1, pp. 539–578, 1998.
- [48] M. Perić and J. H. Ferziger, *Computational Methods for Fluid Dynamics*, 3rd ed. Berlin, Heidelberg: Springer-Verlag, 2002.
- [49] M. Lee and R. D. Moser, "Direct numerical simulation of turbulent channel flow up to $Re_{\tau} \approx 5200$," *Journal of Fluid Mechanics*, vol. 774, pp. 395–415, jun 2015. [Online]. Available: https://www.cambridge.org/core/journals/journal-of-fluid-mechanics/article/abs/direct-numerical-simulation-of-turbulent-channel-flow-up-to_mathitrittauapprox-5200/3AE84A5A48F83AF294F6CB042AF92DA8

- [50] S. B. Pope, *Turbulent Flows*, illustrate ed., C. U. Press, Ed. Cambridge University Press, 2000, 2000.
- [51] X. Wu and P. Moin, "A direct numerical simulation study on the mean velocity characteristics in turbulent pipe flow," *Journal of Fluid Mechanics*, vol. 608, pp. 81–112, aug 2008. [Online]. Available: https://www.cambridge.org/core/product/identifier/S0022112008002085/type/journal_article
- [52] H. Le, J. Kim, and P. Moin, "Direct Numerical Simulation of Turbulent Flow over a Backward-Facing Step," *Article in Journal of Fluid Mechanics*, vol. 330, pp. 349–374, 1997. [Online]. Available: <https://www.researchgate.net/publication/259359559>
- [53] H. Hattori and Y. Nagano, "Direct numerical simulation of turbulent heat transfer in plane impinging jet," *International Journal of Heat and Fluid Flow*, vol. 25, no. 5, pp. 749–758, oct 2004.
- [54] X. Chu, G. Yang, S. Pandey, and B. Weigand, "Direct numerical simulation of convective heat transfer in porous media," *International Journal of Heat and Mass Transfer*, vol. 133, pp. 11–20, apr 2019.
- [55] K. Mahesh, G. Constantinescu, and P. Moin, "A numerical method for large-eddy simulation in complex geometries," *Journal of Computational Physics*, vol. 197, no. 1, pp. 215–240, jun 2004. [Online]. Available: <https://linkinghub.elsevier.com/retrieve/pii/S0021999103006272>
- [56] R. O. Fox, *Computational Models for Turbulent Reacting Flows*, 1st ed. Cambridge University Press, 2003.
- [57] A. Kubilay, D. Derome, and J. Carmeliet, "Analysis of time-resolved wind-driven rain on an array of low-rise cubic buildings using large eddy simulation and an Eulerian multiphase model," *Building and Environment*, vol. 114, pp. 68–81, mar 2017. [Online]. Available: <https://linkinghub.elsevier.com/retrieve/pii/S0360132316304838>
- [58] Y. Yu, Y. Yang, and Z. Xie, "A new inflow turbulence generator for large eddy simulation evaluation of wind effects on a standard high-rise building," *Building and Environment*, vol. 138, pp. 300–313, jun 2018. [Online]. Available: <https://linkinghub.elsevier.com/retrieve/pii/S036013231830194X>
- [59] M. Kurppa, A. Hellsten, M. Auvinen, S. Raasch, T. Vesala, and L. Järvi, "Ventilation and Air Quality in City Blocks Using Large-Eddy Simulation—Urban Planning Perspective," *Atmosphere*, vol. 9, no. 2, p. 65, feb 2018. [Online]. Available: <http://www.mdpi.com/2073-4433/9/2/65>
- [60] Q. Malé, G. Staffelbach, O. Vermorel, A. Misdariis, F. Ravet, and T. Poinso, "Large Eddy Simulation of Pre-Chamber Ignition in an Internal Combustion Engine," *Flow, Turbulence and Combustion*, vol. 103, no. 2, pp. 465–483, aug 2019. [Online]. Available: <http://link.springer.com/10.1007/s10494-019-00026-y>

- [61] S. B. Pope, "Ten questions concerning the large-eddy simulation of turbulent flows," *New Journal of Physics*, vol. 6, pp. 35–35, mar 2004. [Online]. Available: <https://iopscience.iop.org/article/10.1088/1367-2630/6/1/035>
- [62] Y. Zhiyin, "Large-eddy simulation: Past, present and the future," *Chinese Journal of Aeronautics*, vol. 28, no. 1, pp. 11–24, feb 2015. [Online]. Available: <https://linkinghub.elsevier.com/retrieve/pii/S1000936114002064>
- [63] S. T. Bose and G. I. Park, "Wall-Modeled Large-Eddy Simulation for Complex Turbulent Flows," *Annual Review of Fluid Mechanics*, vol. 50, no. 1, pp. 535–561, jan 2018. [Online]. Available: <http://www.annualreviews.org/doi/10.1146/annurev-fluid-122316-045241>
- [64] P. Spalart, W. Jou, M. Strelets, and S. Allmaras, "Advances in DNS/LES," in *Proceedings of the First AFOSR International Conference on DNS/LES*, C. Liu and Z. Liu, Eds. Louisiana: Greyden Press, Columbus, 1997, pp. 137–147. [Online]. Available: <http://www.cobaltcfd.com/pdfs/DES97.pdf>
- [65] M. Shur, P. Spalart, M. Strelets, and A. Travin, "Detached-eddy simulation of an airfoil at high angle of attack," in *Engineering Turbulence Modelling and Experiments 4*. Elsevier, 1999, pp. 669–678.
- [66] P. R. Spalart, "Detached-Eddy Simulation," *Annual Review of Fluid Mechanics*, vol. 41, no. 1, pp. 181–202, jan 2009. [Online]. Available: <http://www.annualreviews.org/doi/10.1146/annurev.fluid.010908.165130>
- [67] F. Grossi, M. Braza, and Y. Hoarau, "Prediction of Transonic Buffet by Delayed Detached-Eddy Simulation," *AIAA Journal*, vol. 52, no. 10, pp. 2300–2312, oct 2014. [Online]. Available: <https://arc.aiaa.org/doi/10.2514/1.J052873>
- [68] Y. Zhang, W. G. Habashi, and R. A. Khurram, "Zonal Detached-Eddy Simulation of Turbulent Unsteady Flow over Iced Airfoils," *Journal of Aircraft*, vol. 53, no. 1, pp. 168–181, jan 2016. [Online]. Available: <https://arc.aiaa.org/doi/10.2514/1.C033253>
- [69] Y. Jin, F. Liao, and J. Cai, "Numerical Simulation of 30P30N Multi-Element Airfoil Using Delayed Detached-Eddy Simulation," in *AIAA AVIATION 2020 FORUM*. Reston, Virginia: American Institute of Aeronautics and Astronautics, jun 2020. [Online]. Available: <https://arc.aiaa.org/doi/10.2514/6.2020-2556>
- [70] N. Chauvet, S. Deck, and L. Jacquin, "Zonal Detached Eddy Simulation of a Controlled Propulsive Jet," *AIAA Journal*, vol. 45, no. 10, pp. 2458–2473, oct 2007. [Online]. Available: <https://arc.aiaa.org/doi/10.2514/1.28562>
- [71] K. Kakosimos and M. Assael, "Application of Detached Eddy Simulation to neighbourhood scale gases atmospheric dispersion modelling," *Journal of Hazardous Materials*, vol. 261, pp. 653–668, oct 2013. [Online]. Available: <https://linkinghub.elsevier.com/retrieve/pii/S0304389413005840>

- [72] S. Deck, "Zonal-Detached-Eddy Simulation of the Flow Around a High-Lift Configuration," *AIAA Journal*, vol. 43, no. 11, pp. 2372–2384, nov 2005. [Online]. Available: <https://arc.aiaa.org/doi/10.2514/1.16810>
- [73] A. Uzun and M. Yousuff Hussaini, "An application of delayed detached eddy simulation to tandem cylinder flow field prediction," *Computers & Fluids*, vol. 60, pp. 71–85, may 2012. [Online]. Available: <https://linkinghub.elsevier.com/retrieve/pii/S0045793012000850>
- [74] Z. Xiao, J. Liu, K. Luo, J. Huang, and S. Fu, "Investigation of Flows Around a Rudimentary Landing Gear with Advanced Detached-Eddy-Simulation Approaches," *AIAA Journal*, vol. 51, no. 1, pp. 107–125, jan 2013. [Online]. Available: <https://arc.aiaa.org/doi/10.2514/1.J051598>
- [75] V. B. Ananthan, P. Bernicke, and R. A. D. Akkermans, "Aeroacoustic Analysis of a Circulation-Controlled High-Lift Flap by Zonal Overset Large-Eddy Simulation," *AIAA Journal*, vol. 58, no. 12, pp. 5294–5305, dec 2020. [Online]. Available: <https://arc.aiaa.org/doi/10.2514/1.J059056>
- [76] P. Wang and Y. Liu, "Influence of diametral acoustic mode on cavity flow dynamics: Zonal large eddy simulation and proper orthogonal decomposition," *Physics of Fluids*, vol. 32, no. 7, pp. 075 103–1;075 103–21, jul 2020. [Online]. Available: <http://aip.scitation.org/doi/10.1063/5.0012640>
- [77] G. Chen, X.-F. Liang, D. Zhou, X.-B. Li, and F.-s. Lien, "Numerical study of flow and noise predictions for tandem cylinders using incompressible improved delayed detached eddy simulation combined with acoustic perturbation equations," *Ocean Engineering*, vol. 224, p. 108740, mar 2021. [Online]. Available: <https://linkinghub.elsevier.com/retrieve/pii/S002980182100175X>
- [78] A. Sharma, H. Mittal, and A. Gairola, "Detached-eddy simulation of interference between buildings in tandem arrangement," *Journal of Building Engineering*, vol. 21, pp. 129–140, 2019.
- [79] A. Straatman and R. Martinuzzi, "A STUDY ON THE SUPPRESSION OF VORTEX SHEDDING FROM A SQUARE CYLINDER NEAR A WALL," in *Engineering Turbulence Modelling and Experiments 5*, W. Rodi and N. Fueyo, Eds. Elsevier Science Ltd. All rights reserved., 2002, pp. 403–411. [Online]. Available: <https://linkinghub.elsevier.com/retrieve/pii/B9780080441146500387>
- [80] A. Demuren and H. Grotjans, "Buoyancy-Driven Flows—Beyond the Boussinesq Approximation," *Numerical Heat Transfer, Part B: Fundamentals*, vol. 56, no. 1, pp. 1–22, jun 2009. [Online]. Available: <http://www.tandfonline.com/doi/abs/10.1080/10407790902970080>
- [81] K. Suga and K. Abe, "Nonlinear eddy viscosity modelling for turbulence and heat transfer near wall and shear-free boundaries," *International Journal of*

- Heat and Fluid Flow*, vol. 21, no. 1, pp. 37–48, feb 2000. [Online]. Available: <https://linkinghub.elsevier.com/retrieve/pii/S0142727X99000600>
- [82] W. Bauer, O. Haag, and D. Hennecke, “Accuracy and robustness of nonlinear eddy viscosity models,” *International Journal of Heat and Fluid Flow*, vol. 21, no. 3, pp. 312–319, jun 2000. [Online]. Available: <https://linkinghub.elsevier.com/retrieve/pii/S0142727X00000151>
- [83] Q. Chen and J. Srebric, “A Procedure for Verification, Validation, and Reporting of Indoor Environment CFD Analyses,” *HVAC&R Research*, vol. 8, no. 2, pp. 201–216, apr 2002. [Online]. Available: <http://www.tandfonline.com/doi/abs/10.1080/10789669.2002.10391437>
- [84] A. Kolmogorov, “Equations of turbulent motion of an incompressible fluid,” *Physics, Izv Akad Nauk SSR*, vol. 6, no. 1, p. 2, 1942.
- [85] P. G. Saffman, “A model for inhomogeneous turbulent flow,” *Proceedings of the Royal Society of London. A. Mathematical and Physical Sciences*, vol. 317, no. 1530, pp. 417–433, jun 1970. [Online]. Available: <https://royalsocietypublishing.org/doi/10.1098/rspa.1970.0125>
- [86] D. C. Wilcox, “Reassessment of the scale-determining equation for advanced turbulence models,” *AIAA Journal*, vol. 26, no. 11, pp. 1299–1310, nov 1988. [Online]. Available: <https://arc.aiaa.org/doi/10.2514/3.10041>
- [87] D. Wilcox, *Turbulence modeling for CFD*, 2nd ed. DCW industries La Canada, CA, 1998, vol. 2.
- [88] F. R. Menter, “Influence of freestream values on k-omega turbulence model predictions,” *AIAA Journal*, vol. 30, no. 6, pp. 1657–1659, jun 1992. [Online]. Available: <https://arc.aiaa.org/doi/10.2514/3.11115>
- [89] F. Menter, “Zonal Two Equation k- ω Turbulence Models For Aerodynamic Flows,” in *23rd Fluid Dynamics, Plasmadynamics, and Lasers Conference*. Reston, Virginia: American Institute of Aeronautics and Astronautics, 1993.
- [90] J. C. Kok and S. Spekreijse, “Efficient and accurate Implementation of the k-omega turbulence model in the NLR multi-block Navier-Stokes system,” National Aerospace Laboratory NLR, Tech. Rep., 2000. [Online]. Available: <https://reports.nlr.nl/bitstream/handle/10921/822/TP-2000-144.pdf?sequence=1>
- [91] R. Morgans, B. Dally, G. Nathan, P. Lanspeary, and D. Fletcher, “Application of the revised Wilcox (1998) k-omega turbulence model to a jet in co-flow,” in *Second international conference on CFD in the Mineral and process industries*, Melbourne, Australia, 1999. [Online]. Available: https://www.cfd.com.au/cfd_conf99/Conf99_Papers/068MORG.PDF

- [92] J. C. Kok, "Resolving the dependence on free-stream values for the k - ω turbulence model," *AIAA journal*, vol. 38, no. 7, pp. 1292–1295, 2000. [Online]. Available: <https://reports.nlr.nl/xmlui/bitstream/handle/10921/1141/TP-1999-295.pdf?sequence=1&isAllowed=y>
- [93] A. Hellsten, "Some improvements in Menter's k - ω SST turbulence model," in *29th AIAA Fluid Dynamics Conference*. Albuquerque: American Institute of Aeronautics and Astronautics Inc., 1998, pp. 1–11.
- [94] F. R. Menter, M. Kuntz, and R. Langtry, "Ten Years of Industrial Experience with the SST Turbulence Model," *Turbulence, Heat and Mass Transfer*, vol. 4, no. July 2014, pp. 625–632, 2003. [Online]. Available: https://cfd.spbstu.ru/agarbaruk/doc/2003_Menter,Kuntz,Langtry_TenyearsofindustrialexperiencewiththeSSTturbulencemodel.pdf
- [95] P. Y. Chou, "ON VELOCITY CORRELATIONS AND THE SOLUTIONS OF THE EQUATIONS OF TURBULENT FLUCTUATION," *Quarterly of Applied Mathematics*, vol. 3, no. 1, pp. 38–54, 1945. [Online]. Available: <https://www.ams.org/journals/qam/1945-03-01/S0033-569X-1945-11999-0/S0033-569X-1945-11999-0.pdf>
- [96] W. Jones and B. Launder, "The prediction of laminarization with a two-equation model of turbulence," *International Journal of Heat and Mass Transfer*, vol. 15, no. 2, pp. 301–314, feb 1972. [Online]. Available: <https://linkinghub.elsevier.com/retrieve/pii/0017931072900762>
- [97] B. Launder and D. Spalding, "The Numerical Computation of Turbulent Flows," in *Numerical Prediction of Flow, Heat Transfer, Turbulence and Combustion*. Elsevier, 1974, ch. Paper 8, pp. 96–116.
- [98] T.-H. Shih, W. W. Liou, A. Shabbir, Z. Yang, and J. Zhu, "A New k - ϵ Eddy Viscosity Model for High Reynolds Number Turbulent Flows: Model Development and Validation," NASA Lewis Research Center, Cleveland, OH, United States, Tech. Rep., 1994.
- [99] V. Yakhot and S. A. Orszag, "Renormalization group analysis of turbulence. I. Basic theory," *Journal of Scientific Computing*, vol. 1, no. 1, pp. 3–51, 1986.
- [100] V. Yakhot, S. A. Orszag, S. Thangam, T. B. Gatski, and C. G. Speziale, "Development of turbulence models for shear flows by a double expansion technique," *Physics of Fluids A: Fluid Dynamics*, vol. 4, no. 7, pp. 1510–1520, 1992.
- [101] K. Hafez, O. Elsamni, and K. Zakaria, "Numerical investigation of the fully developed turbulent flow over a moving wavy wall using k - ϵ turbulence model," *Alexandria Engineering Journal*, vol. 50, no. 2, pp. 145–162, jun 2011. [Online]. Available: <https://linkinghub.elsevier.com/retrieve/pii/S1110016811000354>
- [102] N. Viti, D. Valero, and C. Gualtieri, "Numerical Simulation of Hydraulic Jumps. Part 2: Recent Results and Future Outlook," *Water*, vol. 11, no. 1, p. 28, dec 2018. [Online]. Available: <http://www.mdpi.com/2073-4441/11/1/28>

- [103] Z. J. Zhai, Z. Zhang, W. Zhang, and Q. Y. Chen, "Evaluation of Various Turbulence Models in Predicting Airflow and Turbulence in Enclosed Environments by CFD: Part 1—Summary of Prevalent Turbulence Models," *HVAC&R Research*, vol. 13, no. 6, pp. 853–870, nov 2007. [Online]. Available: <http://www.tandfonline.com/doi/abs/10.1080/10789669.2007.10391459>
- [104] P. V. Nielsen, "Fifty years of CFD for room air distribution," *Building and Environment*, vol. 91, pp. 78–90, sep 2015. [Online]. Available: <https://linkinghub.elsevier.com/retrieve/pii/S036013231500092X>
- [105] T. H. Shih, W. W. Liou, A. Shabbir, Z. Yang, and J. Zhu, "A new $k-\epsilon$ eddy viscosity model for high reynolds number turbulent flows," *Computers & Fluids*, vol. 24, no. 3, pp. 227–238, 1995.
- [106] Z. Qian, X. Hu, W. Huai, and A. Amador, "Numerical simulation and analysis of water flow over stepped spillways," *Science in China Series E: Technological Sciences*, vol. 52, no. 7, pp. 1958–1965, jul 2009. [Online]. Available: <http://link.springer.com/10.1007/s11431-009-0127-z>
- [107] M. Bulat and P. Bulat, "Comparison of Turbulence Models in the Calculation of Supersonic Separated Flows," *World Applied Sciences Journal*, vol. 27, pp. 1263–1266, 2013.
- [108] T.-H. Shih, J.-Y. Chen, and J. L. Lumley, "Second order modeling of boundary-free turbulent shear flows," *AIAA Journal*, vol. 30, no. 6, pp. 1553–1560, jun 1992. [Online]. Available: <https://arc.aiaa.org/doi/10.2514/3.11100>
- [109] B. L. Mount and M. L. de Bertodano, "Three-Dimensional Nonisotropic Porous-Medium Realizable $k-\epsilon$ CFD Model for a Jet," *Nuclear Technology*, vol. 171, no. 2, pp. 161–170, aug 2010. [Online]. Available: <https://www.tandfonline.com/doi/full/10.13182/NT10-A10781>
- [110] H. Chen and B. Moshfegh, "Comparing $k-\epsilon$ models on predictions of an impinging jet for ventilation of an office room," *The 12th International Conference on Air Distribution in Rooms, Trondheim, Norway June 19-22, 2011*, 2011. [Online]. Available: <https://www.researchgate.net/publication/267249036>
- [111] M. d. A. Maria Odete, "The effect of the wall downstream on air curtain sealing efficiency," Master's Thesis, Eindhoven University of Technology, 2017. [Online]. Available: <https://research.tue.nl/en/studentTheses/the-effect-of-the-wall-downstream-on-air-curtain-sealing-efficien>
- [112] M. Noor, A. P. Wandel, and T. Yusaf, "Analysis of Recirculation Zone and Ignition Position of Non-Premixed Bluff-Body for Biogas MILD Combustion," *International Journal of Automotive and Mechanical Engineering*, vol. 8, pp. 1176–1186, dec 2013. [Online]. Available: http://ijame.ump.edu.my/images/Volume_{ }8/8_{ }Nooretal.pdf

- [113] Y. Lee and C. Kim, "A STUDY ON THE IMPROVEMENT OF k - ϵ TURBULENCE MODEL FOR PREDICTION OF THE RECIRCULATION FLOW," *Journal of computational fluids engineering*, vol. 21, no. 2, pp. 12–24, jun 2016. [Online]. Available: <http://koreascience.or.kr/journal/view.jsp?kj=JSRCB3&py=2016&vnc=v21n2&sp=12>
- [114] J. Fan, C. Yan, P. Lei, C. Wang, and G. Liu, "Study on Flow Characteristics of Three-Dimensional Backward-Facing Step at High Reynolds," *Journal of Coastal Research*, vol. 106, no. sp1, pp. 522–525, 2020. [Online]. Available: <https://doi.org/10.2112/SI106-118.1>
- [115] P. V. Nielsen, C. Zhang, L. A. Bugenings, and M. Schaffer, "The Development of a Benchmark for Room Air Distribution: the backward facing step flow," in *15th ROOMVENT Virtual Conference, 2021*. Aalborg: Energy efficient ventilation for healthy future buildings, 2021. [Online]. Available: <https://vbn.aau.dk/en/publications/the-development-of-a-benchmark-for-room-air-distribution-the-back>
- [116] R. Shaheed, A. Mohammadian, and H. Kheirkhah Gildeh, "A comparison of standard k - ϵ and realizable k - ϵ turbulence models in curved and confluent channels," *Environmental Fluid Mechanics*, vol. 19, no. 2, pp. 543–568, apr 2019. [Online]. Available: <http://link.springer.com/10.1007/s10652-018-9637-1>
- [117] A. Secchiaroli, R. Ricci, S. Montelpare, and V. D'Alessandro, "Numerical simulation of turbulent flow in a Ranque-Hilsch vortex tube," *International Journal of Heat and Mass Transfer*, no. 23-24, pp. 5496–5511. [Online]. Available: https://www.researchgate.net/publication/40822232_Numerical_Simulation_of_Confined_Vortex_Flow_Using_a_Modified_k-epsilon_Turbulence_Model, volume={52},year={2009}
- [118] A. M. Jawarneh, H. Tlilan, A. Al-Shyyab, and A. Ababneh, "Strongly swirling flows in a cylindrical separator," *Minerals Engineering*, vol. 21, no. 5, pp. 366–372, apr 2008. [Online]. Available: <https://linkinghub.elsevier.com/retrieve/pii/S0892687507002920>
- [119] C. G. Speziale, T. B. Gatski, and N. Fitzmaurice, "An analysis of RNG-based turbulence models for homogeneous shear flow," *Physics of Fluids A: Fluid Dynamics*, vol. 3, no. 9, pp. 2278–2281, sep 1991. [Online]. Available: <http://aip.scitation.org/doi/10.1063/1.857963>
- [120] J. Papp and K. Ghia, "Application of the RNG turbulence model to the simulation of axisymmetric supersonic separated base flows," in *39th Aerospace Sciences Meeting and Exhibit*. Reston, Virginia: American Institute of Aeronautics and Astronautics, jan 2001. [Online]. Available: <https://arc.aiaa.org/doi/10.2514/6.2001-727>

- [121] Z. Han and R. D. Reitz, "Turbulence Modeling of Internal Combustion Engines Using RNG $k-\epsilon$ Models," *Combustion Science and Technology*, vol. 106, no. 4-6, pp. 267–295, jan 1995. [Online]. Available: <http://www.tandfonline.com/doi/abs/10.1080/00102209508907782>
- [122] F. Wang, R. D. Reitz, C. Pera, Z. Wang, and J. Wang, "Application of Generalized RNG Turbulence Model to Flow in Motored Single-Cylinder PFI Engine," *Engineering Applications of Computational Fluid Mechanics*, vol. 7, no. 4, pp. 486–495, jan 2013. [Online]. Available: <http://www.tandfonline.com/doi/abs/10.1080/19942060.2013.11015487>
- [123] V. Krastev, L. Silvestri, and G. Falcucci, "A Modified Version of the RNG $k-\epsilon$ Turbulence Model for the Scale-Resolving Simulation of Internal Combustion Engines," *Energies*, vol. 10, no. 12, p. 2116, dec 2017. [Online]. Available: <http://www.mdpi.com/1996-1073/10/12/2116>
- [124] J. Kim, "A numerical study of the effects of ambient wind direction on flow and dispersion in urban street canyons using the RNG k -Epsilon turbulence model," *Atmospheric Environment*, vol. 38, no. 19, pp. 3039–3048, jun 2004. [Online]. Available: <https://linkinghub.elsevier.com/retrieve/pii/S1352231004001773>
- [125] J. Y. Wang and X. J. Hu, "Application of RNG $k-\epsilon$ Turbulence Model on Numerical Simulation in Vehicle External Flow Field," *Applied Mechanics and Materials*, vol. 170-173, pp. 3324–3328, may 2012. [Online]. Available: <https://www.scientific.net/AMM.170-173.3324>
- [126] T. Bartzanas, C. Kittas, A. Sapounas, and C. Nikita-Martzopoulou, "Analysis of airflow through experimental rural buildings: Sensitivity to turbulence models," *Biosystems Engineering*, vol. 97, no. 2, pp. 229–239, jun 2007. [Online]. Available: <https://linkinghub.elsevier.com/retrieve/pii/S1537511007000499>
- [127] A. T. Nguyen and S. Reiter, "The effect of ceiling configurations on indoor air motion and ventilation flow rates," *Building and Environment*, vol. 46, no. 5, pp. 1211–1222, may 2011. [Online]. Available: <https://linkinghub.elsevier.com/retrieve/pii/S0360132310003689>
- [128] X. Zhao and Q. Chen, "Inverse design of indoor environment using an adjoint RNG $k-\epsilon$ turbulence model," *Indoor Air*, vol. 29, no. 2, pp. 320–330, mar 2019. [Online]. Available: <https://onlinelibrary.wiley.com/doi/10.1111/ina.12530>
- [129] P. I. Energy And Environment, W. Y. Tey, Y. Asako, N. A. Che Sidik, and G. Rui-Zher, "Governing Equations in Computational Fluid Dynamics: Derivations and A Recent Review," *Progress in Energy and Envirnoment*, vol. 1, p. 19, 2017. [Online]. Available: https://www.researchgate.net/publication/322032449_Governing_Equations_in_Computational_Fluid_Dynamics_Derivations_and_A_Recent_Review

- [130] F. P. Incropera, T. L. Bergman, D. P. DeWitt, and A. S. Lavine, *Fundamentals of Heat and Mass Transfer*, 7th ed., T. L. Bergman, F. P. Incropera, D. P. DeWitt, and A. S. Lavine, Eds. John Wiley & Sons, 2011.
- [131] F. M. White, *Fluid Mechanics*, 4th ed., J. Loyd and J. P. Holdman, Eds. Boston: McGraw-Hill Series in Mechanical Engineering, 1999.
- [132] Y. A. Çengel and J. M. Cimbala, *Fluid Mechanics: Fundamentals and Applications*, 1st ed. McGraw-Hill, 2004.
- [133] B. Končar and L. Klobučar, *Use of CFD Codes for Calculation of Radiation Heat Transfer: From Validation to Application*. BoD – Books on Demand, 2018, 2018, ch. 2, pp. 23–41.
- [134] C. Greenshields, “Energy Equation in OpenFOAM | CFD Direct,” 2016. [Online]. Available: <https://cfd.direct/openfoam/energy-equation/#x1-70004>
- [135] D. B. Spalding, “A Single Formula for the “Law of the Wall,”” *Journal of Applied Mechanics*, vol. 28, no. 3, pp. 455–458, sep 1961. [Online]. Available: <https://asmedigitalcollection.asme.org/appliedmechanics/article/28/3/455/386110/A-Single-Formula-for-the-Law-of-the-Wall>
- [136] H. Li, D. Wang, and H. Xu, “Improved Law-of-the-Wall Model for Turbulent Boundary Layer in Engineering,” *AIAA Journal*, pp. 1–12, jun 2020. [Online]. Available: <https://arc.aiaa.org/doi/10.2514/1.J058464>
- [137] B. Mandal and H. Mazumdar, “The Importance Of The Law Of The Wall,” *International Journal of Applied Mechanics and Engineering*, vol. 20, no. 4, pp. 857–869, dec 2015. [Online]. Available: <http://content.sciendo.com/view/journals/ijame/20/4/article-p857.xml>
- [138] H. M. Nagib and K. A. Chauhan, “Variations of von Kármán coefficient in canonical flows,” in *Physics of Fluids*, vol. 20, no. 10. American Institute of Physics Inc., oct 2008, p. 11. [Online]. Available: <http://aip.scitation.org/doi/10.1063/1.3006423>
- [139] P. Bradshaw and G. P. Huang, “The law of the wall in turbulent flow,” *Proceedings of the Royal Society of London. Series A: Mathematical and Physical Sciences*, vol. 451, no. 1941, pp. 165–188, oct 1995. [Online]. Available: <https://royalsocietypublishing.org/doi/10.1098/rspa.1995.0122>
- [140] A. Schalin and P. V. Nielsen, “Impact of turbulence anisotropy near walls in room airflow,” *Indoor Air*, vol. 14, no. 3, pp. 159–168, jun 2004. [Online]. Available: <https://vbn.aau.dk/en/publications/impact-of-turbulence-anisotropy-near-walls-in-room-airflowhttps://onlinelibrary.wiley.com/doi/10.1111/j.1600-0668.2004.00201e.x>
- [141] A. J. Smits, “Viscous Flows and Turbulence,” Princeton University, Princeton, Tech. Rep., 2009.

- [142] S. H. El Tahry, “k-epsilon equation for compressible reciprocating engine flows,” *Journal of Energy*, vol. 7, no. 4, pp. 345–353, 1983.
- [143] J. C. R. Hunt and D. J. Carruthers, “Rapid distortion theory and the ‘problems’ of turbulence,” *Journal of Fluid Mechanics*, vol. 212, no. 2, pp. 497–532, 1990. [Online]. Available: <https://www.cambridge.org/core/journals/journal-of-fluid-mechanics/article/abs/rapid-distortion-theory-and-the-problems-of-turbulence/366D92CEB8403E4479589E51246B63B2>
- [144] V. Yakhot and L. M. Smith, “The renormalization group, the ϵ -expansion and derivation of turbulence models,” *Journal of Scientific Computing*, vol. 7, no. 1, pp. 35–61, 1992.
- [145] W. C. Reynolds, “Fundamentals of Turbulence for Turbulence Modeling and Simulation.” Stanford University, Tech. Rep., 1987. [Online]. Available: <https://apps.dtic.mil/sti/citations/ADP005793>
- [146] T.-H. Shih, J. Zhu, and J. L. Lumley, “A new Reynolds stress algebraic equation model,” *Computer Methods in Applied Mechanics and Engineering*, vol. 125, no. 1-4, pp. 287–302, sep 1995. [Online]. Available: <https://linkinghub.elsevier.com/retrieve/pii/0045782595007964>
- [147] P. A. Durbin, “Separated flow computations with the k- ϵ -v2 model,” *AIAA Journal*, vol. 33, no. 4, pp. 659–664, apr 1995. [Online]. Available: <https://arc.aiaa.org/doi/10.2514/3.12628>
- [148] F. S. Lien and G. Kalitzin, “Computations of transonic flow with the ν^2 -f turbulence model,” *International Journal of Heat and Fluid Flow*, vol. 22, no. 1, pp. 53–61, 2001.
- [149] L. Davidson, P. V. Nielsen, and A. Sveningsson, “Modifications of the V2 Model for Computing the Flow in a 3D Wall Jet,” *Turbulence, Heat and Mass Transfer*, vol. 4, pp. 577–584, 2003.
- [150] D. C. Wilcox, “A half century historical review of the k-omega model,” in *29th Aerospace Sciences Meeting*. Reston, Virginia: American Institute of Aeronautics and Astronautics, jan 1991. [Online]. Available: <https://arc.aiaa.org/doi/10.2514/6.1991-615>
- [151] D. B. Spalding, “Kolmogorov’s two-equation model of turbulence,” *Proceedings of the Royal Society of London. Series A: Mathematical and Physical Sciences*, vol. 434, no. 1890, pp. 211–216, jul 1991. [Online]. Available: <https://royalsocietypublishing.org/doi/10.1098/rspa.1991.0089>
- [152] NASA, “Wilcox k-omega Model,” 2021. [Online]. Available: <https://turbmodels.larc.nasa.gov/wilcox.html>

- [153] F. R. Menter, "Two-equation eddy-viscosity turbulence models for engineering applications," *AIAA Journal*, vol. 32, no. 8, pp. 1598–1605, aug 1994. [Online]. Available: <https://arc.aiaa.org/doi/10.2514/3.12149>
- [154] F. Menter and T. Esch, "Elements of Industrial Heat Transfer Predictions," in *16th Brazilian Congress of Mechanical Engineering (COBEM)*, Uberlandia, Brazil, 2001, pp. 117–127.
- [155] T. O. Foundation, "OpenFOAM v7 User Guide." [Online]. Available: <https://cfd.direct/openfoam/user-guide-v7>
- [156] H. Jasak, "Error Analysis and Estimation for the Finite Volume Method with Applications to Fluid Flows," Ph.D, Imperial College of Science, Technology and Medicine, 1996.
- [157] A. Wimshurst, "The PISO Algorithm," 2019. [Online]. Available: <https://www.fluidmechanics101.com/pages/lectures.html>
- [158] L. S. Caretto, A. D. Gosman, S. V. Patankar, and D. B. Spalding, "Two calculation procedures for steady, three-dimensional flows with recirculation," in *Proceedings of the Third International Conference on Numerical Methods in Fluid Mechanics. Lecture Notes in Physics*, vol 19 ed., H. Cabannes and R. Temam, Eds. Berlin, Heidelberg: Springer, 1973, ch. Proceeding, pp. 60–68.
- [159] R. I. Issa, "Solution of the Implicitly Discretised Fluid Flow Equations by Operator-Splitting," *Journal of Computational Physics*, vol. 62, no. 1, pp. 40–65, 1986.
- [160] D. S. Jang, R. Jetli, and S. Acharya, "COMPARISON OF THE PISO, SIMPLER, AND SIMPLEC ALGORITHMS FOR THE TREATMENT OF THE PRESSURE-VELOCITY COUPLING IN STEADY FLOW PROBLEMS," *Numerical Heat Transfer*, vol. 10, no. 3, pp. 209–228, sep 1986. [Online]. Available: <http://www.tandfonline.com/doi/abs/10.1080/10407788608913517>
- [161] A. Bayón, "Numerical analysis of air-water flows in hydraulic structures using computational fluid dynamics (CFD)," PhD Thesis, Universitat Politècnica de València, 2017. [Online]. Available: <https://dialnet.unirioja.es/servlet/tesis?codigo=250873>
- [162] F. Aristides Castro, "Mecânica dos Fluidos Computacional," p. 92, 2014.
- [163] J. F. Thompson, *Handbook of Grid Generation*, J. F. Thompson, B. K. Soni, and N. P. Weatherill, Eds. CRC Press LLC, 1999.
- [164] V. D. Liseikin, *Grid Generation Methods*, 3rd ed., ser. Scientific Computation. Cham, Switzerland: Springer International Publishing, 2017. [Online]. Available: <http://link.springer.com/10.1007/978-3-319-57846-0>

-
- [165] M. Ishigaki, S. Abe, Y. Sibamoto, and T. Yonomoto, "Influence of mesh non-orthogonality on numerical simulation of buoyant jet flows," *Nuclear Engineering and Design*, vol. 314, pp. 326–337, apr 2017. [Online]. Available: <https://linkinghub.elsevier.com/retrieve/pii/S0029549317300596>
- [166] L. Fangqing, "CFD with OpenSource software A Thorough Description Of How Wall Functions Are Implemented In OpenFOAM," in *In Proceedings of CFD with OpenSource Software, 2016*, H. Nilsson and I. Mohsen, Eds., 2017. [Online]. Available: http://www.tfd.chalmers.se/~hahani/kurser/OS_CFD_2016/FangqingLiu/openfoamFinal.pdf
- [167] P. V. Nielsen, A. Restivo, and J. H. Whitelaw, "BUOYANCY-AFFECTED FLOWS IN VENTILATED ROOMS," *Numerical Heat Transfer*, vol. 2, no. 1, pp. 115–127, jan 1979. [Online]. Available: <http://www.tandfonline.com/doi/abs/10.1080/10407787908913402>
- [168] W. M. Kays, "Turbulent Prandtl number. Where are we?" *ASME Transactions Journal of Heat Transfer*, vol. 116, no. 2, pp. 284—295, 1994.
- [169] S. W. Churchill, "A Reinterpretation of the Turbulent Prandtl Number," *Industrial & Engineering Chemistry Research*, vol. 41, no. 25, pp. 6393–6401, dec 2002. [Online]. Available: <https://pubs.acs.org/doi/10.1021/ie011021k>
- [170] NASA, "Similarity Parameters," 2018. [Online]. Available: <https://www.grc.nasa.gov/www/k-12/airplane/airsim.html>

ANNEXES

- 7.1 ANNEX 1 - T EQUATION IN OPENFOAM
- 7.2 ANNEX 2 -PRESSURE AND VELOCITY CORRECTIONS
[8]
- 7.3 ANNEX 3 - DIMENSIONLESS NUMBERS
- 7.4 ANNEX 4 - 2D CHANNEL FLOW
- 7.5 ANNEX 5 - 2D ISOTHERMAL TEST CASE
- 7.6 ANNEX 6 - 2D NON-ISOTHERMAL TEST CASE
- 7.7 ANNEX 7 - 3D ISOTHERMAL TEST CASE

7 ANNEXES

7.1 Annex 1 - T equation in OpenFOAM

```

{
  alphas = turbulence->nut()/Prt;
  alphas.correctBoundaryConditions();

  volScalarField alphaEff("alphaEff", turbulence->nu()/Pr + alphas);

  fvScalarMatrix TEqn
  (
    fvm::div(phi, T)
    - fvm::laplacian(alphaEff, T)
    ==
    radiation->ST(rhoCpRef, T)
    + fvOptions(T)
  );

  TEqn.relax();

  fvOptions.constrain(TEqn);

  TEqn.solve();

  radiation->correct();

  fvOptions.correct(T);

  rhoK = 1.0 - beta*(T - TRef);
}

```

Figure 7.1 – Equation for temperature in a steady-state solver.

```

{
  alphas = turbulence->nut()/Prt;
  alphas.correctBoundaryConditions();

  volScalarField alphaEff("alphaEff", turbulence->nu()/Pr + alphas);

  fvScalarMatrix TEqn
  (
    fvm::ddt(T)
    + fvm::div(phi, T)
    - fvm::laplacian(alphaEff, T)
    ==
    radiation->ST(rhoCpRef, T)
    + fvOptions(T)
  );

  TEqn.relax();

  fvOptions.constrain(TEqn);

  TEqn.solve();

  radiation->correct();

  fvOptions.correct(T);

  rhoK = 1.0 - beta*(T - TRef);
}

```

Figure 7.2 – Equation for temperature in a transient solver.

7.2 Annex 2 -Pressure and Velocity Corrections [8]

The goal is to find a way of improving the guessed pressure p^* such that the resulting starred velocity field will progressively get closer to satisfying the continuity equation. Consider that the correct pressure p is obtained from

$$p = p^* + p', \quad (7.1)$$

where p' is the *pressure correction*. Next, it is necessary to know how the velocity components respond to this change in pressure. The corresponding velocity corrections u' , v' , w' can be introduced in a similar manner:

$$u = u^* + u' \quad v = v^* + v' \quad w = w^* + w'. \quad (7.2)$$

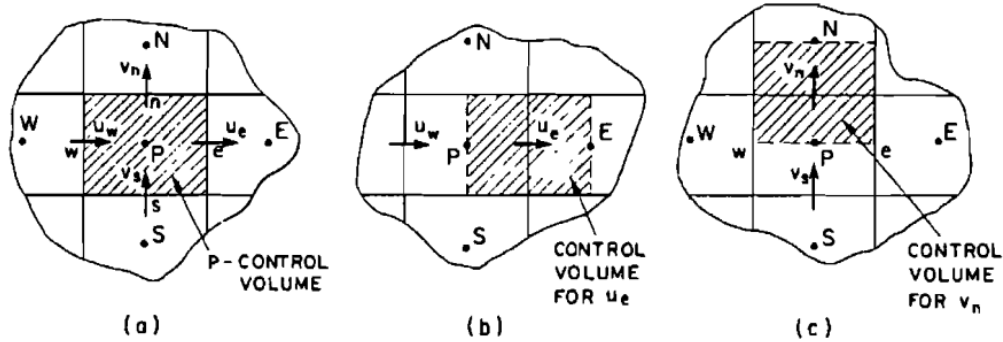


Figure 7.3 – Representation of a 2D control volume [8].

Consider the control volume for the x –direction in Figure 7.3 (b) the discretization equation can be written as

$$a_e u_e = \sum a_{nb} u_{nb} + b_e + (p_P - p_E) A_e \quad (7.3)$$

and, the corresponding velocity component based on a guessed pressure field p^*

$$a_e u_e^* = \sum a_{nb} u_{nb}^* + b_e + (p_P^* - p_E^*) A_e, \quad (7.4)$$

if Eq.(7.4) is subtracted from Eq.(7.3), it yields:

$$a_e u'_e = \sum a_{nb} u'_{nb} + (p'_P - p'_E) A_e. \quad (7.5)$$

At this point, the term $\sum a_{nb} u'_{nb}$ will be dropped from the equation (computational convenience). The result is:

$$a_e u'_e = (p'_P - p'_E) A_e \quad (7.6)$$

or

$$u'_e = \frac{A_e}{a_e} (p'_P - p'_E), \quad (7.7)$$

Equation 7.7 is called the velocity-correction formula, which can also be written as

$$u_e = u_e^* + d_e(p'_P - p'_E) \quad \text{where} \quad d_e = \frac{A_e}{a_e} \quad (7.8)$$

This shows how the starred velocity u_e^* is to be corrected in response to the pressure corrections to produce u_e .

The correction formulas for the velocity components in other directions can be written similarly:

$$v_n = v_n^* + d_n(p'_P - p'_N), \quad (7.9)$$

$$w_t = w_t^* + d_t(p'_P - p'_T). \quad (7.10)$$

Thus, now it is possible to obtain a discretization equation for p' .

7.3 Annex 3 - Dimensionless Numbers

Forces are generated between a fluid and an object, their magnitude depends on the shape of the object and the speed, mass, viscosity and compressibility of the fluid. To properly model these effects, similarity parameters [170] are often used. If two experiments have the same values for the similarity parameters, then the relative importance of the forces are being correctly modelled. Some important relations are the following:

Table 7.1 – Some dimensionless numbers

Dimensionless Number	Formula	Expresses the:
Mach	$M = \frac{u}{a} \quad (7.11)$	Ratio of object speed to speed of sound .
Reynolds	$Re = \frac{uL}{\nu} \quad (7.12)$	Ratio of inertial forces to viscous forces.
Archimedes	$Ar = \frac{\beta g L \Delta T}{u^2} \quad (7.13)$	Ratio of gravitational forces to viscous forces. It is used to determine the motion of fluids due to density differences.
Prandtl	$Pr = \frac{c_p \mu}{k} \quad (7.14)$	Ratio of momentum diffusivity (kinematic viscosity) to thermal diffusivity .

7.4 Annex 4 - 2D Channel Flow

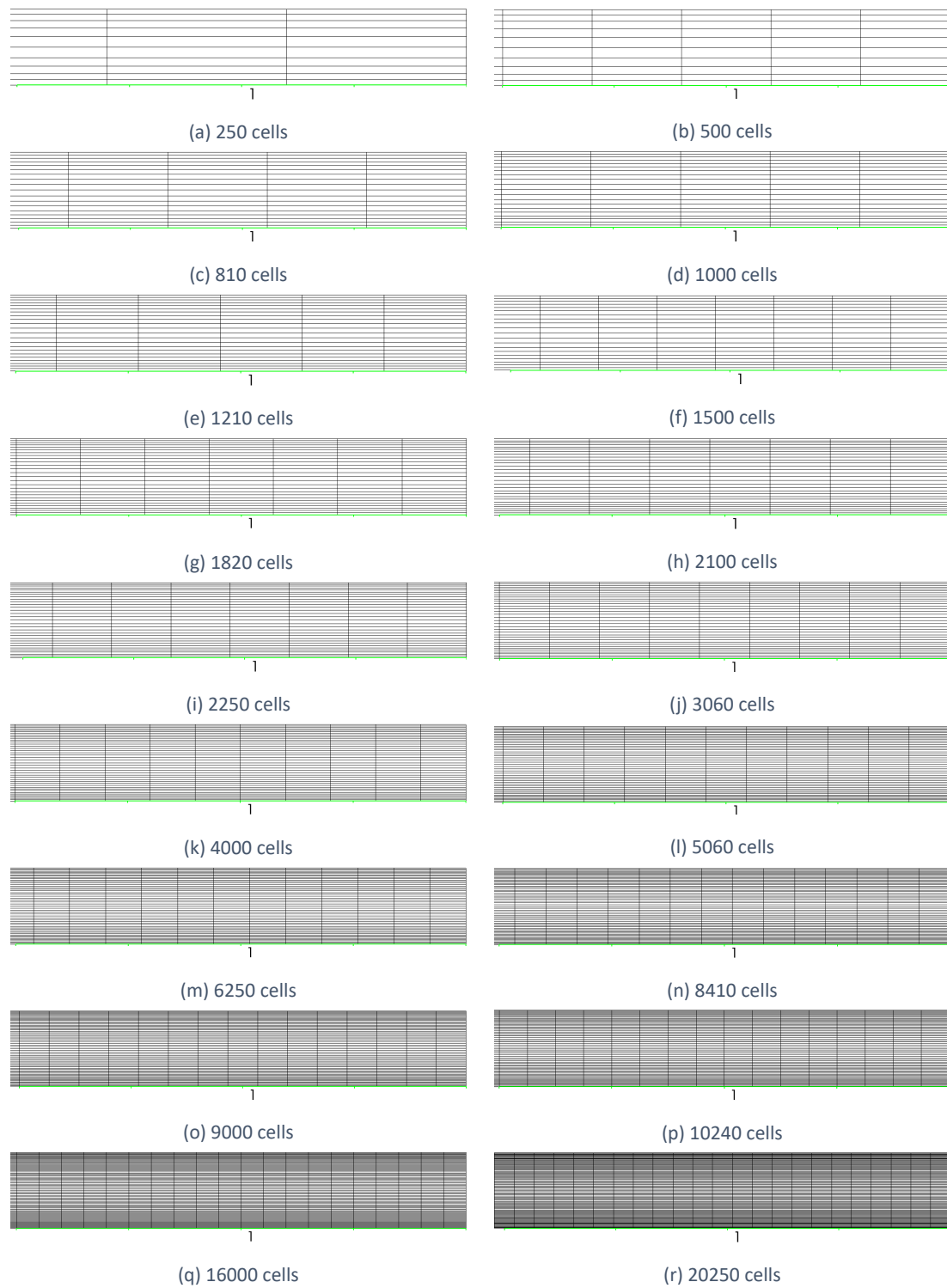


Figure 7.4 – Channel meshes studied (1m).

7.5 Annex 5 - 2D Isothermal Test Case

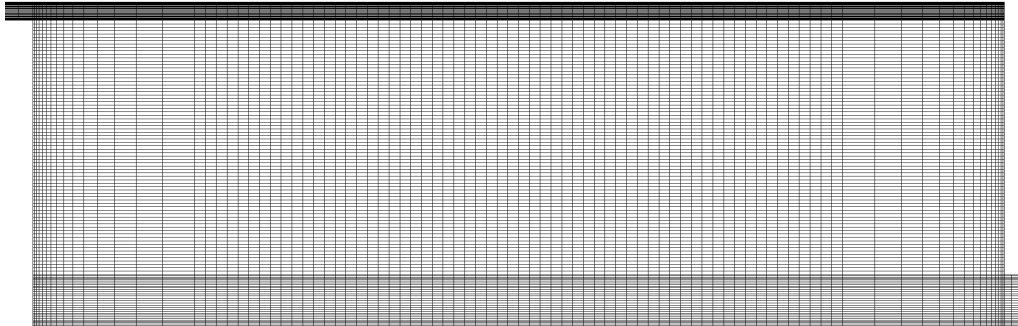


Figure 7.5 – 2D Annex 20 room *coarse* mesh (16650 cells).

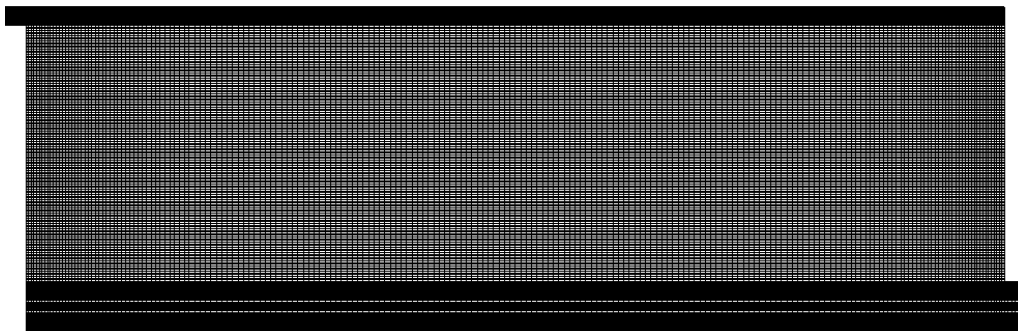


Figure 7.6 – 2D Annex 20 room *medium* mesh (76200 cells).

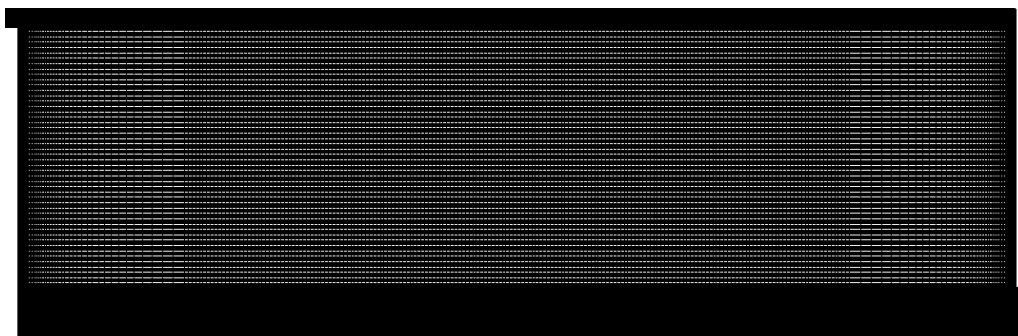


Figure 7.7 – 2D Annex 20 room *fine* mesh (159750 cells).

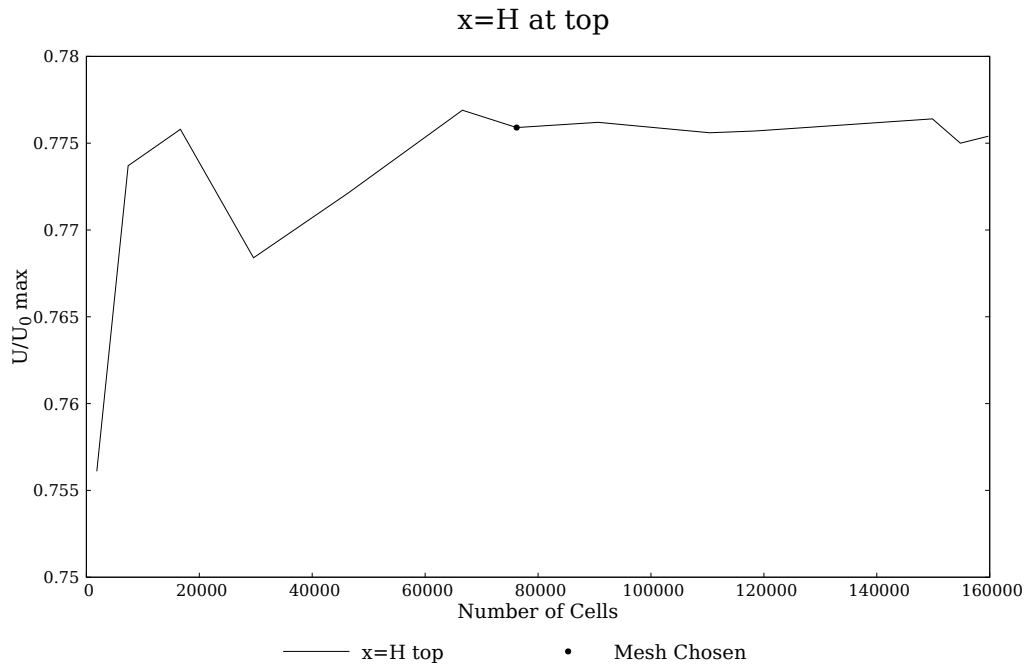


Figure 7.8 – Evolution of U/U_0 maximum near the ceiling for $x = H$.

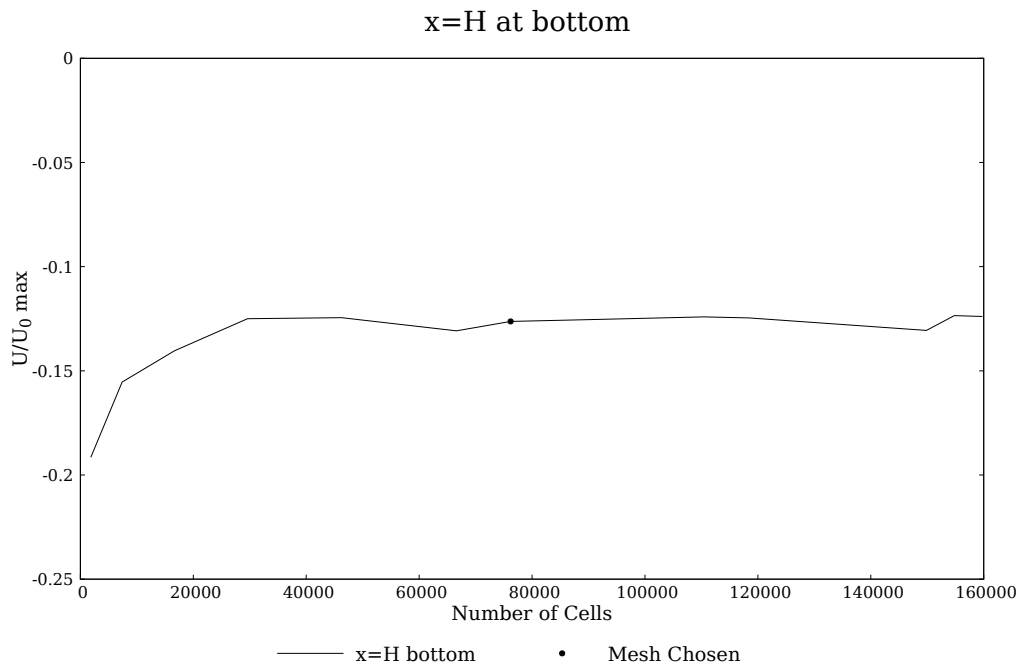


Figure 7.9 – Evolution of U/U_0 maximum near the floor for $x = H$.

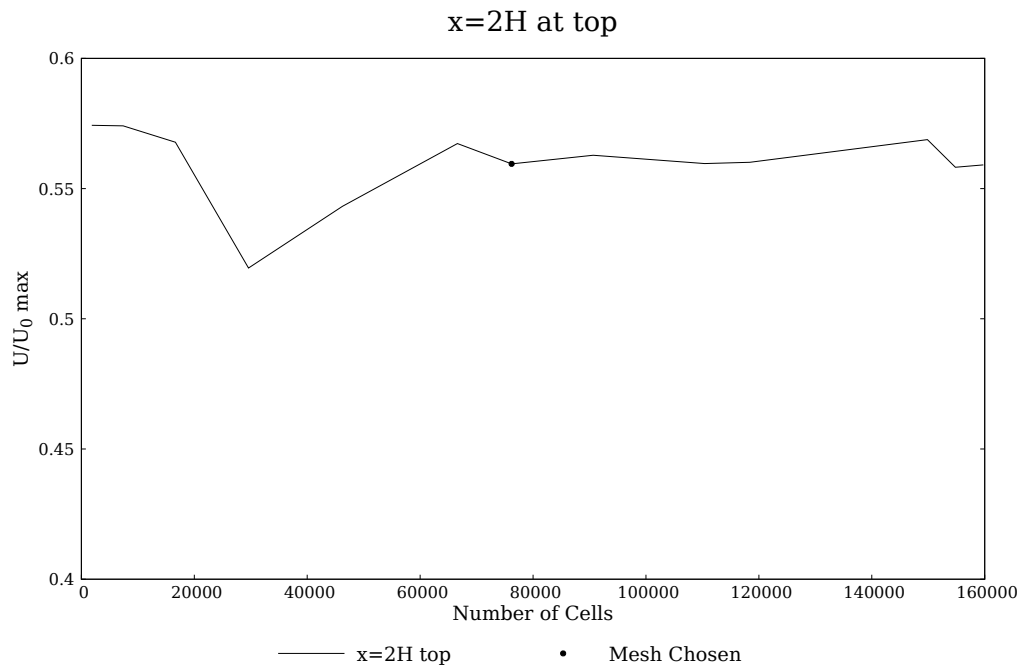


Figure 7.10 – Evolution of U/U_0 maximum near the ceiling for $x = 2H$.

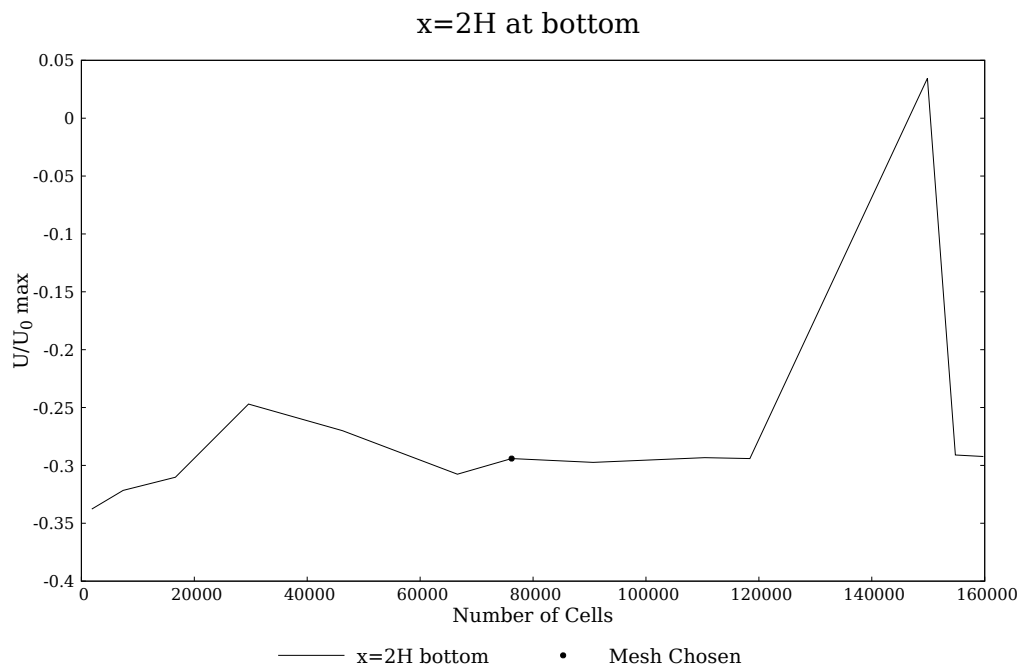


Figure 7.11 – Evolution of U/U_0 maximum near the floor for $x = 2H$.

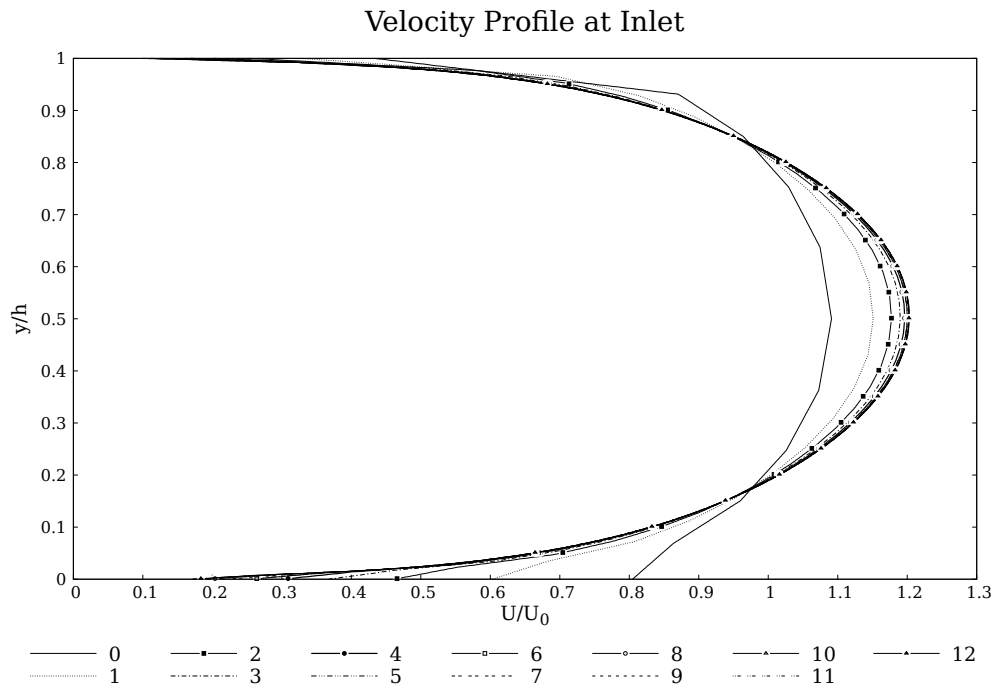


Figure 7.12 – Velocity profile (U/U_0) at the room inlet for all meshes.

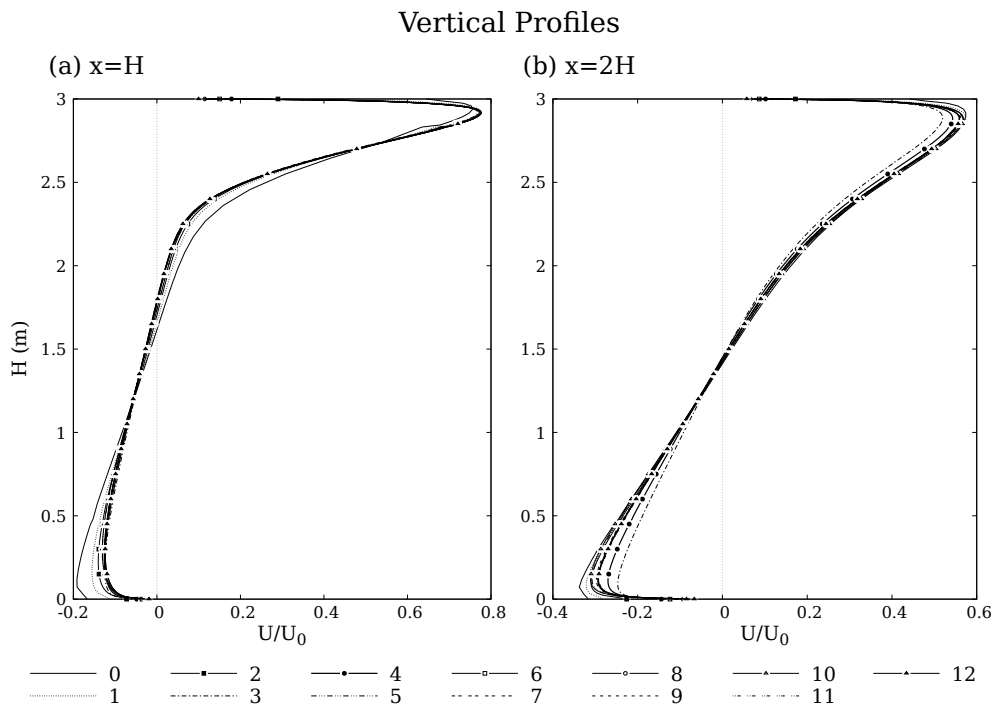
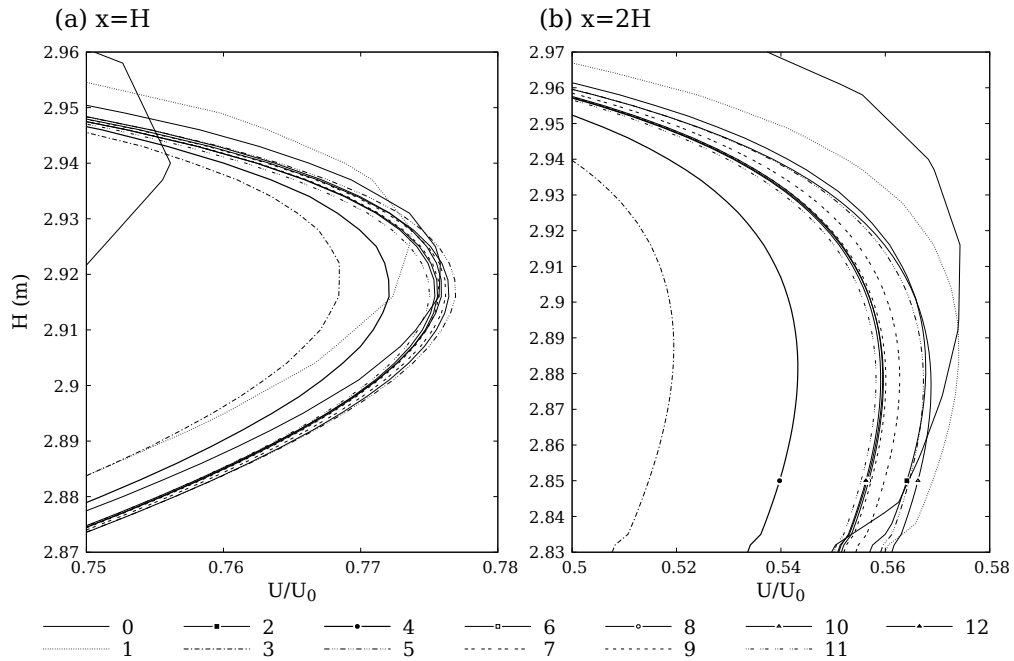
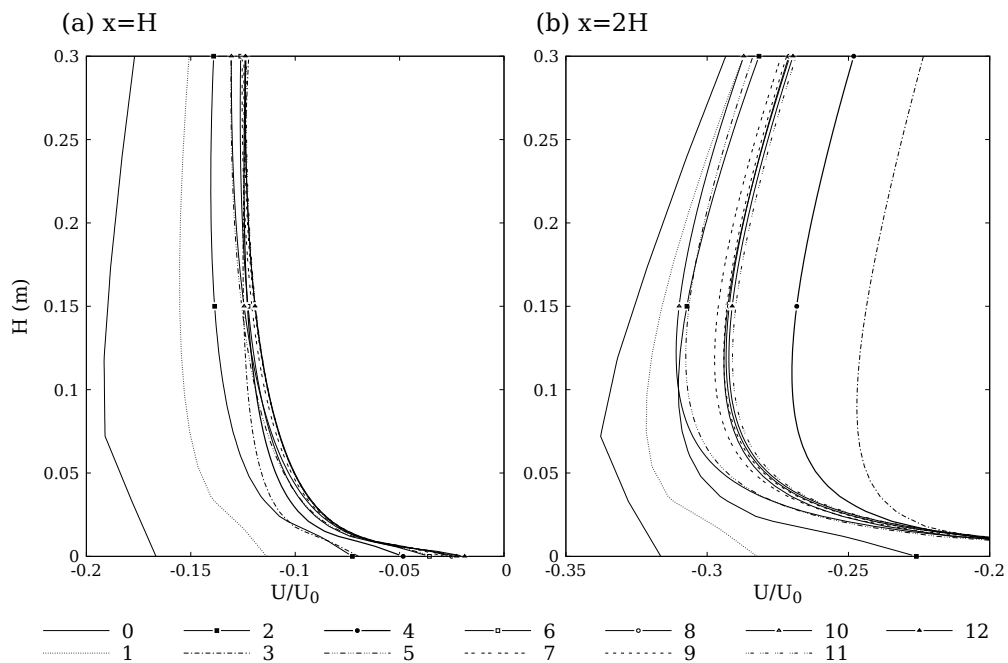


Figure 7.13 – Velocity profile (U/U_0) at $x = H$ and $x = 2H$ for all meshes.

Velocity Profile Detail near the Ceiling

Figure 7.14 – Velocity profile (U/U_0) at $x=H$ and $x=2H$, near the room ceiling for all meshes.

Velocity Profile Detail near the Floor

Figure 7.15 – Velocity profile (U/U_0) at $x=H$ and $x=2H$, near the room floor for all meshes.

7.6 Annex 6 - 2D non-Isothermal Test Case

$Re = 5000$

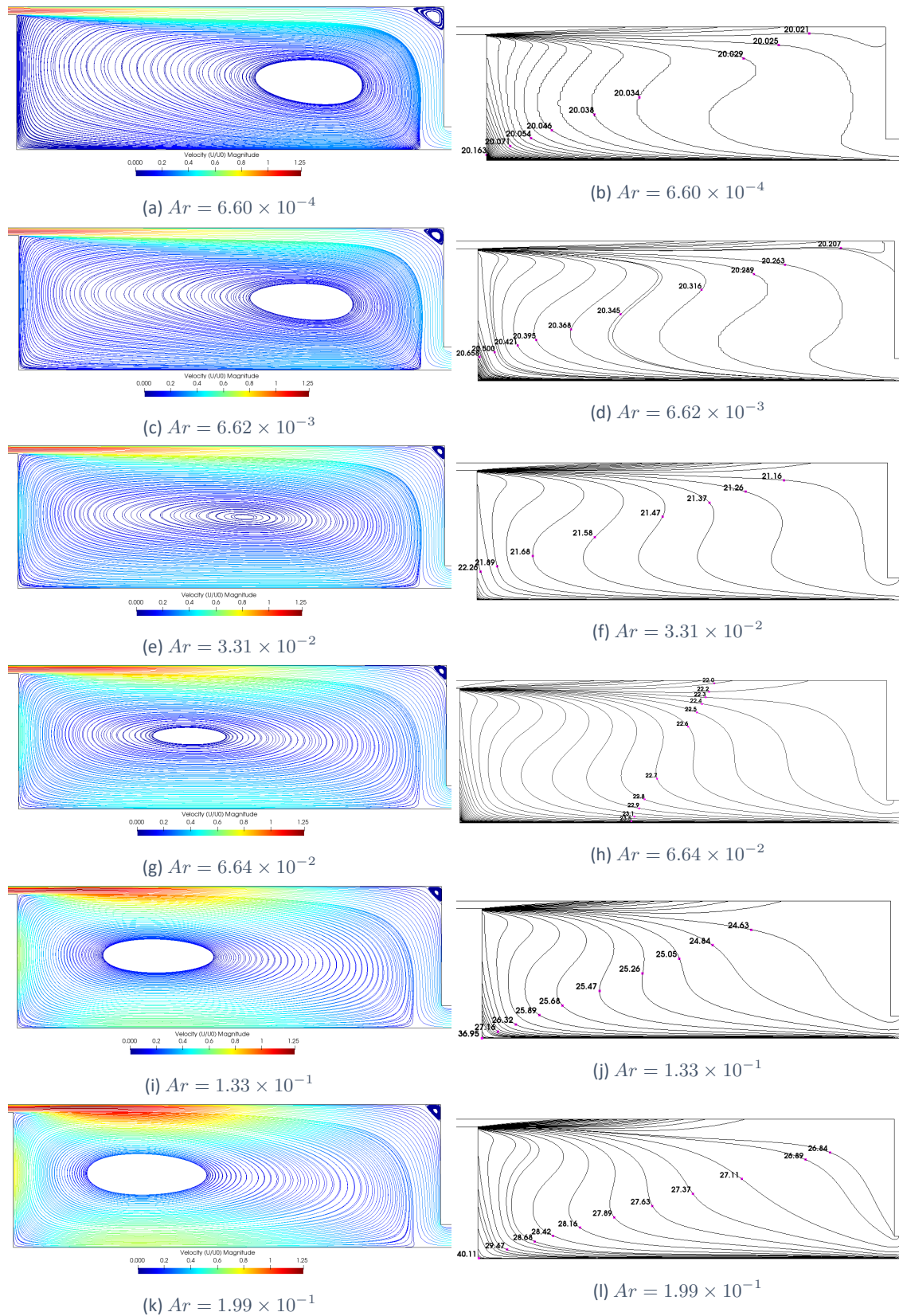


Figure 7.16 – Velocity (U/U_0) streamlines and Temperature isotherms (T in $^{\circ}C$) for $Re = 5000$.

$Re = 7100$

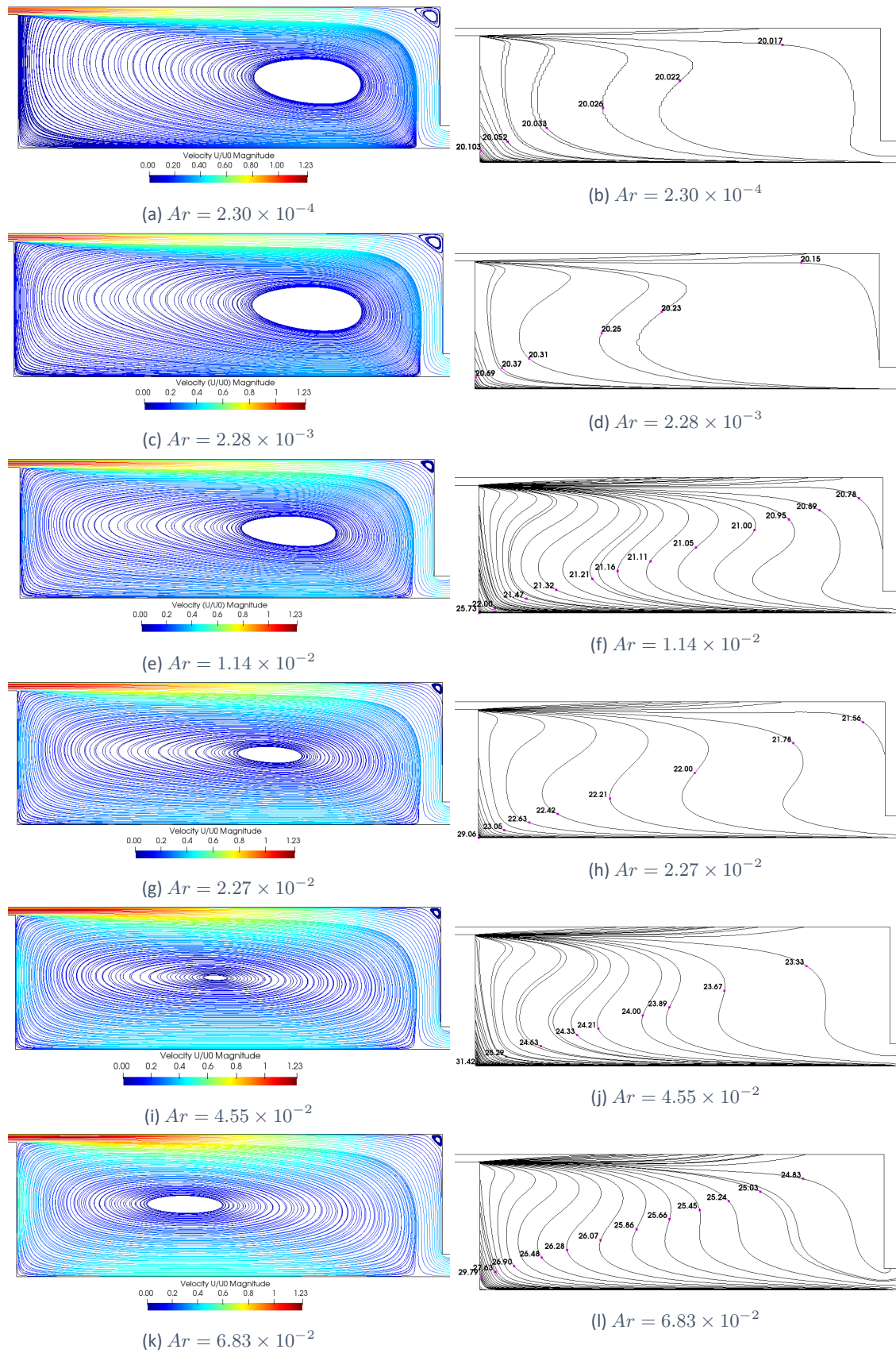


Figure 7.17 – Velocity (U/U_0) streamlines and Temperature isotherms (T in $^{\circ}C$) for $Re = 7100$.

7.7 Annex 7 - 3D Isothermal Test Case

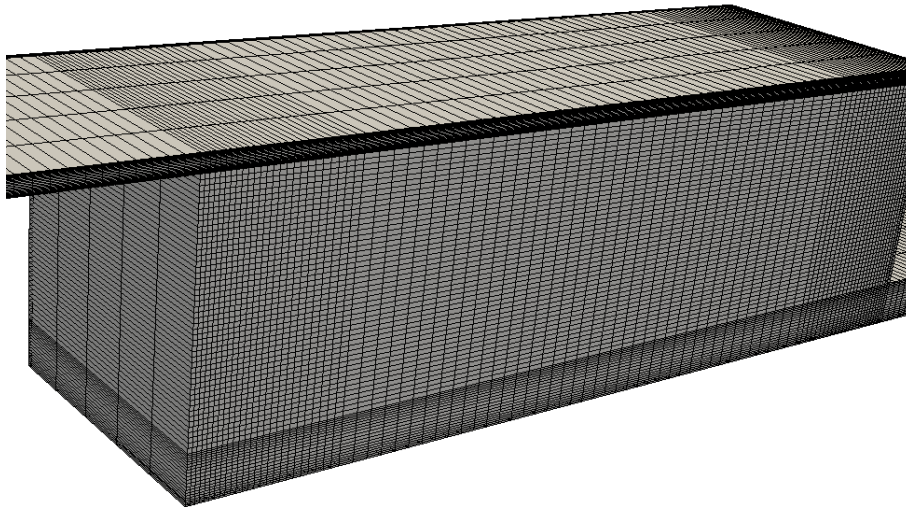


Figure 7.18 – 3D Annex 20 room *coarse* mesh (53000 cells).

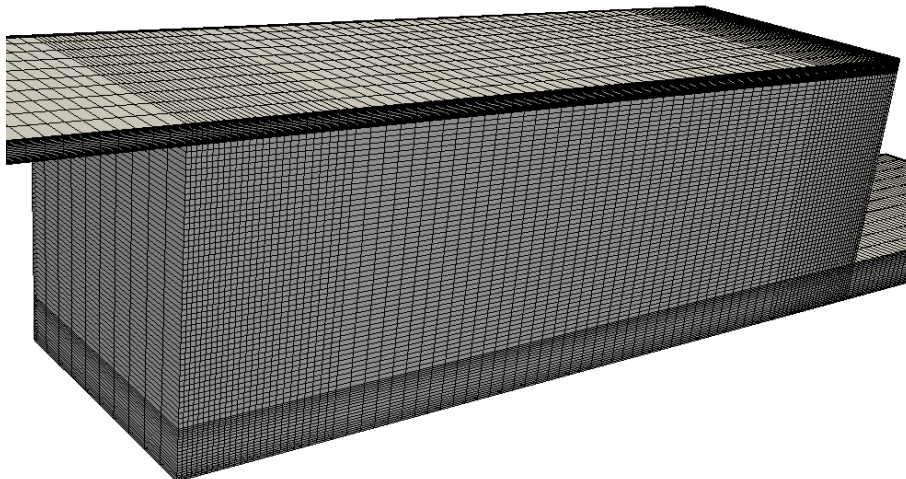


Figure 7.19 – 3D Annex 20 room *medium* mesh (106000 cells).

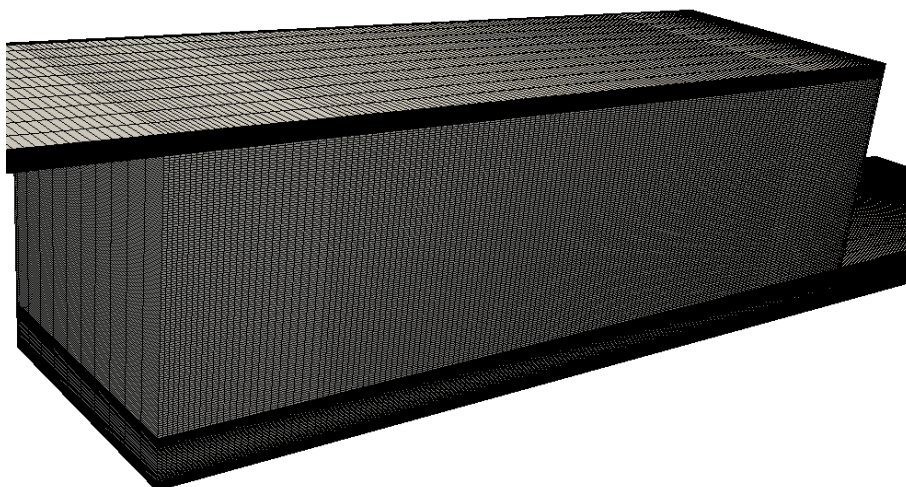


Figure 7.20 – 3D Annex 20 room *fine* mesh (462500 cells).

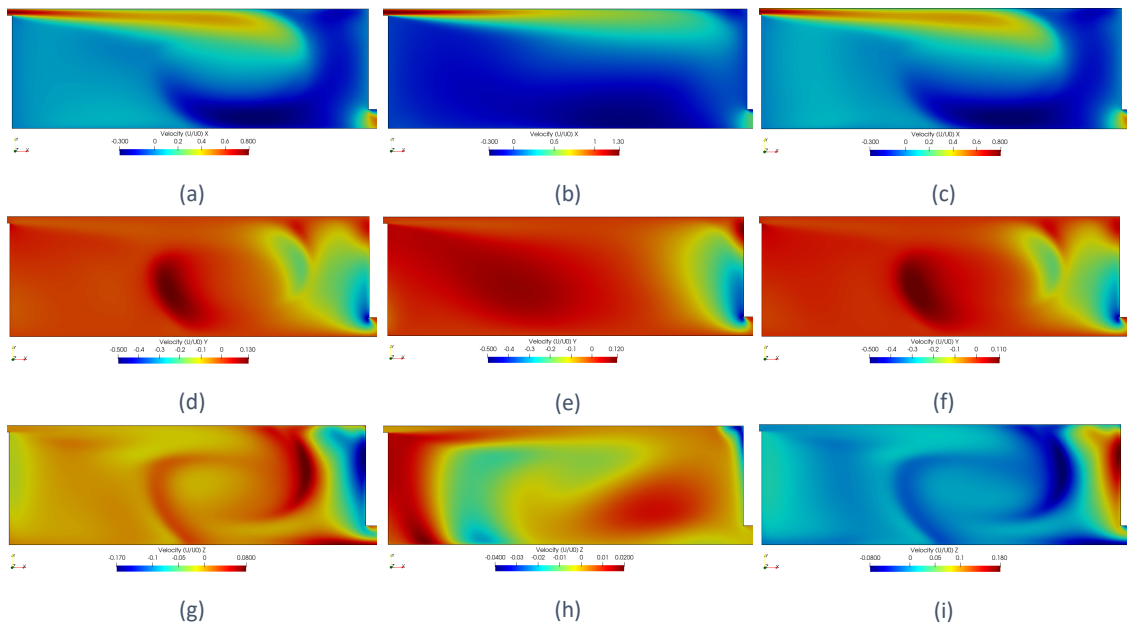


Figure 7.21 – Velocity distribution at the near wall regions and at the symmetry plane for the x -component (a,d,g), y -component (b,e,h) and z -component (c,f,i).

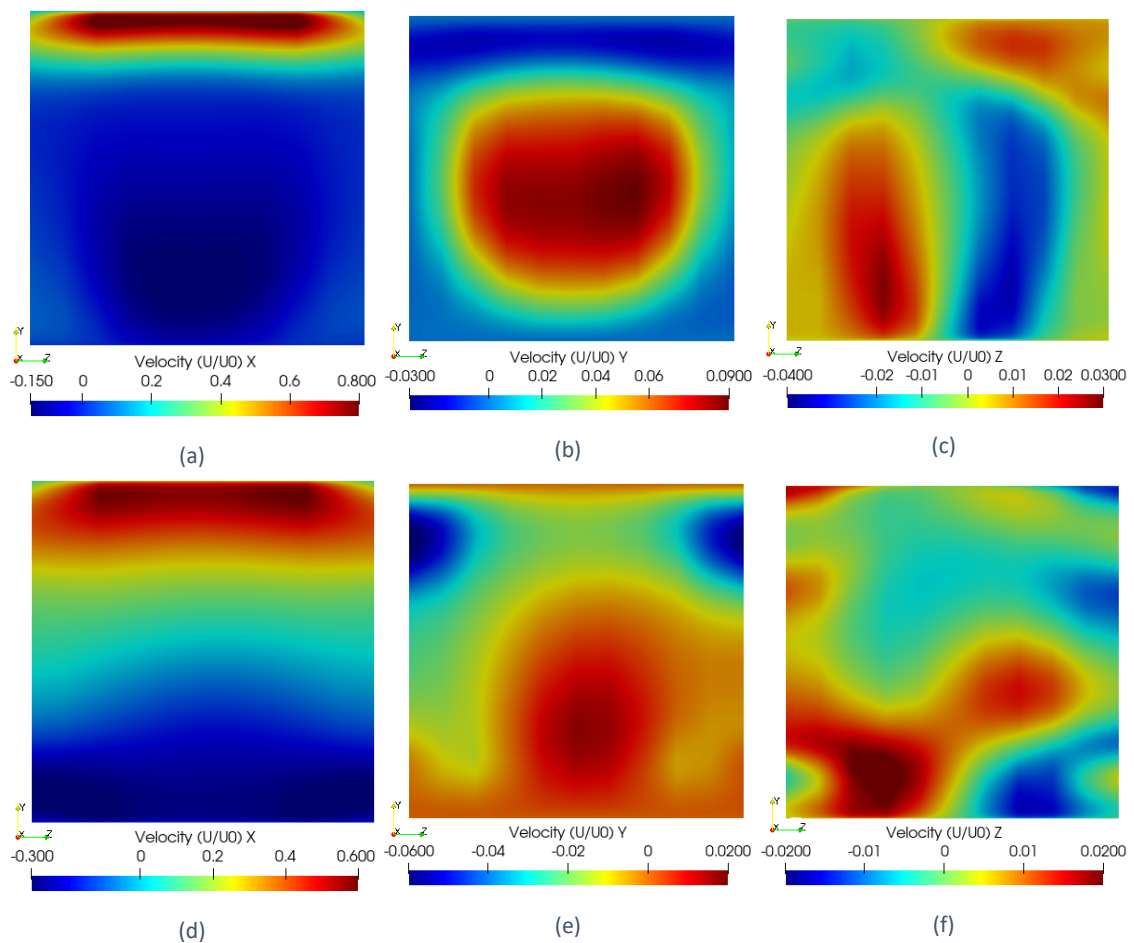


Figure 7.22 – Velocity distribution at the $x = H$ (a,b,c) and $x = 2H$, for the x -component, y -component and z -component, respectively.

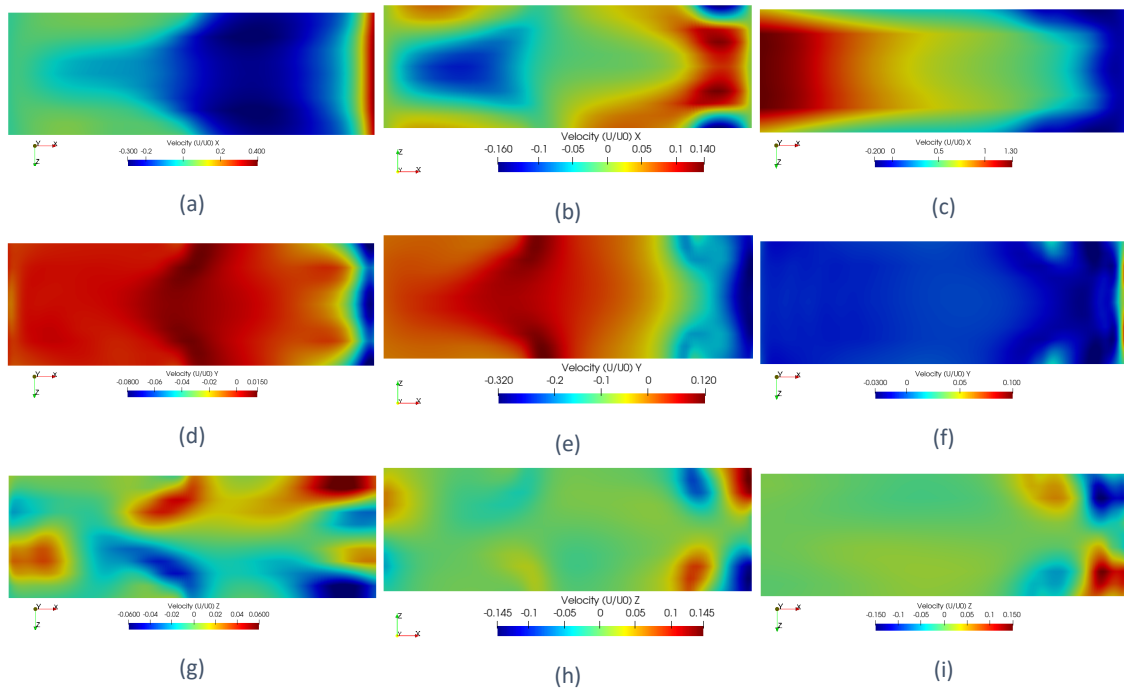


Figure 7.23 – Velocity distribution at the $y = h/2$ (a,d,g), $y = 0.5H$ (b,e,h), and $y = H - h/2$ (c,f,i), for the x -component, y -component and z -component.

